Article

Microbiota-driven antitumour immunity mediated by dendritic cell migration

https://doi.org/10.1038/s41586-025-09249-8

Received: 16 January 2023

Accepted: 5 June 2025

Published online: 14 July 2025

Open access

Check for updates

Nina Yi-Tzu Lin[1,2,19], Shota Fukuoka[1,19], Shohei Koyama[1,3,19], Daisuke Motooka[4], Dieter M. Tourlousse[5], Yuko Shigeno[6], Yuki Matsumoto[4], Hiroyuki Yamano[4], Kazutoshi Murotomi[5], Hideyuki Tamaki[7], Takuma Irie[1], Eri Sugiyama[1,8], Shogo Kumagai[1,9], Kota Itahashi[1], Tokiyoshi Tanegashima[1], Kaori Fujimaki[2], Sachiko Ito[2], Mariko Shindo[10], Takahiro Tsuji[10], Hiroaki Wake[10], Keisuke Watanabe[1], Yuka Maeda[1], Tomohiro Enokida[11], Makoto Tahara[11], Riu Yamashita[12], Takao Fujisawa[11,13], Motoo Nomura[14], Akihito Kawazoe[15], Koichi Goto[8], Toshihiko Doi[15], Kohei Shitara[15], Hiroyuki Mano[9], Yuji Sekiguchi[5], Shota Nakamura[4], Yoshimi Benno[6,16] ✉ & Hiroyoshi Nishikawa[1,2,17,18] ✉

Gut microbiota influence the antitumour efficacy of immune checkpoint blockade[1–6], but the mechanisms of action have not been fully elucidated. Here, we show that a new strain of the bacterial genus *Hominenteromicrobium* (designated YB328) isolated from the faeces of patients who responded to programmed cell death 1 (PD-1) blockade augmented antitumour responses in mice. YB328 activated tumour-specific $CD8^+$ T cells through the stimulation of $CD103^+CD11b^-$ conventional dendritic cells (cDCs), which, following exposure in the gut, migrated to the tumour microenvironment. Mice showed improved antitumour efficacy of PD-1 blockade when treated with faecal transplants from non-responder patients supplemented with YB238. This result suggests that YB328 could function in a dominant manner. YB328-activated $CD103^+CD11b^-$ cDCs showed prolonged engagement with tumour-specific $CD8^+$ T cells and promoted PD-1 expression in these cells. Moreover, YB238-augmented antitumour efficacy of PD-1 blockade treatment was observed in multiple mouse models of cancer. Patients with elevated YB328 abundance had increased infiltration of $CD103^+CD11b^-$ cDCs in tumours and had a favourable response to PD-1 blockade therapy in various cancer types. We propose that gut microbiota enhance antitumour immunity by accelerating the maturation and migration of $CD103^+CD11b^-$ cDCs to increase the number of $CD8^+$ T cells that respond to diverse tumour antigens.

Immune checkpoint blockade (ICB) therapies, including monoclonal antibodies against PD-1 and PD-1 ligand (PD-L1), are used in many cancer types[7]. PD-1 blockade therapies have led to significant improvements in progression-free survival (PFS) and overall survival. However, the complete response rate remains low[8–11]. Therefore, predictive biomarkers for clinical efficacy and new approaches to overcome resistance mechanisms are needed. Notably, high ratios of $PD\text{-}1^+CD8^+$ T cells to $PD\text{-}1^+$ regulatory T (T_{reg}) cells in the tumour microenvironment (TME) correspond to the responsiveness to PD-1 and PD-L1 inhibitors[12]. Moreover, PD-1 expression by $CD8^+$ T cells is induced by T cell activation signalling, especiallyNFATC1, through the stimulation of fully matured dendritic cells (DCs)[13,14].

In gut microbiota, the abundance of certain bacteria (for example, *Ruminococcus* spp. and *Prevotellaceae* spp.) is associated with the clinical efficacy of ICB therapies[1–6]. Several mechanisms of microbiome-mediated antitumour immunity have been proposed, including stimulation of macrophages and monocytes[15], antigenic mimics between microbiota and tumour antigens[16–18] or direct activation of tumour-infiltrating $CD8^+$ T cells by microbiota-derived metabolites[19–22]. Moreover, a consortium of bacteria isolated from healthy individuals reportedly stimulated $CD103^+$ DCs, which led to the activation of effector $CD8^+$ T cells[23]. However, the detailed mechanisms that underlie the connection between DC maturation by gut microbiota

[1]Division of Cancer Immunology, National Cancer Center Research Institute, Tokyo, Japan. [2]Department of Immunology, Nagoya University Graduate School of Medicine, Nagoya, Japan. [3]Department of Respiratory Medicine and Clinical Immunology, Osaka University Graduate School of Medicine, Osaka, Japan. [4]Department of Infection Metagenomics, Genome Information Research Center, Research Institute for Microbial Diseases, Osaka University, Osaka, Japan. [5]Molecular Biosystems Research Institute, National Institute of Advanced Industrial Science and Technology (AIST), Ibaraki, Japan. [6]Benno Laboratory, RIKEN Baton Zone Program, RIKEN Cluster for Science Technology and Innovation Laboratory, Saitama, Japan. [7]Biomanufacturing Process Research Center, National Institute of Advanced Industrial Science and Technology (AIST), Ibaraki, Japan. [8]Department of Thoracic Oncology, National Cancer Center Hospital East, Chiba, Japan. [9]Division of Cellular Signaling, National Cancer Center Research Institute, Tokyo, Japan. [10]Department of Anatomy and Molecular Cell Biology, Nagoya University Graduate School of Medicine, Nagoya, Japan. [11]Department of Head and Neck Medical Oncology, National Cancer Center Hospital East, Chiba, Japan. [12]Division of Translational Informatics, Exploratory Oncology Research and Clinical Trial Center (EPOC), National Cancer Center, Chiba, Japan. [13]Translational Research Support Office, National Cancer Center Hospital East, Chiba, Japan. [14]Department of Head and Neck Oncology and Innovative Treatment, Graduate School of Medicine, Kyoto University, Kyoto, Japan. [15]Department of Gastroenterology and Gastrointestinal Oncology, National Cancer Center Hospital East, Chiba, Japan. [16]Benno Institute for Gut Microflora (BIGM), Saitama Industrial Technology Center, Saitama, Japan. [17]Division of Cancer Immune Multicellular System Regulation, Center for Cancer Immunotherapy and Immunobiology, Kyoto University Graduate School of Medicine, Kyoto, Japan. [18]Kindai University Faculty of Medicine, Osaka, Japan. [19]These authors contributed equally: Nina Yi-Tzu Lin, Shota Fukuoka, Shohei Koyama. ✉e-mail: benno828@bigm.or.jp; hnishika@ncc.go.jp

and the activation of tumour antigen-specific PD-1$^+$CD8$^+$ T cells in the distant TME have not been fully elucidated.

Here, we identified a new bacterial strain, designated YB328, that was significantly enriched in faeces of patients who responded to PD-1 blockade therapies. YB328 accelerated the differentiation of CD103$^+$CD11b$^-$ cDCs, which is an essential DC subset for antigen cross-presentation to CD8$^+$ T cells[24,25]. YB328 mediated cDC differentiation through the phosphorylation of S6K and STAT3 and the induction of IRF8 through the stimulation of multiple Toll-like receptors (TLRs) in the gut. YB328-stimulated CD103$^+$CD11b$^-$ cDCs were further activated by other bacteria and migrated to tumour-draining lymph nodes (dLNs) and the TME. Once in these locations, the cDCs primed and activated CD8$^+$ T cells and induced PD-1$^+$CD8$^+$ T cells specific for a broad range of tumour antigens. Overall, we describe in detail the mechanism of the activation of antigen-specific CD8$^+$ T cells in the distant TME by gut microbiota.

Gut microbiota and antitumour efficacy

We prospectively collected stool samples from 50 Japanese patients with cancer (15 patients with non-small cell lung cancer (NSCLC) and 35 patients with gastric cancer (GC)) who received PD-1 blockade therapy. These patients were classified as responders or non-responders (Supplementary Tables 1 and 2). Clinicopathological features that are reportedly associated with a favourable clinical response to PD-1 blockade (listed in Supplementary Tables 3–5) were not significantly different in our cohort, except for PD-L1 expression by tumour cells in patients with GC. 16S rRNA gene amplicon sequencing of faecal samples showed that the Shannon diversity of gut microbiota was significantly higher in responders than in non-responders (Fig. 1a and Extended Data Fig. 1a,b,f). Receiver operating characteristic (ROC) analysis further showed that the Shannon diversity was a significant predictive biomarker for identifying responders (Fig. 1b and Extended Data Fig. 1c, left, g, left). Moreover, patients with high diversity of gut microbiota exhibited significantly prolonged PFS, regardless of the cancer type (Fig. 1c, Supplementary Table 6 and Extended Data Fig. 1c, right, g, right). Principal coordinate analysis (PCoA) and analysis of similarities (ANOSIM) based on unweighted unique fraction metric (UniFrac) distances revealed a significant difference in gut microbiota between responders and non-responders (Fig. 1d and Extended Data Fig. 1a,d,h). Linear discriminant analysis effect size (LEfSe) showed that members of several families, namely, Ruminococcaceae, Propionibacteriaceae, Dehalobacteriaceae and Turicibacteraceae, were enriched in responders (Fig. 1e,f and Extended Data Fig. 1e,i,j). Among them, Ruminococcaceae abundance was significantly correlated with prolonged PFS after PD-1 blockade therapy and showed the highest AUC score (Fig. 1g and Extended Data Fig. 1k). In contrast to previous reports[1–4,18], the abundance of the genera *Faecalibacterium*, *Enterococcus*, *Bifidobacterium* and *Akkermansia* did not differ significantly between responders and non-responders (Extended Data Fig. 1l). Notably, members of the families Bacteroidaceae and Veillonellaceae, which were enriched in non-responders, were associated with a significantly shorter PFS (Fig. 1e,f,h and Extended Data Fig. 1e,i–k). We also confirmed that patients with high Shannon diversity values, a high abundance of Ruminococcaceae and a low abundance of Bacteroidaceae, when stratified by the median cut-off, had prolonged PFS (Extended Data Fig. 1m).

Among the multiple parameters associated with antitumour immunity, the abundance of PD-1$^+$CD8$^+$ T cells in the TME, which is correlated with the response to PD-1 blockade therapy[12,26–28], was significantly correlated with the abundance of Ruminococcaceae (Fig. 1i–l and Extended Data Fig. 1n). By contrast, the abundance of Bacteroidaceae was associated with a decrease in PD-1$^+$CD8$^+$ T cells and an increase in T_{reg} cell infiltration in the TME (Fig. 1i,m–o). These findings indicate a clear correlation between specific gut microbiota compositions and immune responses.

Gut microbiota regulate antitumour responses

Germ-free (GF) mice colonized with faeces from responders, but not from non-responders, exhibited strong antitumour effects against MC38 tumours after anti-PD-1 monoclonal antibody (anti-PD-1) treatment (Extended Data Fig. 2a,b) and showed increased Shannon diversity in the faeces (Extended Data Fig. 2c). Moreover, Ruminococcaceae was enriched in mice who received faecal microbiota transplantation (FMT) derived from responders (R-FMT), whereas Bacteroidaceae was enriched in mice who received FMT derived from non-responders (NR-FMT) (Extended Data Fig. 2d–g). To exclude the influence of congenital immunodeficiency in GF mice, we performed the same experiments in specific-pathogen-free (SPF) mice preconditioned with antibiotics (ATB-SPF mice). Consistent with GF mice, anti-PD-1 treatment significantly inhibited the growth of MC38 and EMT6 tumours in ATB-SPF mice that received R-FMT (Extended Data Fig. 3a–c). Analyses of the TME demonstrated that activated CD8$^+$ T cells (PD-1$^+$CD8$^+$ T cells and CD62L$^-$CD44$^+$ effector memory CD8$^+$ T cells) and cytokine-producing CD8$^+$ T cells (IFNγ$^+$TNF$^+$) were significantly higher in mice treated with R-FMT and anti-PD-1 than in mice treated with NR-FMT and anti-PD-1 or in control mice (Extended Data Fig. 3d–f). Moreover, tumour-infiltrating PD-1$^+$CD8$^+$ T cells from mice treated with R-FMT and anti-PD-1 exhibited a broader T cell receptor (TCR) Vβ repertoire diversity than mice treated with NR-FMT and anti-PD-1 (Extended Data Fig. 3g–i).

As PD-1 expression by T cells correlates with the strength of T cell activation signalling[13,29], we examined the maturation of DCs in the TME, a process that has a crucial role in T cell activation. The expression levels of DC maturation markers (CD86, CD40 and CD80) were significantly higher in R-FMT-treated mice than in NR-FMT-treated mice (Extended Data Fig. 3j–l). Therefore, gut microbiota augment PD-1 blockade efficacy by promoting mature DC infiltration and PD-1$^+$CD8$^+$ T cell accumulation in the TME.

YB328 promotes antitumour immunity

Given the strong antitumour efficacy of R-FMT, we aimed to isolate bacterial strains from the faeces of responders. A previously undescribed strain, designated YB328, was isolated, and its characteristics were investigated (Fig. 2a, Supplementary Tables 7–9). Taxonomic assignment based on its full-length 16S rRNA gene sequence and the Greengenes database (v.13 8) indicated that strain YB328 belongs to the family Ruminococcaceae. Based on its whole-genome sequence and the Genome Taxonomy Database (GTDB; v.220), strain YB328 was assigned to the recently described species *Hominenteromicrobium mulieris*[30] (Extended Data Fig. 4a), sharing an average 97.3% nucleotide identity to the GTDB species-representative genome. Notably, the family-level name depended on the taxonomic framework, namely, Ruminococcaceae (Greengenes), Oscillospiraceae (NCBI taxonomy) or Acutalibacteraceae (GTDB taxonomy). Moreover, YB328 was detected not only in the Japanese population but also in individuals worldwide (Extended Data Fig. 4b).

We further evaluated the abundance of YB328 in the gut microbiome through metagenome sequencing and species-level quantification using Kraken2 and Bracken against a custom version of the GTDB (v.220). This analysis showed that the abundance of YB328 was significantly higher in the faeces of responders than in non-responders (Fig. 2b). Patients with abundant YB328, defined by a ROC-based cut-off value, had a significantly longer PFS (Fig. 2c), even after excluding patients with high microsatellite instability (Extended Data Fig. 4c). By contrast, *Phocaeicola vulgatus* (represented by strain AE61, a newly isolated strain from this study belonging to the family Bacteriodeceae and enriched in non-responders), showed an increased abundance in non-responders. Moreover, patients with abundant *P. vulgatus* had a shorter PFS (Fig. 2d,e). Similar data were obtained

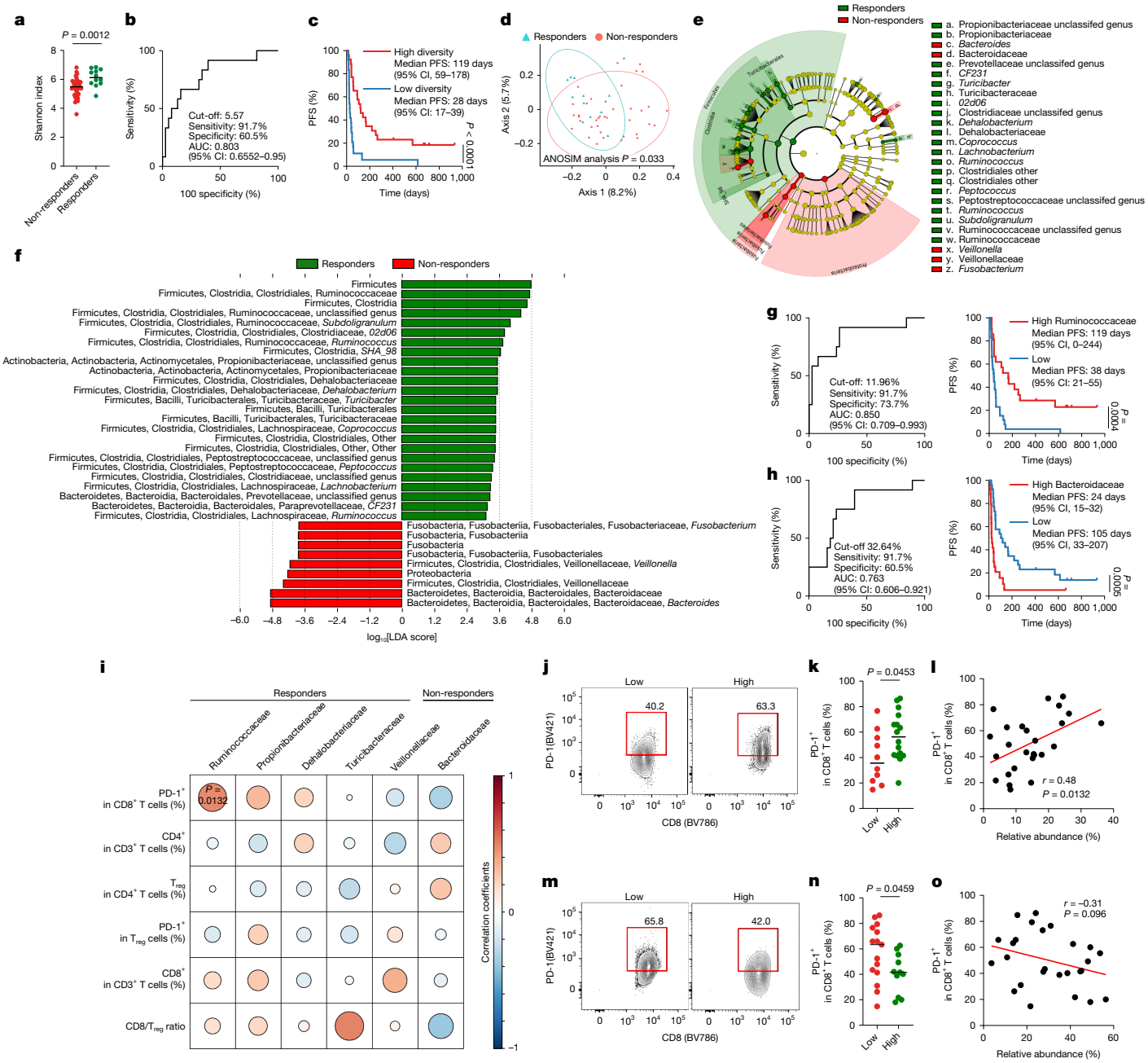

Fig. 1 | The response to PD-1 blockade therapy is correlated with the diversity of gut microbiota and enrichment of Ruminococcaceae in association with the abundance of PD-1$^+$CD8$^+$ T cells in the TME. Faecal samples were collected from patients (n = 15 NSCLC, n = 35 GC) who received PD-1 blockade therapy. **a**, Comparison of Shannon diversity of gut microbiota of responders and non-responders. **b**, ROC analysis of the diversity (Shannon index) of microbiota in faeces. AUC, area under the curve. **c**, Kaplan–Meier curves for PFS of patients with high or low Shannon diversity of gut microbiota. High and low Shannon diversity of gut microbiota in patients were stratified by ROC analysis (**b**). **d**, Differences between gut microbiota of responders and non-responders as visualized by PCoA based on unweighted UniFrac distances. The ellipses represent the 95% confidence intervals (CIs). **e**, Cladogram of differentially abundant taxa identified by LEfSe analysis. Symbol sizes are scaled by the relative abundance. **f**, Linear discriminant analysis (LDA) scores of the significantly different taxa between responders and non-responders. **g**,**h**, ROC analysis (left) and Kaplan–Meier curves (right) for PFS in patients with high or low Ruminococcaceae (**g**) or Bacteroidaceae (**h**) abundance. **i**–**o**, Immune profiles of tumour-infiltrating lymphocytes (TILs) in patients with both biopsy and faecal samples available (n = 4 NSCLC, n = 22 GC). Correlations between subsets of TILs and bacterial families enriched in responders and non-responders (**i**). The frequency of PD-1$^+$CD8$^+$ T cells (representative staining (**j**,**m**) and summary (**k**,**n**)) in patients with high or low abundances of Ruminococcaceae (**k**) or Bacteroidaceae (**n**) stratified by ROC analysis in **g** and **h**. Cells were gated on CD8 TILs (**j**,**m**). The correlation between PD-1 expression by tumour-infiltrating CD8$^+$ T cells and the abundance of Ruminococcaceae (**l**) or Bacteroidaceae (**o**). Significance was assessed using two-sided Mann–Whitney U-test, with data presented as the median (**a**,**k**,**n**); two-sided log-rank test (**c**, **g**, right, **h**, right); ANOSIM with one-tailed significance computed using 999 permutations) (**d**); or two-sided Pearson's correlation (**i**,**l**,**o**).

using the median cut-off value (Extended Data Fig. 4d). As *P. vulgatus* is a well-known commensal bacterium[31], we used the patient-isolated *P. vulgatus* strain AE61 to represent gut microbiota of non-responders and evaluated its effects on immunotherapy responses in animal models together with YB328. Although YB328 administration alone did not inhibit tumour growth (Extended Data Fig. 4e), YB328 augmented

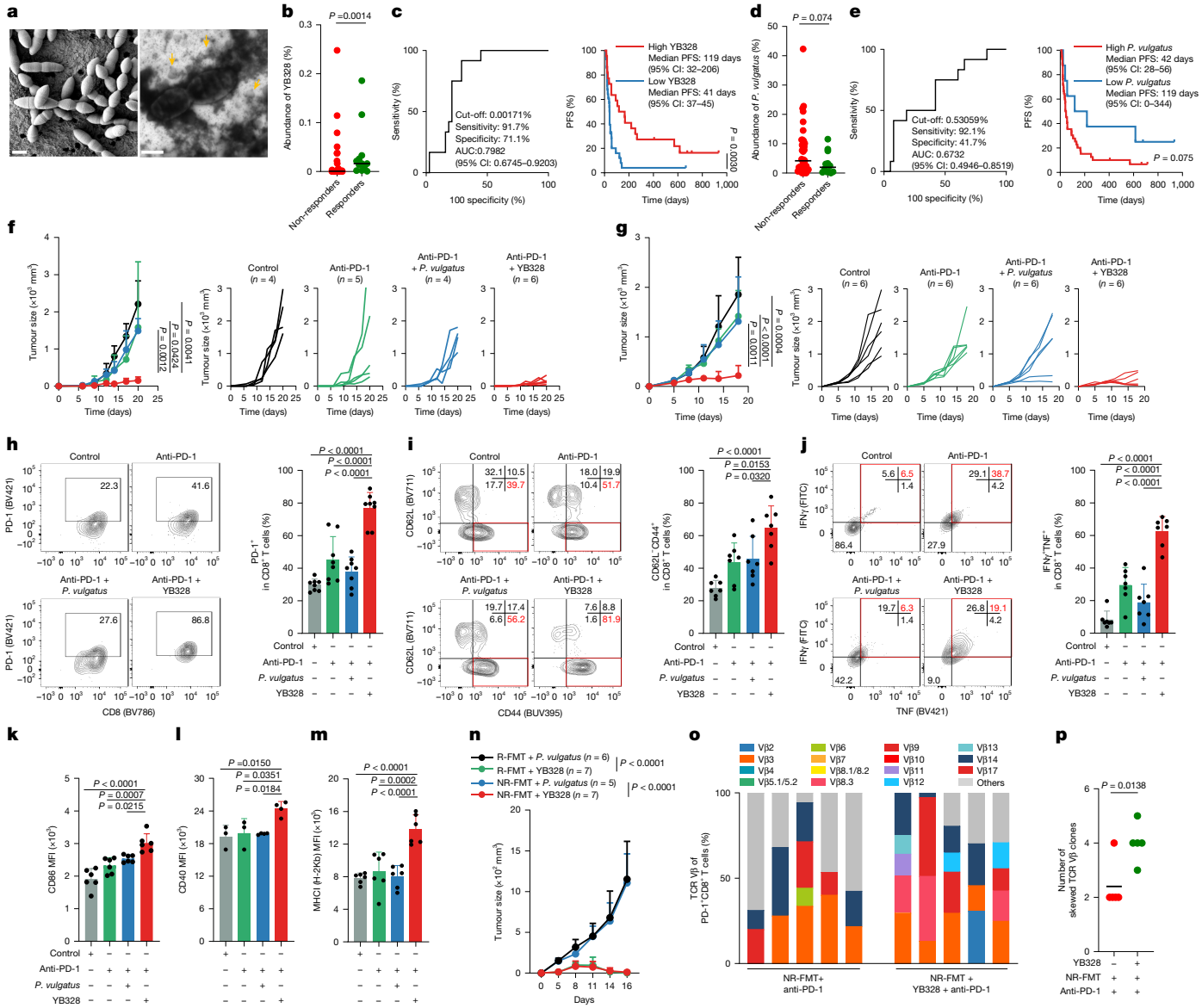

Fig. 2 | YB328 colonization restores responsiveness to anti-PD-1 treatment. **a**–**e**, The morphological traits of YB328. **a**, Left, scanning electron microscopy image. Scale bar, 1 µm. Right, transmission electron microscopy image of negatively stained cells. The arrows indicate extracellular membrane vesicles secreted by YB328. Scale bar, 0.5 µm. **b**,**d**, Relative abundances of YB328 (**b**) and *P. vulgatus* (**d**) in faecal samples of patients shown in Fig. 1a–h ($n = 50$). **c**,**e**, ROC curves (left) and Kaplan–Meier curves (right) of the PFS of patients with high or low abundances of YB328 (**c**) or *P. vulgatus* (**e**) in faeces. **f**,**g**, Tumour growth curves of SPF mice with B16F10 (**f**) or MC38 (**g**) tumours (left, summary; right, each mouse). $n = 4$–6 mice per group. Here and in other figures, control indicates mice treated with an isotype control antibody. **h**–**j**, The frequency (representative staining (left) and summary (right)) of PD-1 (**h**, $n = 8$), CD62L and CD44 (**i**, $n = 7$) and IFNγ and TNF production (**j**, $n = 7$) by CD8⁺ T cells in MC38 tumours. Cells were gated on CD8⁺ TILs (**h**–**j**). **k**–**m**, The mean fluorescent intensity (MFI) of CD86 (**k**, $n = 6$), CD40 (**l**, control or anti-PD-1, $n = 3$, *P. vulgatus* or YB328, $n = 4$) and H-2Kb (a marker for MHCI) (**m**, $n = 6$) by CD11c⁺MHCII⁺ DCs in MC38 tumours. **n**–**p**, Tumour growth curves (**n**, $n = 5$–7 mice per group), TCR Vβ repertoire (**o**) and numbers of skewed TCR Vβ clones (>10% of each clone) (**p**) among PD-1⁺CD8⁺ T cells ($n = 5$ mice per group). For **b** and **d**, each dot indicates one patient, and the data are presented as the median. For **f** (left), **g** (left) and **n**, the average tumour sizes of the groups on a certain day are shown as dots and are presented as the mean ± s.d. For **h**–**m** and **p**, each dot in the summary graphs indicates one mouse. Data are presented as the mean ± s.d. (**h**–**m**) or median (**p**). Significance was assessed using two-sided Mann–Whitney *U*-test (**b**,**d**,**p**), two-sided log-rank test (**c**, right, **e**, right), two-way analysis of variance (ANOVA) with the Tukey–Kramer method (**f**,**g**,**n**) or one-way ANOVA with Bonferroni correction (**h**–**m**).

the antitumour effect of anti-PD-1 treatment more than *P. vulgatus* in ATB-SPF mice. This effect was observed in both poorly immunogenic B16F10 and immunogenic MC38 tumour models, with colonization beyond the gavage period (Fig. 2f,g and Extended Data Fig. 4f). Other bacterial strains enriched and isolated from the faeces of responders exhibited few or no antitumour effects compared with YB328 and PD-1 blockade therapy (Extended Data Fig. 4g).

Mice treated with YB328 and anti-PD-1 had higher abundances of activated CD8⁺ T cells and cytokine-producing CD8⁺ T cells in the TME than mice treated with *P. vulgatus* and anti-PD-1 or control mice (Fig. 2h–j and Extended Data Fig. 5a–c). However, the frequencies of T_{reg} cells and PD-1⁺ T_{reg} cells were comparable across groups (Extended Data Fig. 5d,e). Nevertheless, DCs in the TME of YB328-colonized mice exhibited significantly increased expression of co-stimulatory molecules (Fig. 2k,l and Extended Data Fig. 5f) and recapitulated the phenotypes of DCs in mice that received R-FMT. Moreover, major histocompatibility class I (MHCI) expression was significantly upregulated in these DCs (Fig. 2m). Taken together, these results

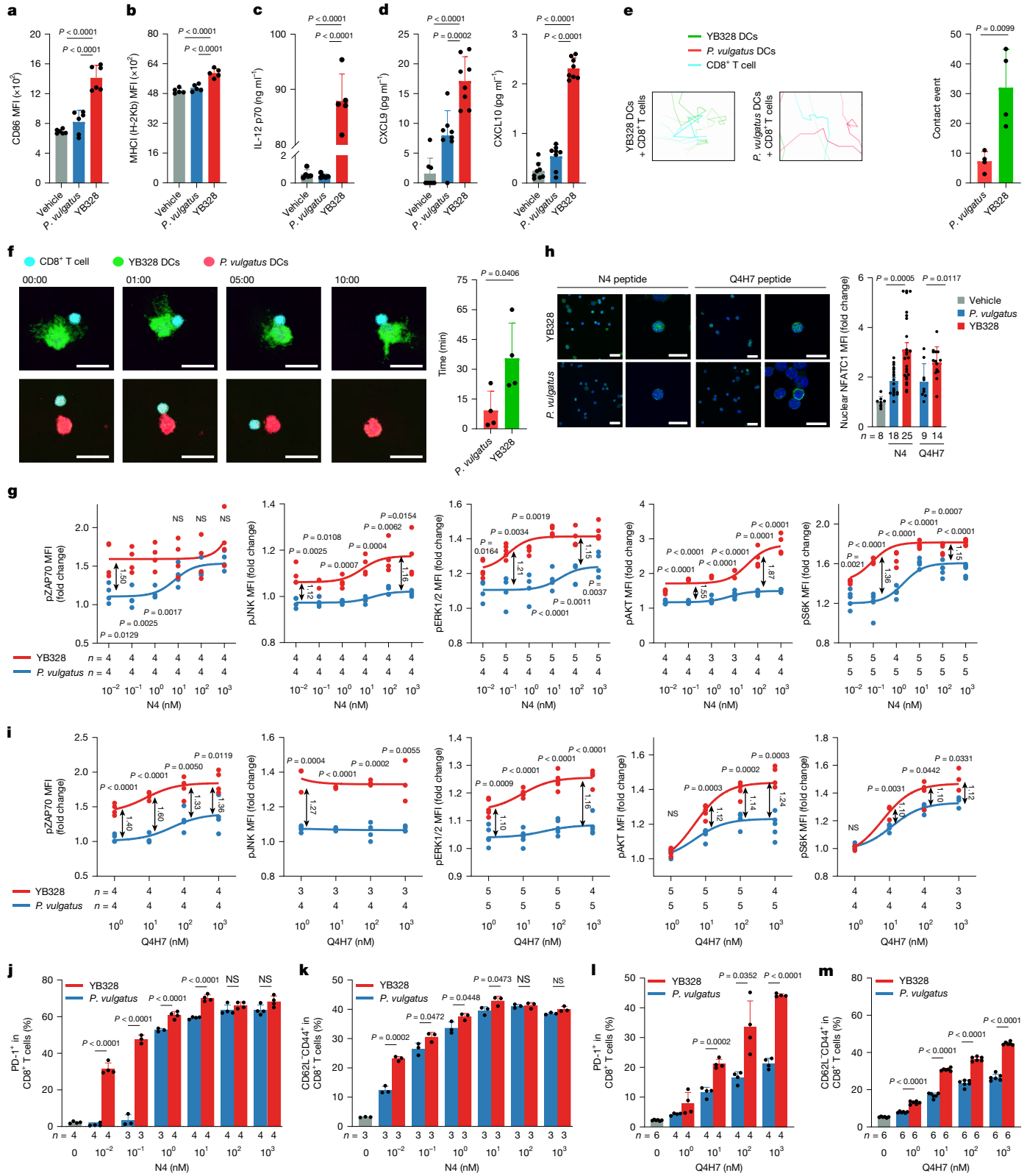

Fig. 3 | See next page for caption.

suggest that YB328 colonization induces DC maturation with high efficiency antigen presentation to activate tumour-infiltrating CD8$^+$ T cells. Furthermore, the administration of YB328, but not *P. vulgatus*, favourably changed the Shannon diversity of gut microbiota (Extended Data Fig. 5g).

YB328 redirects treatment sensitivity

ATB-SPF mice treated with NR-FMT and colonized with YB328, but not *P. vulgatus*, showed increased sensitivity to anti-PD-1 therapy (Fig. 2n and Extended Data Fig. 5h,i). Moreover, YB328 administration increased

Fig. 3 | YB328-stimulated BMDCs reduce the activation threshold of CD8$^+$ T cells to induce PD-1 expression. a–**d**, BMDCs were stimulated with YB328 or *P. vulgatus*. MFI summaries of the maturation markers CD86 (**a**, *n* = 6 wells per group) and H-2Kb (**b**, *n* = 5 wells per group), IL-12p70 production (**c**, *n* = 5 wells per group) and chemokine (CXCL9 and CXCL10) expression (**d**, *n* = 8 wells per group) in BMDCs are shown. **e**,**f**, Dynamic imaging of CD8$^+$ T cells and BMDCs stimulated with YB328 or *P. vulgatus*. **e**, Contact events were evaluated at 10-min intervals (right), and a representative trajectory of the indicated cell (left) was extracted from Supplementary Video 1. **f**, Images showing the interaction between DCs and CD8$^+$ T cells. The elapsed time is shown in minutes and seconds. *n* = 4 cells per group. Scale bars, 10 µm. **g**–**m**, OT-I CD8$^+$ T cells were cultured with bacteria-treated BMDCs pulsed with the indicated concentrations of antigen peptides. **g**,**i**, Expression levels of TCR signalling molecules by CD8$^+$ T cells induced by N4 peptide (**g**) or Q4H7 peptide (**i**). NS, not significant. **h**, Representative confocal images of NFATC1 nuclear translocation (left) and MFI summary (right) Scale bars, 20 µm (first and third columns) and 10 µm (second and fourth columns). **j**–**m**, The frequency of expression of the effector molecules PD-1 (**j**,**l**) and CD62L and CD44 (**k**,**m**) in CD8$^+$ T cells induced by treatment with N4 peptide (**j**,**k**) or Q4H7 peptide (**l**,**m**). Each dot in the summary graphs indicates a well (**a**–**d**,**g**–**m**), and the data are presented as the mean ± s.d. (**a**–**f**,**h**,**j**–**m**) or the mean (**g**,**i**). Significance was assessed using one-way ANOVA with Bonferroni correction (**a**–**d**) or two-sided unpaired *t*-test (**e**–**m**).

the diversity of the TCR Vβ repertoire of tumour-infiltrating PD-1$^+$CD8$^+$ T cells among skewed TCRs in these mice (Fig. 2o,p and Extended Data Fig. 5j). The administration of YB328, but not *P. vulgatus*, favourably altered the Shannon diversity of gut microbiota (Extended Data Fig. 5k). Consistently, in our GC and NSCLC cohort of patients, increased levels of YB328 were positively correlated with the Shannon diversity of gut microbiota (Extended Data Fig. 5l).

However, the co-administration of YB328 and *P. vulgatus* abolished the antitumour immunity induced by YB328 (Extended Data Fig. 5m). This effect was in contrast to YB328 single administration in mice treated with NR-FMT, which showed effective induction of antitumour immunity in combination with anti-PD-1 treatment. The co-administration of *P. vulgatus* prevented the colonization of YB328 in ABT-SPF mice. However, YB328 sufficiently colonized the gut of mice treated with NR-FMT at a similar level to that observed with YB328 administration alone. This finding indicated that YB328 colonization is not significantly influenced by the microbial environment shaped by NR-FMT (Extended Data Fig. 5n). Indeed, *P. vulgatus* administration led to significantly greater engraftment of *P. vulgatus* than NR-FMT (Extended Data Fig. 5o). These observations underscore the impact of competitive dominance on the efficacy of microbiome-based therapies.

YB328-treated DCs activate CD8$^+$ T cells

To understand the mechanisms of DC maturation, we analysed bone-marrow-derived DCs (BMDCs) treated with *P. vulgatus* or YB328. Compared with *P. vulgatus*-treated BMDCs, YB328-treated BMDCs were larger and presented multiple pseudopodia. Moreover, they had increased expression of CD86, CD80 and MHCI and increased levels of IL-12p70 and the chemokines CXCL9, CXCL10 and CCL5 (Fig. 3a–d and Extended Data Fig. 6a–c). When ovalbumin (OVA)-specific (OT-I) TCR transgenic CD8$^+$ T cells were cultured with bacteria-treated DCs pulsed with OVA peptides, YB328-treated BMDCs were more strongly attracted and were in contact with CD8$^+$ T cells for a longer time than *P. vulgatus*-treated BMDCs (Fig. 3e,f and Supplementary Videos 1–3). No difference was observed in CCL22 production, which recruits T_{reg} cells, among YB328-treated, *P. vulgatus*-treated and unstimulated BMDCs (Extended Data Fig. 6c). This result is consistent with the comparable T_{reg} cell infiltration levels observed in the TME across treatments.

OT-I CD8$^+$ T cells were cultured with DCs and then pulsed with different OVA peptides capable of delivering titrated levels of TCR signalling[32]. YB328-treated and *P. vulgatus*-treated BMDCs pulsed with higher doses (100 nM to 1 µM) of high-affinity OVA peptide (N4) presented comparable levels of phosphorylated ZAP70. When BMDCs were pulsed with lower doses (0.01 nM to 10 nM) of N4, YB328-treated BMDCs, but not *P. vulgatus*-treated BMDCs, exhibited ZAP70 phosphorylation. YB328-treated BMDCs also stimulated strong phosphorylation of co-stimulatory signals (pJNK, pERK1 and pERK2 (pERK1/2), pAKT and pS6K) in CD8$^+$ T cells (Fig. 3g and Extended Data Fig. 7a). YB328-treated BMDCs pulsed with a low dose (10 nM) of the N4 peptide induced extensive NFATC1 nuclear translocation in CD8$^+$ T cells, whereas *P. vulgatus*-treated BMDCs induced only limited translocation (Fig. 3h). YB328-treated BMDCs pulsed with N4 peptides, regardless of the dose, were correlated with the successful activation of and increased cytokine production by CD8$^+$ T cells, whereas *P. vulgatus*-treated BMDCs induced PD-1 expression only when pulsed with high N4 doses (Fig. 3j,k and Extended Data Fig. 7b–d). Moreover, when supplied with low-affinity OVA peptide (Q4H7), YB328-treated BMDCs induced ZAP70 phosphorylation and co-stimulatory signalling (Fig. 3i and Extended Data Fig. 7e) at relatively high doses and promoted the nuclear translocation of NFATC1 in CD8$^+$ T cells (Fig. 3h). YB328-treated BMDCs consistently induced increased PD-1 expression, which correlated with the activation of and cytokine production by CD8$^+$ T cells, regardless of the dose (Fig. 3l,m and Extended Data Fig. 7f–h).

YB328 enhances the differentiation of cDCs

Analysis of the transcriptional profile revealed higher expression of *Irf8* and *Batf3* in YB328-treated DCs than in *P. vulgatus*-treated DCs and untreated DCs (Fig. 4a–c). BATF3 maintains IRF8 autoactivation to commit to the terminal differentiation of CD103$^+$CD11b$^-$ cDCs, which have a crucial role in antitumour immunity by effectively activating CD8$^+$ T cells[33,34]. Accordingly, the number of CD103$^+$CD11b$^-$ cDC progenies increased in response to YB328 treatment (Fig. 4d and Extended Data Fig. 8a). By contrast, IRF4, which is a key transcription factor of CD103$^-$CD11b$^+$ cDCs[35], was highly expressed by *P. vulgatus*-treated DCs (Fig. 4e). To further understand the mechanisms of CD103$^+$CD11b$^-$ cDC differentiation induced by YB328 treatment, common DC progenitors (CDPs) were cultured with YB328 or *P. vulgatus* and with FLT3 ligand (FLT3L), a factor essential for the differentiation of CDPs into CD103$^+$CD11b$^-$ cDCs[36,37]. IRF8 expression was significantly upregulated in CDPs stimulated with YB328 at low concentrations of FLT3L, although IRF8 expression was comparable between the groups treated with high concentrations of FLT3L (Fig. 4f). This result suggests that YB328 activates an alternative signalling pathway in CDPs that compensates for FLT3L signalling. FLT3L treatment promotes both PI3K–mTOR and STAT3 signalling for the development of CD103$^+$CD11b$^-$ cDCs[38,39], and these two pathways regulate *Batf3* expression[40,41]. YB328 stimulation increased levels of S6K and STAT3 phosphorylation compared with *P. vulgatus* stimulation (Fig. 4g,h). YB328-induced *Irf8* expression was reduced by an S6K inhibitor (rapamycin) or a STAT3 inhibitor (HJC0152) and was more significantly inhibited by the administration of both inhibitors (Fig. 4i). Consequently, the number of CD103$^+$CD11b$^-$ cDCs induced by YB328 stimulation was decreased by rapamycin and/or HJC0152 treatment (Fig. 4j). The antitumour effects induced by combination treatment with YB328 and anti-PD-1 were completely abrogated in *Batf3*$^{-/-}$ mice, which lack a subset of CD103$^+$CD11b$^-$ cDCs[42] (Fig. 4k and Extended Data Fig. 8b–d). By contrast, the depletion of macrophages with an anti-CSF1R monoclonal antibody did not affect the antitumour efficacy induced by YB328 and anti-PD-1 treatment (Extended Data Fig. 8e,f). Moreover, YB328-stimulated macrophages were less effective in activating CD8$^+$ T cells than YB328-stimulated DCs (Extended Data Fig. 8g). These data provide further support for the importance of CD103$^+$CD11b$^-$ cDCs in YB328-driven antitumour activity.

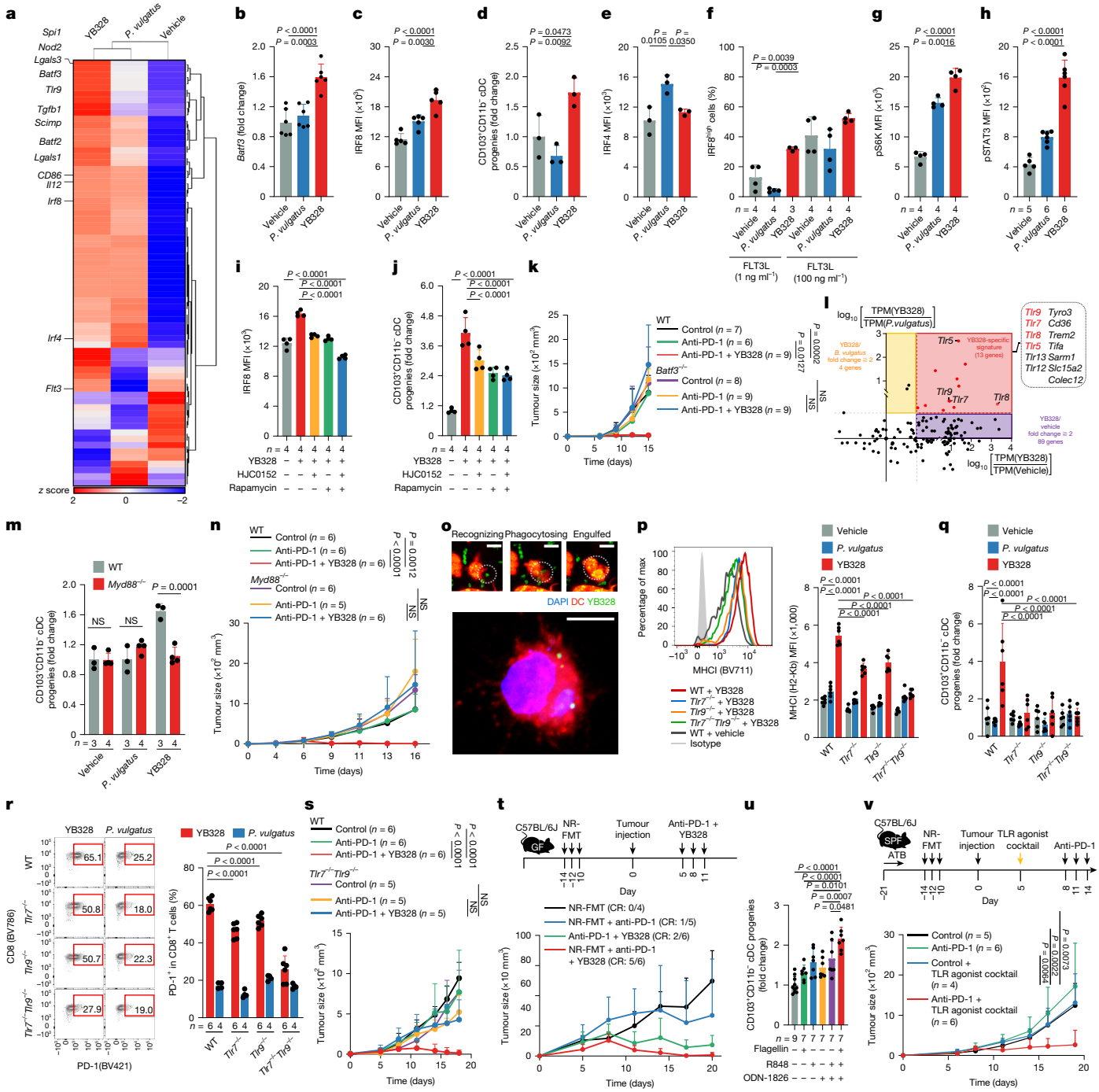

Fig. 4 | YB328 increases IRF8 expression to promote CD103⁺CD11b⁻ cDC generation through TLR signalling to augment antitumour immunity. **a**–**e**, DCs were treated with *P. vulgatus*, YB328 or vehicle. Comprehensive gene expression was examined (**a**), as was the expression of *Batf3* (**b**, $n = 6$), IRF8 (**c**, $n = 5$), IRF4 (**e**, $n = 3$) and changes in the progeny of the CD103⁺CD11b⁻ cDCs (**d**, $n = 3$). **f**, IRF8 expression by CDPs treated with bacteria and Flt3L as indicated, $n = 3$–4. **g**–**j**, BMDCs were treated with the indicated stimuli, and expression of pS6K (**g**), pSTAT3 (**h**) and IRF8 (**i**) and changes in the progeny of CD103⁺CD11b⁻ cDCs (**j**) were examined ($n = 4$–6). **k**, Tumour growth curves of wild-type (WT) and *Batf3*$^{-/-}$ mice ($n = 6$–9) treated as indicated. **l**, Gene expression signatures of BMDCs stimulated with YB328 were extracted. Red text indicates TLR proteins that were highly expressed in the YB328-specific signature. TPM, transcripts per million. **m**, Changes in the progeny of CD103⁺CD11b⁻ cDCs ($n = 3$–4). **n**, Tumour growth curves of WT and *Myd88*$^{-/-}$ mice ($n = 5$–6) treated as indicated. **o**, Representative confocal images of the engulfment of YB328 by BMDCs. Scale bars, 5 µm. **p**,**q**, The expression of MHCI (**p**; gated on CD11c⁺MHCII⁺ cells) and the changes in the progeny of CD103⁺CD11b⁻ cDCs (**q**) ($n = 6$). Max, maximum. **r**, Frequency of PD-1 expression in CD8⁺ T cells ($n = 4$–6). **s**, Tumour growth curves of WT and *Tlr7*$^{-/-}$*Tlr9*$^{-/-}$ mice ($n = 5$–6) treated as indicated. **t**, Experimental scheme (top) and tumour growth curves (bottom). The number of mice showing a complete response (CR) in $n = 4$–6 mice is shown in parentheses. **u**, Changes in the progeny of CD103⁺CD11b⁻ cDCs ($n = 7$–9). **v**, Experimental scheme (top) and tumour growth curves (bottom). $n = 4$–6 mice. Each dot in the summary graphs indicates a well (**b**–**j**,**m**,**p**–**r**,**u**). The average tumour size of the groups on a certain day is shown as a dot (**k**,**n**,**s**,**t**,**v**). The data are presented as the mean ± s.d. Significance was assessed using one-way ANOVA with Bonferroni's correction (**b**–**j**,**p**–**r**,**u**), two-way ANOVA with the Tukey–Kramer method (**k**,**n**,**s**,**v**) or two-sided unpaired Student's *t*-test (**m**).

YB328 stimulates multiple TLR pathways

We next investigated how YB328 stimulates multiple signalling pathways in DCs. The expression of TLR family members, particularly TLR5 and TLR7–TLR9, was markedly upregulated in YB328-treated BMDCs compared with *P. vulgatus*-treated or untreated BMDCs (Fig. 4l). Similarly, YB328 administration increased the diversity of TLR expression by DCs in the gut-associated lymphoid tissues (GALTs) of mice treated with NR-FMT (Extended Data Fig. 9a).

The adaptor protein MYD88 mediates the downstream signalling pathways of TLR5 and TLR7–TLR9 (ref. 43). *Myd88*$^{-/-}$ BMDCs treated with YB328 did not lead to increases in the number of CD103^{+}CD11b^{-} cDC progeny (Fig. 4m). Moreover, the increase in antitumour efficacy induced by YB328 and anti-PD-1 treatment was abrogated in *Myd88*$^{-/-}$ mice (Fig. 4n and Extended Data Fig. 9b). The frequency of CD103^{+}CD11b^{-} cDCs was significantly lower in the lamina propria and Peyer's patch, but not in the spleen, of *Myd88*$^{-/-}$ mice than in wild-type mice (Extended Data Fig. 9c). This result suggests that YB328-triggered CD103^{+}CD11b^{-} cDC generation requires the activation of MYD88 signalling.

As YB328 is not flagellated (Fig. 2a), the ability of YB328 to stimulate endosomal TLRs (TLR7–TLR9) to promote the differentiation of CD103^{+}CD11b^{-} cDCs was examined. YB328 was phagocytosed by BMDCs (Fig. 4o and Supplementary Video 4). The stimulation of THP-1-based TLR7, TLR8 and TLR9 reporter cells revealed that YB328 activated both the IRF and NF-κB signalling pathways (Extended Data Fig. 9d). As mouse TLR8 is nonfunctional[44], the roles of TLR7 and TLR9 in YB328-mediated antitumour immunity were investigated. BMDCs derived from *Tlr7*$^{-/-}$ or *Tlr9*$^{-/-}$ mice partially reduced the upregulation of MHCI expression (Fig. 4p) and abrogated the differentiation of CD103^{+}CD11b^{-} cDCs induced by YB328 (Fig. 4q). Furthermore, BMDCs derived from *Tlr7*$^{-/-}$ *Tlr9*$^{-/-}$ mice did not respond to YB328. Therefore increased MHCI expression, differentiation into CD103^{+}CD11b^{-} cDCs and induction of the production of PD-1-expressing CD8^{+} T cells were not observed in these cells (Fig. 4p–r). YB328 administration to *Tlr7*$^{-/-}$*Tlr9*$^{-/-}$ mice did not augment the antitumour efficacy of anti-PD-1 treatment (Fig. 4s and Extended Data Fig. 9e). These data suggest that endosomal TLR7–TLR9 are key mediators of YB328-induced antitumour immunity.

Multiple TLR ligands sensitize DCs

YB328 induced TLR5 expression in DCs. However, YB328 probably does not have genes encoding components of flagellum, based on whole-genome sequence annotation, and flagella were not detected by electron microscopy (Fig. 2a). Therefore, we examined whether TLR ligands such as flagellin derived from the gut microbiome could further augment the antitumour immunity induced by YB328-stimulated DCs. PD-1 expression by CD8^{+} T cells stimulated with YB328-treated DCs, but not those stimulated with *P. vulgatus*, was significantly increased after flagellin treatment (Extended Data Fig. 9f). Although treatment with YB328 and anti-PD-1 inhibited tumour growth, combined treatment with NR-FMT, which contained a pool of TLR ligands, led to enhanced antitumour efficacy (Fig. 4t and Extended Data Fig. 9g). Therefore, YB328 sensitizes DCs to multiple TLR ligands derived from not only YB328 but also from other gut microbes to augment antitumour immunity.

TLR signalling mimics YB328 stimulation

As YB328 upregulated multiple TLRs in DCs, we explored whether the combined activation of TLR signalling recapitulated the phenotype of YB328-treated DCs. BMDCs treated with the TLR agonist R848 or ODN-1826 exhibited increased S6K and STAT3 phosphorylation, and combination treatment further increased the phosphorylation of both these proteins. The triple combination of flagellin, R848 and ODN-1826 led to the most effective induction of S6K and STAT3 phosphorylation, which in turn resulted in the highest levels of IRF8 expression and the strongest induction of CD103^{+}CD11b^{-} cDCs out of all the treatment combinations (Fig. 4u and Extended Data Fig. 9h). Moreover, combination treatment with an anti-PD-1 and a TLR agonist cocktail—at doses in which each agonist alone was insufficient to completely control tumour growth (Extended Data Fig. 9i)—significantly inhibited tumour growth (Fig. 4v and Extended Data Fig. 9j).

YB328 shows specific antitumour features

We next examined whether the immunomodulatory functions of YB328 are specific to this strain. Five representative bacterial strains were chosen for analysis: one strain isolated from the faeces of responders (*Ruminococcus torques* AE30) and four strains from species phylogenetically close to YB328 (the type strains of the species *Ruminococcus albus, Clostridium leptum*, *Acutalibacter muris* and *Neglectibacter timonensis*) (Extended Data Fig. 4a). Among these, YB328 treatment led to the most significant induction of PD-1 expression in CD8^{+} T cells (Extended Data Fig. 10a) and specifically augmented antitumour effects of anti-PD-1 compared with the other selected bacteria (Extended Data Fig. 10b). We then compared the whole-genome sequences of YB328, the five bacterial strains that lacked antitumour efficacy and *P. vulgatus* (Extended Data Fig. 10c–f, Supplementary Table 10 and Supplementary Discussion). Different cellular fractions of YB328 were also prepared to determine which components of YB328 were responsible for its antitumour activity (Extended Data Fig. 10g and Supplementary Discussion).

We also analysed whether the bacteria *Akkermansia muciniphila*[1,15] and *Bifidobacterium longum*[3,4], which reportedly improve responses to cancer immunotherapy, possessed properties similar to those of YB328. *A. muciniphila*, but not *B. longum*, exhibited a significant antitumour effect when combined with anti-PD-1 treatment (Extended Data Fig. 10h). *A. muciniphila*-treated BMDCs promoted CD103^{+}CD11b^{-} cDC differentiation, which in turn induced PD-1 expression by CD8^{+} T cells (Extended Data Fig. 10i,j). However, *A. muciniphila* induced the expression of IRF8 but not S6K or STAT3 phosphorylation in DCs (Extended Data Fig. 10k–m). Together, these results demonstrate the uniqueness of YB328.

YB328 mobilizes cDCs to tumour lesions

We next investigated the location of CD103^{+}CD11b^{-} cDC differentiation and CD8^{+} T cell activation. The abundance of CD103^{+}CD11b^{-} cDCs, but not CD103^{-}CD11b^{+} DCs, in the lamina propria and Peyer's patch was significantly higher after YB328 treatment than after *P. vulgatus* treatment (Fig. 5a,b). The frequencies of migratory CD103^{+}CD11b^{-} cDCs were also significantly increased in the dLNs (inguinal LNs) and the TME of mice treated with YB328 and anti-PD-1 (Fig. 5c,d). Moreover, the frequency of CD103^{+}CD11b^{-} cDCs was comparable to that observed after *P. vulgatus* treatment in tumour nondraining LNs (NdLNs: inguinal LNs on the opposite flank of the tumour) and the spleen (Extended Data Fig. 11a,b). CD103^{+}CD11b^{-} cDCs in the mesenteric lymph nodes (MLNs) of mice treated with YB328 exhibited significantly increased expression of CCR7, a crucial chemokine receptor for migration[45,46] (Fig. 5e). PD-1^{+}CD8^{+} T cells co-expressing TCF-1 significantly proliferated in the tumour dLNs, but not in the MLNs, of YB328-treated mice, and this phenotype was not observed in *P. vulgatus*-treated mice (Fig. 5f and Extended Data Fig. 11c).

We next used mice expressing photoconvertible Kikume green-red (KikGR) to trace intestinal immune cells (Fig. 5g). In contrast to those in *P. vulgatus*-treated mice, intestinal immune cells (KikR^{+} cells) showed substantial infiltration in the tumour dLNs of YB328-treated mice (Fig. 5h). The intestinal infiltration of KikR^{+}CD103^{+}CD11b^{-} cDCs into the dLNs and MLNs was higher in YB328-treated mice than in *P. vulgatus*-treated mice but was not higher in NdLNs, spleens or cervical lymph nodes (Fig. 5i and Extended Data Fig. 11d). Moreover, treatment with YB328, but not *P. vulgatus*, increased the abundance of

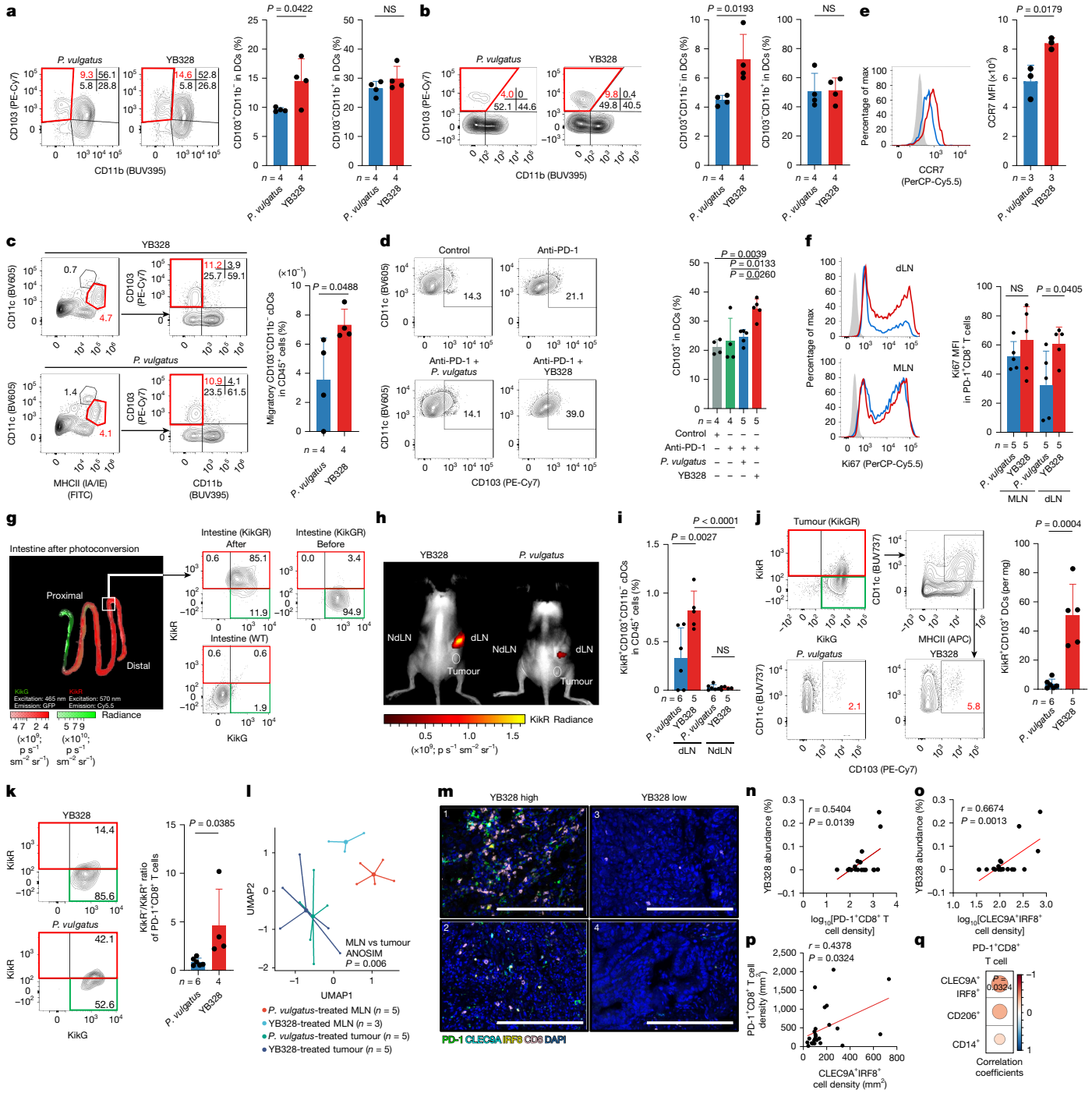

Fig. 5 | YB328 treatment promotes the differentiation and migration of CD103$^+$CD11b$^-$ cDCs to the distant TME and primes and activates CD8$^+$ T cells. **a**–**f**, ATB-SPF mice were subcutaneously injected with MC38 cells and treated with the indicated bacteria. The phenotype and frequency (representative staining (left) and frequency (right)) of DC populations in lamina propria (gated on CD11c$^+$MHCII$^+$ cells) (**a**), Peyer's patch (gated on CD11c$^+$MHCII$^+$ cells) (**b**), dLNs (gated on live CD45$^+$ cells) (**c**) and tumour (gated on CD11c$^+$MHCII$^+$ cells) (**d**). Expression (representative staining (left) and MFI summary (right)) of CCR7 by CD103$^+$CD11b$^-$ cDCs in the MLNs (**e**, $n = 3$). Expression (representative staining (left) and MFI summary (right)) of Ki67 by PD-1$^+$CD8$^+$ T cells in dLNs and MLNs (**f**, $n = 5$; gated on PD-1$^+$CD8$^+$CD3$^+$ cells). **g**, Representative image (left) and staining (right) of KikG-expressing or KikR-expressing intestinal cells (gated on CD45$^+$ cells). **h**, A representative image of the localization of migrated intestinal cells after the indicated bacterial treatment. **i**, The frequency of KikR$^+$CD103$^+$CD11b$^-$ cDCs in CD45$^+$ cells in dLNs and NdLNs. **j**, KikR$^+$CD103$^+$ DCs (representative staining (left) and number summary (right)) in tumours (per mg) (gated on CD45$^+$ cells). **k**, The KikR$^-$/KikR$^+$ ratio of PD-1$^+$CD8$^+$ T cells (representative staining (left) and ratio summary (right)) in tumours. Cells were gated on PD-1$^+$CD8$^+$CD3$^+$ cells. **l**, The TCR Vβ repertoire in CD8$^+$ T cells in the indicated organs. For **i**–**l**, $n = 3$–6 mice per group. For **a**–**l**, each dot in the summary graphs indicates one mouse. The data are presented as the mean ± s.d. **m**–**q**, Assays in human samples. **m**, Representative multiplex immunohistochemical staining of tumours from patients with GC. Scale bars, 200 μm. **n**,**o**, Correlation between the YB328 abundance in the faeces of patients and the density of PD-1$^+$CD8$^+$ T cells (**n**) or CLEC9A$^+$IRF8$^+$ cells (**o**). $n = 20$ patients. **p**,**q**, Correlation between PD-1$^+$CD8$^+$ T cells and CLEC9A$^+$IRF8$^+$ cells (**p**) and correlation coefficients between PD-1$^+$CD8$^+$ T cells and other immune cells (**q**). $n = 24$ patients. For **n**–**p**, each dot indicates one patient, and the relative correlation was assessed by two-sided Pearson's correlation. Significance was assessed using two-sided unpaired Student's *t*-test (**a**–**c**,**e**,**f**,**j**–**k**), one-way ANOVA with Bonferroni correction (**d**,**i**) or ANOSIM with one-tailed significance using 999 permutations (**l**).

KikR$^+$CD103$^+$ DCs and the number of KikR$^-$PD-1$^+$CD8$^+$ T cells in the TME (Fig. 5j,k). Although the frequency of KikR$^+$PD-1$^+$CD8$^+$ T cells was slightly increased in the MLNs of YB328-treated mice, the TCR Vβ repertoire of tumour-infiltrating CD8$^+$ T cells was significantly different from that of CD8$^+$ T cells in MLNs (Fig. 5l and Extended Data Fig. 11e), which indicated that there was local activation of tumour-antigen-specific CD8$^+$ T cells. By contrast, the frequencies of KikR$^+$PD-1$^+$CD8$^+$ T cells and KikR$^+$CD11b$^+$ cells were comparable in the dLNs, NdLNs, spleens and cervical lymph nodes after YB328 or *P. vulgatus* administration. However, KikR$^+$FOXP3$^+$ T cells were slightly increased in the dLNs of YB328-treated mice (Extended Data Fig. 11e–g). Moreover, YB328 itself was not detected in the tumour (Extended Data Fig. 11h). These data support the notion that YB328 promotes the migration of intestinal CD103$^+$CD11b$^-$ cDCs into tumour dLNs and the TME and primes and activates CD8$^+$ T cells in situ, which augments the antitumour efficacy of PD-1 blockade treatment.

YB328 augments human antitumour effects

YB328 abundance was significantly associated with the infiltration of PD-1$^+$CD8$^+$ T cells and IRF8$^+$CLEC9A$^+$ DCs, which correspond to mouse CD103$^+$CD11b$^-$ cDCs[25], in the TME of patients treated with PD-1 blockade therapies (Fig. 5m–o and Extended Data Fig. 12a,b). The abundance of PD-1$^+$CD8$^+$ T cells was significantly correlated with that of IRF8$^+$CLEC9A$^+$ DCs but not with that of CD206$^+$ or CD14$^+$ cells (Fig. 5p,q and Extended Data Fig. 12c).

We confirmed these findings in our validation cohort (GC, $n = 14$; NSCLC, $n = 7$; collected from January 2018 to September 2018; see Methods) (Supplementary Tables 1–5). In accordance with our discovery cohort (GC, $n = 35$; NSCLC, $n = 15$; collected from March 2017 to December 2017; see Methods), the presence of YB328 in gut microbiota showed a clear correlation with a favourable clinical outcome, and patients with abundant YB328 exhibited a significantly longer PFS (Extended Data Fig. 12d,e). In a prospective cohort of patients with head and neck squamous cell carcinoma (HNSCC) (Supplementary Table 11), the YB328 phylotype was more abundant in the faeces of the responder group than in the non-responder group (Extended Data Fig. 12f). We also analysed datasets from the Japanese nationwide MONSTAR project (MONSTAR cohort)[47] (Supplementary Table 12). Patients with malignant melanoma (MM) in the MONSTAR cohort had a higher abundance of *Akkermansia* in the responder group than in the non-responder group, as previously observed[1]. Moreover, YB328 was more abundant in the responder group of not only patients with MM and in patients with renal cell carcinoma, both of which are known to be immunotherapy-favourable cancer types, but also in patients with GC (thereby validating our results) and in patients with oesophageal cancer (Extended Data Fig. 12g). Furthermore, in a public dataset[48] from patients with MM treated with anti-PD-1, responders exhibited significantly higher YB328 colonization than non-responders 3 months after FMT and anti-PD-1 treatment (Extended Data Fig. 12h). Thus, a high abundance of YB328 in faeces correlates with responsiveness to anti-PD-1 treatment in multiple types of cancer. Similarly, YB328 treatment also significantly increased the antitumour efficacy of the adoptive cell transfer of tumour antigen-specific CD8$^+$ T cells (Extended Data Fig. 12i). Overall, patients with a high abundance of YB328 in gut microbiota have a substantial number of CD103$^+$CD11b$^-$ cDCs, which enable CD8$^+$ T cells to respond to diverse tumour antigens and consequently improving the clinical efficacy of immunotherapies (Extended Data Fig. 12j).

Discussion

One of the difficulties in elucidating the detailed mechanisms by which gut microbiota induce antitumour immunity stems from the complex composition of the microbiota. Restoring and cultivating anaerobic gut microbiota from faecal preservation is technically challenging. Currently, most studies use commercially available bacterial strains, which may limit the clinical relevance of these studies. Here, we successfully isolated a previously undescribed bacterial strain, YB328, from the faeces of patients who responded to PD-1 blockade therapy and revealed the mechanism by which YB328 improves responsiveness to immunotherapy. On the basis of publicly available 16S rRNA gene sequence data, YB328 was estimated to be in the gastrointestinal tract of approximately one-fourth of Japanese individuals. As YB328 abundance ranges from 0.01% to 1%, which indicates that YB328 constitutes a relatively small fraction of microbiota, intervention with YB328 provides a large window to increase its abundance and to improve antitumour immunity (Extended Data Fig. 4b).

The occupation of immunodominant antigen-specific CD8$^+$ T cells in the TME rapidly exhausts CD8$^+$ T cells, which hampers the antitumour efficacy of ICB therapies in patients[49]. YB328 optimizes the range of tumour antigens that contribute to the antitumour efficacy of PD-1 blockade therapy. YB328-stimulated cDCs provided enhanced T cell stimulation signalling to reduce the threshold required for CD8$^+$ T cell antigen recognition. Consequently, PD-1$^+$CD8$^+$ T cell clones with diverse TCRs against both immunodominant and subdominant tumour antigens were primed and activated, which resulted in a favourable PD-1 blockade treatment outcome (Extended Data Fig. 12j and Supplementary Discussion).

Our findings, together with previous reports[2,50–52], suggest that gut microbiota diversity can serve as a pan-ethnic predictive biomarker for response to PD-1 blockade therapy across different cancer types. One can then envision a plausible explanation for the association between high diversity of the gut microbiota and clinical responses to ICB[53]. That is, bacteria that are beneficial for antitumour immunity, such as YB328, first induce CD103$^+$CD11b$^-$ cDC differentiation and activation and further sensitize these cDCs to TLR ligands. We propose a two-step activation system that involves YB328 for CD103$^+$CD11b$^-$ cDC progenies in the gut to activate CD8$^+$ T cells in the TME, namely, primary direct activation and secondary activation induced by other bacteria (Extended Data Fig. 12j,k).

In summary, we demonstrated that a new bacterial strain, YB328, stimulates DCs in GALTs to augment antitumour immunity in the TME. We also presented the mechanism of spatiotemporal regulation of DCs by the microbiome from GALTs to the distant TME for the priming and activation of tumour antigen-specific CD8$^+$ T cells.

Online content

Any methods, additional references, Nature Portfolio reporting summaries, source data, extended data, supplementary information, acknowledgements, peer review information; details of author contributions and competing interests; and statements of data and code availability are available at https://doi.org/10.1038/s41586-025-09249-8.

1. Routy, B. et al. Gut microbiome influences efficacy of PD-1-based immunotherapy against epithelial tumors. *Science* **359**, 91–97 (2018).
2. Gopalakrishnan, V. et al. Gut microbiome modulates response to anti-PD-1 immunotherapy in melanoma patients. *Science* **359**, 97–103 (2018).
3. Matson, V. et al. The commensal microbiome is associated with anti-PD-1 efficacy in metastatic melanoma patients. *Science* **359**, 104–108 (2018).
4. Sivan, A. et al. Commensal *Bifidobacterium* promotes antitumor immunity and facilitates anti-PD-L1 efficacy. *Science* **350**, 1084–1089 (2015).
5. Vetizou, M. et al. Anticancer immunotherapy by CTLA-4 blockade relies on the gut microbiota. *Science* **350**, 1079–1084 (2015).
6. Lee, K. A. et al. Cross-cohort gut microbiome associations with immune checkpoint inhibitor response in advanced melanoma. *Nat. Med.* **28**, 535–544 (2022).
7. Ribas, A. & Wolchok, J. D. Cancer immunotherapy using checkpoint blockade. *Science* **359**, 1350–1355 (2018).
8. Robert, C. et al. Seven-year follow-up of the phase III KEYNOTE-006 study: pembrolizumab versus ipilimumab in advanced melanoma. *J. Clin. Oncol.* **41**, 3998–4003 (2023).
9. Robert, C. et al. Pembrolizumab versus ipilimumab in advanced melanoma (KEYNOTE-006): post-hoc 5-year results from an open-label, multicentre, randomised, controlled, phase 3 study. *Lancet Oncol.* **20**, 1239–1251 (2019).

10. Larkin, J. et al. Five-year survival with combined nivolumab and ipilimumab in advanced melanoma. *N. Engl. J. Med.* **381**, 1535–1546 (2019).
11. Reck, M. et al. Five-year outcomes with pembrolizumab versus chemotherapy for metastatic non-small-cell lung cancer with PD-L1 tumor proportion score ≧ 50. *J. Clin. Oncol.* **39**, 2339–2349 (2021).
12. Kumagai, S. et al. The PD-1 expression balance between effector and regulatory T cells predicts the clinical efficacy of PD-1 blockade therapies. *Nat. Immunol.* **21**, 1346–1358 (2020).
13. Oestreich, K. J., Yoon, H., Ahmed, R. & Boss, J. M. NFATc1 regulates PD-1 expression upon T cell activation. *J. Immunol.* **181**, 4832–4839 (2008).
14. Agata, Y. et al. Expression of the PD-1 antigen on the surface of stimulated mouse T and B lymphocytes. *Int. Immunol.* **8**, 765–772 (1996).
15. Lam, K. C. et al. Microbiota triggers STING-type I IFN-dependent monocyte reprogramming of the tumor microenvironment. *Cell* **184**, 5338–5356 (2021).
16. Fluckiger, A. et al. Cross-reactivity between tumor MHC class I-restricted antigens and an enterococcal bacteriophage. *Science* **369**, 936–942 (2020).
17. Bessell, C. A. et al. Commensal bacteria stimulate antitumor responses via T cell cross-reactivity. *JCI Insight* **5**, e135597 (2020).
18. Griffin, M. E. et al. *Enterococcus* peptidoglycan remodeling promotes checkpoint inhibitor cancer immunotherapy. *Science* **373**, 1040–1046 (2021).
19. Hezaveh, K. et al. Tryptophan-derived microbial metabolites activate the aryl hydrocarbon receptor in tumor-associated macrophages to suppress anti-tumor immunity. *Immunity* **55**, 324–340 (2022).
20. Singh, N. et al. Activation of Gpr109a, receptor for niacin and the commensal metabolite butyrate, suppresses colonic inflammation and carcinogenesis. *Immunity* **40**, 128–139 (2014).
21. Kim, O. Y. et al. Bacterial outer membrane vesicles suppress tumor by interferon-γ-mediated antitumor response. *Nat. Commun.* **8**, 626 (2017).
22. Mager, L. F. et al. Microbiome-derived inosine modulates response to checkpoint inhibitor immunotherapy. *Science* **369**, 1481–1489 (2020).
23. Tanoue, T. et al. A defined commensal consortium elicits CD8 T cells and anti-cancer immunity. *Nature* **565**, 600–605 (2019).
24. Gutierrez-Martinez, E. et al. Cross-presentation of cell-associated antigens by MHC class I in dendritic cell subsets. *Front. Immunol.* **6**, 363 (2015).
25. Cabeza-Cabrerizo, M., Cardoso, A., Minutti, C. M., da Costa, M. P. & Sousa, C. R. E. Dendritic cells revisited. *Annu. Rev. Immunol.* **39**, 131–166 (2021).
26. Gros, A. et al. PD-1 identifies the patient-specific $CD8^+$ tumor-reactive repertoire infiltrating human tumors. *J. Clin. Invest.* **124**, 2246–2259 (2014).
27. Kansy, B. A. et al. PD-1 status in $CD8^+$ T cells associates with survival and anti-PD-1 therapeutic outcomes in head and neck cancer. *Cancer Res.* **77**, 6353–6364 (2017).
28. Thommen, D. S. et al. A transcriptionally and functionally distinct PD-1^+ $CD8^+$ T cell pool with predictive potential in non-small-cell lung cancer treated with PD-1 blockade. *Nat. Med.* **24**, 994–1004 (2018).
29. Wherry, E. J. & Kurachi, M. Molecular and cellular insights into T cell exhaustion. *Nat. Rev. Immunol.* **15**, 486–499 (2015).
30. Afrizal, A. et al. Anaerobic single-cell dispensing facilitates the cultivation of human gut bacteria. *Environ. Microbiol.* **24**, 3861–3881 (2022).
31. Wexler, A. G. & Goodman, A. L. An insider's perspective: *Bacteroides* as a window into the microbiome. *Nat. Microbiol.* **2**, 17026 (2017).
32. Zehn, D., Lee, S. Y. & Bevan, M. J. Complete but curtailed T-cell response to very low-affinity antigen. *Nature* **458**, 211–214 (2009).
33. Spranger, S., Dai, D., Horton, B. & Gajewski, T. F. Tumor-residing Batf3 dendritic cells are required for effector T cell trafficking and adoptive T cell therapy. *Cancer Cell* **31**, 711–723 (2017).
34. Grajales-Reyes, G. E. et al. Batf3 maintains autoactivation of Irf8 for commitment of a $CD8\alpha^+$ conventional DC clonogenic progenitor. *Nat. Immunol.* **16**, 708–717 (2015).
35. Suzuki, S. et al. Critical roles of interferon regulatory factor 4 in $CD11b^{high}CD8\alpha^-$ dendritic cell development. *Proc. Natl Acad. Sci. USA* **101**, 8981–8986 (2004).
36. Bogunovic, M. et al. Origin of the lamina propria dendritic cell network. *Immunity* **31**, 513–525 (2009).
37. Murphy, T. L. et al. Transcriptional control of dendritic cell development. *Annu. Rev. Immunol.* **34**, 93–119 (2016).
38. Sathaliyawala, T. et al. Mammalian target of rapamycin controls dendritic cell development downstream of Flt3 ligand signaling. *Immunity* **33**, 597–606 (2010).
39. Laouar, Y., Welte, T., Fu, X. Y. & Flavell, R. A. STAT3 is required for Flt3L-dependent dendritic cell differentiation. *Immunity* **19**, 903–912 (2003).
40. Vrzalikova, K. et al. S1PR1 drives a feedforward signalling loop to regulate BATF3 and the transcriptional programme of Hodgkin lymphoma cells. *Leukemia* **32**, 214–223 (2018).
41. Lollies, A. et al. An oncogenic axis of STAT-mediated BATF3 upregulation causing MYC activity in classical Hodgkin lymphoma and anaplastic large cell lymphoma. *Leukemia* **32**, 92–101 (2018).
42. Edelson, B. T. et al. Peripheral $CD103^+$ dendritic cells form a unified subset developmentally related to $CD8\alpha^+$ conventional dendritic cells. *J. Exp. Med.* **207**, 823–836 (2010).
43. Kawai, T. & Akira, S. Signaling to NF-κB by toll-like receptors. *Trends Mol. Med.* **13**, 460–469 (2007).
44. Kugelberg, E. Innate immunity: making mice more human the TLR8 way. *Nat. Rev. Immunol.* **14**, 6 (2014).
45. Jang, M. H. et al. CCR7 is critically important for migration of dendritic cells in intestinal lamina propria to mesenteric lymph nodes. *J. Immunol.* **176**, 803–810 (2006).
46. Liu, J., Zhang, X., Cheng, Y. & Cao, X. Dendritic cell migration in inflammation and immunity. *Cell. Mol. Immunol.* **18**, 2461–2471 (2021).
47. Hashimoto, T. et al. The SCRUM-MONSTAR cancer-omics ecosystem: striving for a quantum leap in precision medicine. *Cancer Discov.* **14**, 2243–2261 (2024).
48. Routy, B. et al. Fecal microbiota transplantation plus anti-PD-1 immunotherapy in advanced melanoma: a phase I trial. *Nat. Med.* **29**, 2121–2132 (2023).
49. Burger, M. L. et al. Antigen dominance hierarchies shape $TCF1^+$ progenitor CD8 T cell phenotypes in tumors. *Cell* **184**, 4996–5014 (2021).
50. Zitvogel, L., Ma, Y., Raoult, D., Kroemer, G. & Gajewski, T. F. The microbiome in cancer immunotherapy: diagnostic tools and therapeutic strategies. *Science* **359**, 1366–1370 (2018).
51. Peters, B. A. et al. Relating the gut metagenome and metatranscriptome to immunotherapy responses in melanoma patients. *Genome Med.* **11**, 61 (2019).
52. Jin, Y. et al. The diversity of gut microbiome is associated with favorable responses to anti-programmed death 1 immunotherapy in Chinese patients with NSCLC. *J. Thorac. Oncol.* **14**, 1378–1389 (2019).
53. Matson, V., Chervin, C. S. & Gajewski, T. F. Cancer and the microbiome-influence of the commensal microbiota on cancer, immune responses, and immunotherapy. *Gastroenterology* **160**, 600–613 (2021).

Methods

Patients and samples

Patients with advanced NSCLC ($n = 22$) and patients with GC ($n = 49$) who received PD-1 blockade monotherapy (nivolumab or pembrolizumab) from March 2017 to September 2018 were enrolled in this study. Patients were separated into two independent cohorts in this study: the discovery cohort, in which patients with NSCLC or GC received PD-1 blockade monotherapy from March 2017 to December 2017 ($n = 50$; NSCLC, $n = 15$; GC, $n = 35$), and the validation cohort, in which patients with NSCLC or GC received PD-1 blockade monotherapy from January 2018 to September 2018 ($n = 21$; NSCLC, $n = 7$; GC, $n = 14$). Patients with HNSCC ($n = 16$) who received PD-1 blockade monotherapy (nivolumab or pembrolizumab) from June 2022 to October 2023 were also enrolled in this study. Patients with HNSCC who tested positive for human papillomavirus were excluded. In the MONSTAR cohort[47], patients who received PD-1 blockade monotherapy (nivolumab or pembrolizumab) were enrolled from July 2019 to February 2022. Cancer types with $n > 15$ patients (advanced MM ($n = 16$), renal cell carcinoma ($n = 44$), GC ($n = 32$) and oesophageal cancer ($n = 29$)) were analysed in this study. Patients who were treated with antibiotics or microbiome intervention therapy within 1 month (the NSCLC and GC cohort and the HNSCC cohort) or 3 months (MONSTAR cohort) before the initiation of treatment were excluded from this study. Patients who achieved a complete or partial response or stable disease lasting >6 months were classified as responders and those who progressed on therapy or had stable disease <6 months were classified as non-responders per the Response Evaluation Criteria in Solid Tumors (RECIST; v.1.1). Forty-seven patients (discovery cohort: NSCLC, $n = 4$ and GC, $n = 22$; validation cohort: NSCLC, $n = 7$ and GC, $n = 14$) had an available quantity of TIL isolated; these samples were subjected to multiple immunological analyses. Stool samples were collected within 1 week before initial treatment with a DNA stabilizer (FS-0009, TechnoSuruga Laboratory) according to the manufacturer's instructions and then stored at −80 °C. Fresh tumour samples were obtained from primary or metastatic tumours by needle or endoscopic biopsy within 2 weeks before initial administration and subjected to immunological analyses. Clinical information of patients was obtained from their medical records.

PD-L1 immunohistochemistry

Anti-PD-L1 monoclonal antibody (22C3, Dako; SP142 or SP263, Roche) was used for immunohistochemistry (IHC) with an automatic staining instrument (BenchMark ULTRA, Roche) as previously described[54]. PD-L1 positivity was defined as staining in 1% or more of the tumour cells.

Evaluation of mismatch repair status

Anti-mutL homologue 1 (MLH1; ES05) monoclonal antibody, anti-mutS homologue 2 monoclonal antibody (MSH2; FE11), anti-postmeiotic segregation increased 2 monoclonal antibody (PMS2; EP51) and anti-mutS homologue 6 monoclonal antibody (MSH6; EP49) (all from Dako) were used for IHC. Tumours were considered negative for MLH1, MSH2, PMS2 or MSH6 expression if there was a complete absence of nuclear staining in tumour cells. Normal epithelial cells and lymphocytes were used as internal controls. Tumours lacking MLH1, MSH2, PMS2 or MSH6 expression were considered deficient in mismatch repair, whereas tumours that expressed all these markers were considered proficient in mismatch repair.

Evaluation of Epstein–Barr virus status

Chromogenic in situ hybridization for RNA encoding Epstein–Barr virus was performed with fluorescein-labelled oligonucleotide probes (INFORM EBER probe) with enzymatic digestion (ISH protease 3, Roche) and an iViewBlue detection kit (Roche) with the BenchMark ULTRA staining system.

Analysis of human TILs

Tumour tissues were minced and treated within 72 h after surgery according to a TIL preparation protocol using an optimized tissue preservation reagent (Tumor & Tissue Preservation Reagent (TTPR)) and a TIL isolation reagent (Tumor & Tissue Dissociation Reagent (TTDR)), which were codeveloped by BD Biosciences[55]. Alternatively, tumour tissues were treated immediately with a gentleMACS Dissociator (Miltenyi Biotec) as previously described[56]. These samples were analysed using a BD LSRFortessa X-20 (BD Biosciences) or a FACSymphony system (BD Biosciences).

Flow cytometry analysis

Cells were washed with PBS containing 2% FCS and stained with the indicated antibodies and fixable viability dye. After staining for cell surface markers, the cells were intracellularly stained with antibodies with a FOXP3 staining buffer set (Thermo Fisher Scientific) according to the manufacturer's instructions. After washing, cells were analysed with a BD LSRFortessa X-20 (BD Biosciences) or a FACSymphony system (BD Biosciences). The data were analysed with FlowJo software (v.10.8.1; BD Biosciences). The staining antibodies were diluted according to the manufacturer's instructions. To analyse the similarity of the $CD8^+$ TCR Vβ repertoires, the expression of TCR Vβ was evaluated and presented as an ordination plot by uniform manifold approximation and projection. To analyse the diversity of TLR expression on DCs, the Shannon index of TLR expression was calculated based on the expression of TLR1–TLR9.

DNA extraction from faecal samples

Total DNA extraction was conducted using a QIAamp DNA Stool Mini kit (Qiagen) according to the manufacturer's instructions. To increase the recovery of bacterial DNA, particularly from Gram-positive bacteria, pretreatment with lytic enzymes was performed before extraction using a stool kit. In brief, 100 mg faecal sample was suspended in 10 ml Tris-EDTA buffer (pH 7.5), and then 50 µl of 100 mg ml^{-1} lysozyme type VI purified from chicken egg white (MP Biomedicals) and 50 µl of 1 mg ml^{-1} purified achromopeptidase (Fujifilm Wako Pure Chemical) were added. The solution was incubated at 37 °C for 1 h with mixing. Next, 0.12 g SDS (final concentration of 1%) was added, and the suspension was mixed until it became clear. Next, 100 µl of 20 mg ml^{-1} proteinase K (Fujifilm Wako Pure Chemical) was added, followed by incubation at 55 °C for 1 h with mixing. The cell lysate was then subjected to ethanol precipitation. The precipitate was dissolved in 1.6 ml ASL buffer from the stool kit and subsequently purified using a QIAamp DNA Stool Mini kit (Qiagen). For the HNSCC cohort, DNA was extracted using an ISOSPIN Fecal DNA kit (Nippon Gene) following protocol N as previously described[57].

16S rRNA gene sequencing

Each library was prepared according to the 'Illumina 16S Metagenomic Sequencing Library Preparation Guide' with a primer set (27Fmod: 5′-AGR GTT TGA TCM TGG CTC AG-3′ and 338R: 5′-TGC TGC CTC CCG TAG GAG T-3′) targeting the V1–V2 region of the 16S rRNA gene. Next, 251-bp paired-end sequencing of the amplicon was performed using MiSeq (Illumina) with a MiSeq v.2 500 cycle kit. The raw sequences were demultiplexed and quality-trimmed with a FASTX-Toolkit (http://hannonlab.cshl.edu/fastx_toolkit/index.html, v.0.0.14) and BBtrim (http://bbmap.sourceforge.net, v.33.21). A total of 20,000 reads per sample were randomly selected using seqtk (v.1.3-r106) for further analyses. The processed sequences were clustered into operational taxonomic units (OTUs) defined at a 97% similarity cut-off using UCLUST (v.1.2.22q). Representative sequences for each OTU were then classified taxonomically by using RDP Classifier (v.2.2) with the Greengenes (v.13 8) database. The bioinformatics pipeline QIIME (v.1.9.1) was used as the informatics environment for all relevant processing of raw sequencing data and the determination of relative

bacterial abundances. For the HNSCC cohort, sequencing libraries of the V4 hypervariable region of the 16S rRNA gene were prepared as previously described[58] and sequenced on an Illumina MiSeq instrument with V2 chemistry (2 × 251 bp reads).

Bacterial diversity analysis

Alpha diversity was estimated using the Shannon index, which captures both microbiota richness and evenness, after subsampling to an even depth (10,000 reads per sample). Beta diversity was assessed by unweighted UniFrac distance matrices and visualized by PCoA. The PCoA of unweighted UniFrac distances was performed with QIIME, and the results were plotted using R (v.4.02). ANOSIM was used to evaluate the significant differences between groups.

LEfSe

Kruskal–Wallis and pairwise Wilcoxon tests were performed, followed by LDA to assess the effect size of each differentially abundant taxon[59]. Bacteria with markedly increased abundance were defined as those with a $\log_{10}$[LDA score] > 3.

Estimation of YB328 phylotype abundance

Phylotype analysis, as delineated on the basis of the YB328 amplicon sequence variant (ASV) using 16S rRNA gene amplicon sequencing data, was performed for the following datasets: (1) prospective cohort of patients with HNSCC (V4 region, sequencing performed in this study); (2) MONSTAR cohort (V3V4 region, sequencing data obtained with permission from the MONSTAR alliance); and (3) two publicly available sequencing datasets[48,60] (both V3V4 region). For ref. 60, data captured two healthy Japanese cohorts, namely the MORINAGA cohort (n = 704 for study accession DRP005906) and the NIBIOHN cohort (n = 1,280 for study accessions DRP007219, DRP007221, DRP007218, DRP007222 and DRP007220); the data were downloaded from the DDBJ Sequence Read Archive (DRA) in fastq format. For ref. 48, sequence data were obtained from the NCBI Sequence Read Archive (SRA) under BioProject PRJNA928744. In all cases, sequencing reads were denoised to obtain ASVs using DADA2 (v.1.26.0)[61]. For this purpose, primers in the reads were trimmed using Cutadapt (v.4.2)[62], and read pairs without identifiable primers and undetermined bases (Ns) were discarded. Reads were then further trimmed by length (truncLen option) and filtered on the basis of their expected error (maxEE option) using the filterAndTrim function of DADA2. For the publicly available sequencing data, forward and reverse reads were denoised on a per-sample basis using the dada function in DADA2 with the options err = NULL and selfConsist = TRUE. For the data generated in this study (that is, the prospective cohort of patients with HNSCC) and the MONSTAR cohort data, error models for the forward and reverse reads were generated using the learnErrors function in DADA2 on a per-sequencing run basis. After denoising using the dada function with the run-specific error models, ASV tables were merged using mergeSequenceTables function in DADA2 and chimeras were removed using the removeBimeraDenovo function with method = "consensus". For all datasets, a single ASV that perfectly matched the 16S rRNA gene sequence of YB328 was retained and used to calculate the relative abundance of YB328 (phylotype). To verify the specificity of detection of YB328, the V4 and V3V4 ASVs of YB328, as extracted from its whole-genome sequence, were compared against the Greengenes2 database (release 2024.09; Supplementary Data 1).

Metagenomic sequencing

The shotgun sequencing library for each microbial sample was constructed using Illumina DNA Prep (Illumina). The Illumina library was converted to a library for DNBSEQ using an MGIEasy Universal Library Conversion kit (App-A, MGI). Sequencing was performed on a DNBSEQ-G400RS (MGI) in 150-bp paired-end mode. All procedures were performed according to the manufacturer's instructions.

Whole-genome sequencing of bacteria

The genomic DNA of YB328 and *P. vulgatus* AE61 was extracted using an enzymatic lysis method with Qiagen Genomic-tip 100/G columns according to the manufacturer's protocol. The complete genome sequence of strain YB328 and a high-quality draft genome of *P. vulgatus* AE61 were determined using PacBio HiFi (high-fidelity) reads (Supplementary Table 7). PacBio sequencing, including library preparation and library quality control, were performed by Bioengineering Lab. In brief, short DNA fragments were removed using a Short Read Eliminator kit (PacBio) and retained DNA was sheared using a Covaris instrument to a size of 10–20 kbp. Sequencing libraries were then prepared using a PacBio SMRTbell Prep kit 3.0 and a SMRTbell gDNA Sample Amplification kit and quantified using a QuantiFluor dsDNA system (Promega) and an Agilent HS Genomic DNA 50 kb kit (Agilent Technologies) for quantification and size distribution, respectively. The library was then treated with a Revio Polymerase kit (PacBio) and sequenced on a Revio instrument. HiFi reads (Q20) were generated using SMRT Link (v.13.0.0.207600) to remove overhang adapter sequences and to create consensus sequences based on the resultant subreads. Lima (v.2.9.0) and pbmarkdup (v.1.0.3) were used for removing ultra-low PCR adapter sequences and PCR duplex reads, respectively. The resulting reads were assembled using Flye (v.2.9.5) and specifying the parameters --genome-size 3 m --asm-coverage 40. A phylogenetic tree showing the phylogenetic placement of YB328 and related taxa was constructed based on 120 single-copy marker genes using GTDB-Tk (v.2.4.0) with GTDB release 220 reference data. Protein sequences of identified marker genes (using the identify function of GTDBTk) were aligned using the align function of GTDBTk with the option skip_trimming. Aligned protein sequences were then loaded into an ARB (v.7.0) database, representative genomes were selected and the data were exported with custom masks for uninformative sites. Approximate maximum-likelihood phylogenetic trees were inferred using FastTree (v.2.1.1053), and the trees were visualized in ARB. The average nucleotide identity (ANI) values were then calculated using fastANI[63] through comparisons of YB328 and closely related species. Genome gene identification was performed with Prodigal (v.2.6.3) with the default settings[64]. The predicted protein sequences were further analysed by matching against the Clusters of Orthologous Groups (COGs) database (release 3.10 in the Conserved Domain Database)[65] using RPS-Blast (BLAST v.2.9.0+; E value cut-off of 0.01), the Kyoto Encyclopedia of Genes and Genomes (KEGG) database (release 2019-11-18)[66] and the Virulence Factor Database (VFDB; release 2022.04)[67] and by protein alignment using DIAMOND (v.2.0.13)[68]. Coding sequences unique to strain YB328 (see Extended Data Fig. 4a for genome accessions) were identified using CompareM (v.0.1.2; https://github.com/dparks1134/CompareM) with default settings.

Quantification of species abundances based on metagenome sequencing data

Taxonomic profiling using metagenome sequencing data was performed through read-level taxonomic assignment with Kraken2 (v.2.1.3)[69], followed by estimation of relative abundances using Bracken (v.2.9)[70]. For this purpose, paired-end reads were processed using fastp (v.0.23.2 or v.0.24.0)[71] with the following settings: --trim_tail1 1 --trim_tail2 1 --cut_right --cut_right_window_size 4 --cut_right_mean_quality 15 --qualified_quality_phred 15 --unqualified_percent_limit 40 --trim_poly_x --poly_x_min_len 10 --n_base_limit 0 --length_required 75. Reads were then filtered using NCBI's BMTagger (v.3.101) to remove reads derived from the human genomic DNA. Taxonomic assignment of the reads was performed using Kraken2 against a customized version of the GTDB (v.220), with options --confidence 0.30 --use-names --paired. Species abundances were then estimated based on the Kraken2 output using Bracken, with options -r 150 -t 10.

To construct the custom GTDB-based database, we built Kraken2 and Bracken databases using all species-representative genomes in the GTDB (v.220; n = 113,104 total bacterial and archaeal genomes), after replacing the corresponding genomes of the species *P. vulgatus* (representative: GCF_000012825.1) and *H. mulieris* (representative: GCF_020687165.1) by the two genome sequences generated in this study. Furthermore, to reduce the potential of false-positive assignments, a representative human genome sequence (GRCh38) was also included in the database. Construction of the Kraken2 and Bracken databases largely followed the scheme implemented in Struo2 (ref. 72), with a default k-mer length of 35 and specifying a read length of 150 for the bracken-build command.

To investigate the abundance of YB328 on a global scale, we analysed 1,188 human faecal metagenomic datasets from NCBI's SRA. In this study, we focused on samples from healthy individuals; these were identified on the basis of the metadata available in GMrepo2 (ref. 73) and HumGut[74] by retaining entries marked as 'D006262' and 'Healthy' for GMrepo2 and HumGut, respectively. Data were retrieved in FASTQ format using the SRA Toolkit's prefetch and fasterq-dump commands, and then uniformly processed and analysed using fastp and Kraken2 as described above for the in-house generated sequencing data.

Bacterial identification and culture

All bacterial strains were isolated from fresh human faecal samples. The collected faecal samples were transported under 100% CO_2 using a deoxygenating agent (Mitsubishi Gas Chemical) to a vinyl anaerobic chamber (COY) with an atmosphere composed of N_2, H_2 and CO_2 (8:1:1). The faecal samples were diluted with pre-reduced dilution buffer to 1.0×10^{-8} g ml^{-1} in a tenfold dilution series. Fifty microlitres of 1.0×10^{-6} g ml^{-1}, 1.0×10^{-7} g ml^{-1} and 1.0×10^{-8} g ml^{-1} diluted faecal fluid was inoculated on Eggerth–Gagnon (EG) agar plates[75] supplemented with 5% (v/v) horse blood and M98-5 agar plates[76]. After incubation for 48 h at 37 °C, every colony grown on the plates was picked and subcultured on new plates for purification and growth. The obtained strains were preserved in pre-reduced nutrient broth (BD Biosciences) supplemented with 10% glycerol at −80 °C, and a portion of the colony was used for bacterial taxon identification. For bacterial taxon identification, the 16S rRNA gene sequence of the strains was amplified using the universal primers 27F (5′-AGAGTTTGATCCTGGCTCAG-3′) and 1492R (5′-GGTTACCTTGTTACGACTT-3′), and almost-full-length 16S rRNA genes were sequenced with the universal primers using a previously described procedure[77]. The species of the strains were determined by NCBI BLAST searches if the similarity between the query and the results exceeded 99%. *Bacteroides vulgatus* AE61 (renamed *P. vulgatus*), *Sellimonas intestinalis* AE3, *Clostridium colicanis* AE66, *Eggerthella lenta* AE7, *Ruminococcus torques* AE30 and YB328 were isolated from EG agar plates. *Erysipelatoclostridium ramosum* AM28 was isolated using M98-5 agar plates. *Ruminococcus albus* JCM 14654^T was obtained from the Japan Collection of Microorganisms (JCM) (RIKEN). *Acutalibacter muris* DSM 26090^T, *Neglectibacter timonensis* DSM 102082^T and *Clostridium leptum* DSM 753^T were obtained from the German Collection of Microorganisms and Cell Cultures. *A. muciniphila* BAA-835^T and *B. longum* BAA-999 were obtained from the American Type Culture Collection (ATCC). The culture method for the commercial bacteria was performed according to the manufacturer's instructions. For inoculation of these bacterial strains into mice, the cells were collected using degassed GAM broth (Nissui) in an anaerobic chamber and were then suspended at a concentration of approximately 1.0×10^9 cells per ml in pre-reduced PBS containing 0.05% (w/v) L-cysteine·HCl·H2O or 15% (w/v) glycerol solution for storage. Until inoculation, the suspended bacterial strains were kept at −80 °C.

Cell culture

The mouse colon cancer cell line MC38 (ENH204, Kerafast) and the mammary carcinoma cell line EMT6 (CRL-2755, ATCC) were cultured in high-glucose DMEM (Fujifilm Wako Pure Chemical) supplemented with 10% FBS (Biosera) and 2 mM L-glutamine. Mouse B16F10 (CRL-6475, ATCC) and B16F10-OVA (stable transfectant derived from B16F10 cells, which were generated in house) melanoma cell lines were cultured in RPMI-1640 (Fujifilm Wako Pure Chemical) supplemented with 10% FBS (Biosera) and 2 mM L-glutamine. All cell lines are confirmed to be free of mycoplasma contamination. For the induction of BMDCs from bone marrow (BM), 4×10^6 BM cells were cultured in tissue-culture-treated 6-well plates in 4 ml complete medium (RPMI-1640 (Fujifilm Wako Pure Chemical) supplemented with 2 mM L-glutamine and 10% FBS) containing 20 ng ml^{-1} GM-CSF (Peprotech) as previously described[78]. Half of the medium was removed on day 2, and fresh complete medium containing 40 ng ml^{-1} GM-CSF was added. The culture medium was entirely discarded on day 3 and replaced with complete medium containing 20 ng ml^{-1} GM-CSF. For the bacterial stimulation experiments, the multiplicity of infection (m.o.i.) of bacteria used to infect BMDCs was 100 or indicated in each figure legend. For the TLR stimulation experiment, flagellin (25 ng ml^{-1}, InvivoGen), R848 (25 ng ml^{-1}, Selleck Chemicals) and/or ODN-1826 (250 ng ml^{-1}, InvivoGen) were administered for 24 h in complete medium containing 20 ng ml^{-1} GM-CSF. CDPs were isolated from BM cells by cell sorting and cultured with FLT3L (100 ng ml^{-1}, Peprotech) and IMDM (Merck) supplemented with 2 mM GlutaMax (Merck), 55 μM 2-mercaptoethanol (Merck), 25 mM HEPES (Merck), 1 mM sodium pyruvate (Merck) and 10% FBS. CDPs were identified as LIN$^-$CD117^{int}CD135$^+$CD115$^+$CD11c$^-$MHCII$^-$ BM cells, which lacked the markers of other cell lineages, including CD19, B220, CD3, NK1.1 and TER-119 (refs. 79–81). Bone marrow-derived macrophages were induced from BM cells as previously described[82] and cultured in DMEM containing 10 ng ml^{-1} M-CSF (Peprotech). THP-1-derived reporter cell lines expressing human TLRs (hTLR7, hTLR8 and hTLR9) were cultured according to the manufacturer's instructions (InvivoGen). Cells were stimulated with YB328 for 24 h, and supernatants were collected for downstream analyses. For YB328 fractionation, YB328 was cultured with GAM broth (Nissui) at 37 °C for 16 h. Using the collected cells, the cell membrane fraction and cytoplasm fraction were prepared using the bead-beating method as previously described[83,84]. Using the culture supernatant, the membrane vesicle fraction and supernatant fraction (without membrane vesicles) were prepared by ultracentrifugation previously as described[85,86]. For the stimulation of fractions of YB328, each fraction was added to the culture medium at a concentration of 10% (v/v). The MC38, EMT6 and B16F10 cell lines were pre-authenticated by ATCC using short tandem repeat sequencing. OVA expression in B16F10-OVA cells was confirmed by flow cytometry. THP1-Dual™ hTLR7, THP1-Dual™ hTLR8 and THP1-Dual™ hTLR9 cells were not authenticated but were functionally validated for responsiveness to their respective TLR agonists, serving as positive controls.

Animal models

C57BL/6 mice and BALB/cJ mice (6–10 weeks old) were purchased from CLEA Japan. OT-I TCR transgenic mice[87] (provided by W. R. Heath, University of Melbourne), *Myd88*$^{-/-}$ mice[88], *Tlr7*$^{-/-}$, *Tlr9*$^{-/-}$ and *Tlr7*$^{-/-}$*Tlr9*$^{-/-}$ mice (Oriental Bio Service, provided by S. Akira, WPI Immunology Frontier Research Center, Osaka University), *Batf3*$^{-/-}$ mice[89] (The Jackson Laboratory, provided by K. Murphy, Washington University School of Medicine) and Kikume Green–Red (KikGR) mice[90] (RIKEN BioResource Research Center, provided by M. Tomura, Kyoto University Graduate School of Medicine) were used. GF mice were bred and maintained in the gnotobiotic facilities of the Central Institute for Experimental Animals or purchased from CLEA Japa or Sankyo Labo and maintained within the gnotobiotic facilities of the National Institute of Advanced Industrial Science and Technology. Other mice were housed in cages under SPF conditions, provided with standard food, given free access to hypochlorous weak-acid water and housed with a 12–12-h light–dark cycle with lights on at 8:00. The temperature was maintained at 22 °C (20–26 °C), and the humidity was 45% (40–60%).

In tumour challenge experiments, syngeneic mice were subcutaneously inoculated with 1×10^6 MC38 colon cancer cells, 1×10^6 EMT6 mammary carcinoma cells, 5×10^5 B16F10 melanoma cells or 5×10^5 B16F10-OVA melanoma cells in a total of 100 µl of PBS. The mice were randomized into different groups, ensuring that the tumour size was similar across all groups before the initiation of treatment. Anti-PD-1 monoclonal antibody (200 µg per mouse; clone: RMP1-14; BioLegend), anti-CSF1R monoclonal antibody (100 µg per mouse; clone: AFS98; Bio X Cell) or isotype control antibody (clone RTK2758; BioLegend) was intraperitoneally administered 3 times at 3-day intervals. Tumour length and width were measured on the indicated days, and tumour size was calculated as $V = ½ (\text{tumour length} \times \text{tumour width}^2)$. The immunological profile of the TME was analysed on days 13 or 15 after tumour inoculation. For TLR agonist injection, TLR agonists (0.5 µg flagellin, 5 µg R848 and/or 5 µg per ODN-1826 per mouse) were intraperitoneally administered. Mice were monitored twice a week and euthanized when the subcutaneous tumour diameter exceeded 20 mm. In some FMT and bacterial administration experiments, mice were preconditioned with antibiotics (ampicillin 500 mg l^{-1} (Merck), neomycin 500 mg l^{-1} (Merck), metronidazole 1 g l^{-1} (Merck) and vancomycin 500 mg l^{-1} (Merck)) dissolved in sterile drinking water. Mice received bacterial or faecal transplantation by oral gavage using feeding needles. For FMT, we were able to collect faecal samples sufficient for in vivo animal models after examining gut microbiota from a total of 6 patients—3 responders and 3 non-responders—and used the faecal samples from these patients for each independent experiment. Faecal samples (0.1 g) were dissolved in 10 ml PBS and administered to mice by oral gavage (100 µl per mouse). For the bacterial administration experiments, we prepared the bacterial stock at 10^8 cells per ml and administered it to mice by oral gavage (100 µl per mouse). Intestinal-cell-labelling experiments were performed as previously described[90]. In brief, the small intestine was drawn from the abdominal cavity and photoconverted by exposure to violet light (435 nm, 40–50 mW cm^{-2}) for 90 s by laparotomy. Nontargeted regions were protected from light using aluminium foil. For adoptive transfer experiments, splenocytes were collected from OT-I TCR transgenic mice, and $CD8^+$ T cells were purified with CD8a microbeads (Miltenyi Biotec). SPF mice pretreated with antibiotics were subcutaneously injected with B16F10-OVA cells, and the sorted $CD8^+$ T cells (1×10^6 cells per mouse) were transferred by intravenous injection. No blinding was performed. Sample sizes for animal experiments were chosen according to preliminary pilot studies[12,91,92], and are in line with standards in the field.

Isolation of mouse immune cells

To isolate TILs and lymphocytes from the lymph nodes, tissue samples were collected and minced into small pieces, followed by digestion with BD Horizon Dri TTDR reagent at room temperature for 20 min. After dissociation, the cell suspension was filtered through a 70-µm strainer and washed with PBS supplemented with 1% BSA. For intestinal tissues, small intestines (duodenum, jejunum and ilium) were excised. The intestinal contents were removed by washing with HBSS. Fat tissue was also removed. Peyer's patches and mesenteric tissues were carefully removed and digested in BD Horizon Dri TTDR according to the manufacturer's instructions. The intestines were further opened longitudinally and cut into 5-mm long segments. Tissues were digested using a Lamina Propria Dissociation kit (Miltenyi Biotec) according to the manufacturer's instructions.

ELISAs

BMDCs were stimulated with the indicated bacteria for 12 h, and chemokines and cytokines were measured using ELISA kits according to the manufacturer's instructions (CXCL9, Abcam; CXCL10, Thermo Fisher Scientific; Proteome Profiler Mouse Chemokine Array kit, R&D Systems; and IL12p70, Thermo Fisher Scientific). For profiling chemokine expression with a Proteome Profiler Mouse Chemokine Array kit, the membrane was visualized using an LAS-4000 instrument (GE Healthcare), and the raw imaging data were processed and analysed with ImageJ software (Fiji, v.2.0.0).

Features of YB328

The cell structure of YB328 was observed by scanning electron microscopy (S-4500; Hitachi) and transmission electron microscopy (H-7600; Hitachi) as previously described[93,94]. In brief, for scanning electron microscopy observation, YB328 cells were fixed with 2% glutaraldehyde, post-fixed with 1% osmium tetroxide and dehydrated through a graded ethanol series followed by 3-methylbutyl acetate. For transmission electron microscopy observation, the cells were fixed with 2.5% glutaraldehyde and then post-fixed with 1% osmium tetroxide. The fixed cells were suspended in 1% aqueous uranyl acetate. The biochemical properties of YB328 were evaluated using an API ZYM system (bioMérieux) according to the manufacturer's instructions.

Confocal microscopy

$CD8^+$ T cells from OT-I TCR transgenic mice were prestained with 1 mg ml^{-1} Hoechst 33342 (Dōjindo Laboratories) at 37 °C for 10 min, washed and then cultured with the indicated bacteria-stimulated DCs pulsed with OVA peptides. After 4 h of culture, the cells were collected. Bacteria were prestained with SYTO Green Fluorescent Nucleic Acid stains (Thermo Fisher Scientific) and cultured with BMDCs prestained with CellTracker Deep Red dye (Thermo Fisher Scientific). All staining procedures were performed according to the manufacturer's instructions. After 15 min of culture, the cells were collected. Cells were fixed with 4% formaldehyde solution for 30 min, permeabilized with 0.5% Triton X-100 for 10 min and blocked with PBS supplemented with 10% BSA for 1 h. The fixed cells were stained with an anti-NFATC1 (Thermo Fisher Scientific) monoclonal antibody overnight and then with a DyLight 488 secondary antibody (Thermo Fisher Scientific). All the antibodies were diluted in 10% BSA in PBS. Coverslips were mounted with ProLong Diamond Antifade mountant (Thermo Fisher Scientific). Images were captured by fluorescence microscopy (Carl Zeiss LSM-880, Zeiss) and analysed using ZEN software (Zeiss).

Time-lapse microscopy

The DCs and T cells were prestained with 0.5 µM CellTracker Green CMFDA dye, 0.5 µM CellTracker Red CMTPX dye, 0.5 µM CellTracker Deep Red dye (Thermo Fisher Scientific) or 1 mg ml^{-1} Hoechst 33342 at 37 °C for 10 min. Bacteria were prestained with SYTO Green Fluorescent Nucleic Acid stains (Thermo Fisher Scientific) according to the manufacturer's instructions. Prestained DCs (2×10^5) were mixed with prestained $CD8^+$ T cells from OT-I TCR transgenic mice (1×10^5) or bacteria (m.o.i. = 100) and seeded into a culture dish. The videos were recorded using an A1R MP^+ multiphoton microscope system (Nikon) or a fluorescence microscope (Carl Zeiss LSM-880, Zeiss). The raw imaging data were processed and analysed with ImageJ software (Fiji, v.2.0.0).

IVIS spectrum in vivo imaging

Mice were depilated by hair removal cream 1 week before observation using an IVIS spectrum imaging system (IVIS kinetics, PerkinElmer), and the iVid-neo diet (Oriental Bio) was applied 2 weeks before observation to reduce autofluorescence from the diet. After 4 days of photoconversion, in vivo fluorescence images were obtained (for KikG, excitation filter = 465 nm, emission filter = GFP; for KikR, excitation filter = 570 nm, emission filter = Cy5.5). Analysis was conducted using Living Image software (v.4.7.3, PerkinElmer).

RNA sequencing

Total RNA was extracted from BMDCs using a RNeasy Micro kit (Qiagen) and further processed with a SMART-Seq v4 Ultra Low Input RNA kit (Takara Bio). cDNA library preparation was conducted with a Nextera XT DNA Library Preparation kit (Illumina). The prepared RNA sequencing

libraries were subjected to next-generation sequencing with a NovaSeq 6000 (Illumina) using 150-bp read lengths in paired-end mode. The reads generated for each RNA sample were analysed and compared using the Illumina DRAGEN Bio-IT Platform. Sequencing reads were aligned and annotated to the UCSC mouse reference genome (GRCm38.p6) from Gencode. The number of transcripts per kilobase million was calculated and used for downstream analyses. Expression levels across samples were normalized by *z* score transformation.

Quantitative PCR

To determine the gene expression of BMDCs, total RNA was extracted from BMDCs using a RNeasy Micro kit (Qiagen). cDNA synthesis was performed with SuperScript IV VILO master mix (Thermo Fisher Scientific). The TaqMan gene assay probe was purchased from Thermo Fisher Scientific (assay ID: Batf3/Mm01318273_m1; 18S rRNA/Hs03003631_g1). TaqMan Fast Advanced master mix (Thermo Fisher Scientific) was used to perform PCR, and the results were examined with a QuantStudio 7 Flex Real-Time PCR system (Thermo Fisher Scientific). The PCR conditions were as follows: 50 °C for 2 min, 95 °C for 20 s, and 40 cycles of 95 °C for 3 s and 60 °C for 30 s. Gene expression was normalized to that of the endogenous control gene 18S rRNA. Relative gene expression between groups was determined using the comparative threshold cycle method. YB328 and *P. vulgatus* were quantified in faeces and tumour tissues by real-time PCR with a primer set targeting the *recA* gene of YB328 (forward primer: 5′-CCTCTTGGACCTTGCCGAAA-3′; reverse primer: 5′-ATACGCGTGCCGTTATACGA-3′) and the 16S rRNA gene of *P. vulgatus* (5′-forward primer: CGGGCTTAAATTGCAGATGA; reverse primer: 5′-CATGCAGCACCTTCACAGAT-3′) as previously described[95] using a QuantStudio 5 Real-Time PCR instrument. The reactions (20 µl) contained 1 × Power SYBR Green PCR master mix and 500 nM each of the forward and reverse primers, and the thermal cycling conditions were as follows: 95 °C for 1 min, 40 cycles of 95 °C for 30 s, 55 °C for 30 s, and 72 °C for 15 s. A standard curve was prepared using purified genomic DNA of YB328 and *P. vulgatus*.

Multiplex IHC staining

Formalin-fixed and paraffin-embedded blocks of tumour specimens were sliced into 4-µm-thick sections on adhesion microscope slides (Matsunami). The tissue slides were deparaffinized and rehydrated for multiplex IHC staining. Antigen retrieval and subsequent staining were performed using an Opal 7-Colour IHC kit (Akoya Biosciences) according to the manufacturer's instructions.

Statistical analysis

Statistical analyses were performed with Prism software (v.8; GraphPad), SPSS (v.21.0; IBM) and R (v.4.02; R Foundation for Statistical Computing). Patient characteristics were compared between the two groups using Pearson's chi-square test and Fisher's exact test. ROC curves for continuous variables were created by plotting the true-positive rate against the false-positive rate at each threshold. The AUC shown in each plot summarizes the performance of continuous variables. The cut-off values of continuous variables were determined as the maximum sum of the sensitivity and specificity in ROC analyses. Survival curves were estimated using the Kaplan–Meier method and compared using the log-rank test. No statistical methods were used to predetermine sample size. Data were analysed for a normal distribution using the Shapiro-Wilk test before comparisons. The relationships between two groups were compared using a two-sided Student's *t*-test for normally distributed data or the nonparametric Mann–Whitney *U*-test. For multiple testing, significance was determined by one-way ANOVA followed by Bonferroni's correction. Tumour volume curves were compared using two-way ANOVA with the Tukey–Kramer method. The correlation coefficient was evaluated by Pearson's correlation. Univariate or multivariate analyses were performed with the Cox regression model. All graphs of animal and in vitro experiments show representative data from at least two independent experiments. $P < 0.05$ was considered to indicate significance. NS, not significant.

Inclusion and ethics

This study was conducted in Japan with the involvement of local researchers throughout the research process, from conceptualization to data analyses and manuscript preparation. All patients provided written informed consent before sampling, according to the Declaration of Helsinki. Analyses of cohort samples were conducted in a blinded manner and approved by the National Cancer Center Ethics Committee (IRB protocol numbers: GC and NSCLC cohort: 2015-048 and 2017-007; HNSCC cohort: 2022-346; MONSTAR cohort: 2018-367). The GC and NSCLC cohort and the MONSTAR cohort are registered in the UMIN Clinical Trials Registry (https://www.umin.ac.jp/ctr/, IDs: UMIN000019129 and UMIN000036749, respectively). The study was not designed to evaluate outcomes based on participant characteristics such as sex or ethnicity. Animal care and experiments were conducted according to the guidelines of the animal committee of the National Cancer Center/Institutional Animal Experiment Committee of National Institute of Advanced Industrial Science and Technology after approval by the Ethics Review Committee for Animal Experimentation of the National Cancer Center (protocol numbers: K24-007 and K24-010) and the Institutional Animal Experiment Committee of National Institute of Advanced Industrial Science and Technology (protocol number: 2022-0413).

Reporting summary

Further information on research design is available in the Nature Portfolio Reporting Summary linked to this article.

Data availability

The whole genome sequences of YB328 and *P. vulgatus* AE61 have been deposited in the NCBI BioProject under accession PRJDB17635. The 16S rRNA gene sequences of the bacterial strains isolated in this study have been deposited in DDBJ, EMBL and GenBank under the accession numbers LC719261 and LC744884–LC744889, corresponding to strain YB328, *P. vulgatus* strain AE61, *S. intestinalis* strain AE3, *C. colicanis* strain AE66, *E. lenta* strain AE7, *R. torques* strain AE30 and *E. ramosum* strain AM28. The metagenome and 16S rRNA gene amplicon sequencing data generated in this study are available under BioProject accession PRJDB17628. The datasets used in this study, including the HNSCC cohort and the MONSTAR cohort, are not publicly available because of their association with unpublished studies. Access to these datasets is therefore restricted in accordance with institutional policies and data protection requirements. Researchers interested in accessing these data may submit a formal request to the corresponding author H.N. The datasets for the Healthy Japanese cohort (the data have been deposited in DNA Databank of Japan (DDBJ) under accession numbers DRP005906, DRP007219, DRP007221, DRP007218, DRP007222 and DRP007220), the MM cohort (BioProject PRJNA928744)[48] and the faecal metagenomics analysis of global abundance of YB328 in healthy donors (BioProjects PRJEB6456, PRJEB21528, PRJNA422434, PRJNA397112, PRJDB4176, PRJNA517801, PRJNA529400, PRJEB27005, PRJNA529124, PRJEB8094, PRJEB17896, PRJNA328899, PRJEB7369, PRJEB6092, PRJNA268964, PRJNA447983, PRJEB1220, PRJEB1690, PRJNA289586, PRJNA421881, PRJEB17784, PRJEB5224, PRJNA504891, PRJEB9576, PRJEB6070, PRJNA438847, PRJEB27928, PRJEB12357 and PRJEB1786) were downloaded through the SRA. The RNA sequences of bacteria-stimulated BMDCs are available from the Gene Expression Omnibus under accession number GSE285376. The predicted protein sequences were analysed by matching against the COGs database (release 3.10 in the Conserved Domain Database, https://www.ncbi.nlm.nih.gov/research/cog-project/)[65], the KEGG database (release 2019-11-18, https://www.kegg.jp/kegg/download/)[66] and the VFDB

database (release 2022.04, https://www.mgc.ac.cn/VFs/download.htm)[67]. Source data are provided with this paper.

Code availability

No custom code was developed in this study.

54. Tada, Y. et al. Targeting VEGFR2 with ramucirumab strongly impacts effector/activated regulatory T cells and CD8$^+$ T cells in the tumor microenvironment. *J. Immunother. Cancer* **6**, 106 (2018).
55. Kobayashi, T. et al. Isolation of tumor-infiltrating lymphocytes from preserved human tumor tissue specimens for downstream characterization. *STAR Protoc.* **3**, 101557 (2022).
56. Saito, T. et al. Two FOXP3$^+$CD4$^+$ T cell subpopulations distinctly control the prognosis of colorectal cancers. *Nat. Med.* **22**, 679–684 (2016).
57. Tourlousse, D. M. et al. Validation and standardization of DNA extraction and library construction methods for metagenomics-based human fecal microbiome measurements. *Microbiome* **9**, 95 (2021).
58. Tourlousse, D. M. et al. Characterization and demonstration of mock communities as control reagents for accurate human microbiome community measurements. *Microbiol. Spectr.* **10**, e0191521 (2022).
59. Segata, N. et al. Metagenomic biomarker discovery and explanation. *Genome Biol.* **12**, R60 (2011).
60. Park, J. et al. Comprehensive analysis of gut microbiota of a healthy population and covariates affecting microbial variation in two large Japanese cohorts. *BMC Microbiol.* **21**, 151 (2021).
61. Callahan, B. J. et al. DADA2: high-resolution sample inference from Illumina amplicon data. *Nat. Methods* **13**, 581–583 (2016).
62. Martin, M. Cutadapt removes adapter sequences from high-throughput sequencing reads. *EMBnet J.* **17**, 10 (2011).
63. Jain, C., Rodriguez, R. L., Phillippy, A. M., Konstantinidis, K. T. & Aluru, S. High throughput ANI analysis of 90 K prokaryotic genomes reveals clear species boundaries. *Nat. Commun.* **9**, 5114 (2018).
64. Seemann, T. Prokka: rapid prokaryotic genome annotation. *Bioinformatics* **30**, 2068–2069 (2014).
65. Galperin, M. Y. et al. COG database update: focus on microbial diversity, model organisms, and widespread pathogens. *Nucleic Acids Res.* **49**, D274–D281 (2021).
66. Kanehisa, M., Furumichi, M., Sato, Y., Ishiguro-Watanabe, M. & Tanabe, M. KEGG: integrating viruses and cellular organisms. *Nucleic Acids Res.* **49**, D545–D551 (2021).
67. Liu, B., Zheng, D., Zhou, S., Chen, L. & Yang, J. VFDB 2022: a general classification scheme for bacterial virulence factors. *Nucleic Acids Res.* **50**, D912–D917 (2022).
68. Buchfink, B., Reuter, K. & Drost, H. G. Sensitive protein alignments at tree-of-life scale using DIAMOND. *Nat. Methods* **18**, 366–368 (2021).
69. Wood, D. E., Lu, J. & Langmead, B. Improved metagenomic analysis with Kraken 2. *Genome Biol.* **20**, 257 (2019).
70. Lu, J., Breitwieser, F. P., Thielen, P. & Salzberg, S. L. Bracken: estimating species abundance in metagenomics data. *PeerJ Comput. Sci.* **3**, e104 (2017).
71. Chen, S., Zhou, Y., Chen, Y. & Gu, J. fastp: an ultra-fast all-in-one FASTQ preprocessor. *Bioinformatics* **34**, i884–i890 (2018).
72. Youngblut, N. D. & Ley, R. E. Struo2: efficient metagenome profiling database construction for ever-expanding microbial genome datasets. *PeerJ* **9**, e12198 (2021).
73. Dai, D. et al. GMrepo v2: a curated human gut microbiome database with special focus on disease markers and cross-dataset comparison. *Nucleic Acids Res.* **50**, D777–D784 (2022).
74. Hiseni, P., Rudi, K., Wilson, R. C., Hegge, F. T. & Snipen, L. HumGut: a comprehensive human gut prokaryotic genomes collection filtered by metagenome data. *Microbiome* **9**, 165 (2021).
75. Tanaka, Y. & Benno, Y. Application of a single-colony coculture technique to the isolation of hitherto unculturable gut bacteria. *Microbiol. Immunol.* **59**, 63–70 (2015).
76. Salanitro, J. P., Fairchilds, I. G. & Zgornicki, Y. D. Isolation, culture characteristics, and identification of anaerobic bacteria from the chicken cecum. *Appl. Microbiol.* **27**, 678–687 (1974).
77. Shigeno, Y., Kitahara, M., Shime, M. & Benno, Y. *Phascolarctobacterium wakonense* sp. nov., isolated from common marmoset (*Callithrix jacchus*) faeces. *Int. J. Syst. Evol. Microbiol.* **69**, 1941–1946 (2019).
78. Helft, J. et al. GM–CSF mouse bone marrow cultures comprise a heterogeneous population of CD11c$^+$MHCII$^+$ macrophages and dendritic cells. *Immunity* **42**, 1197–1211 (2015).
79. Onai, N. et al. Identification of clonogenic common Flt3$^+$M-CSFR$^+$ plasmacytoid and conventional dendritic cell progenitors in mouse bone marrow. *Nat. Immunol.* **8**, 1207–1216 (2007).
80. Liu, K. et al. In vivo analysis of dendritic cell development and homeostasis. *Science* **324**, 392–397 (2009).
81. Kim, S. et al. High amount of transcription factor IRF8 engages AP1-IRF composite elements in enhancers to direct type 1 conventional dendritic cell identity. *Immunity* **54**, 1622 (2021).
82. Toda, G., Yamauchi, T., Kadowaki, T. & Ueki, K. Preparation and culture of bone marrow-derived macrophages from mice for functional analysis. *STAR Protoc.* **2**, 100246 (2021).
83. Barel, M. et al. A novel receptor–ligand pathway for entry of *Francisella tularensis* in monocyte-like THP-1 cells: interaction between surface nucleolin and bacterial elongation factor Tu. *BMC Microbiol.* **8**, 145 (2008).
84. Jalal, N. & Lee, S. F. The MsrAB reducing pathway of *Streptococcus gordonii* is needed for oxidative stress tolerance, biofilm formation, and oral colonization in mice. *PLoS ONE* **15**, e0229375 (2020).
85. Morinaga, K., Yamamoto, T., Nomura, N. & Toyofuku, M. *Paracoccus denitrificans* can utilize various long-chain *N*-acyl homoserine lactones and sequester them in membrane vesicles. *Environ. Microbiol. Rep.* **10**, 651–654 (2018).
86. Yasuda, M. et al. Phage genes induce quorum sensing signal release through membrane vesicle formation. *Microbes Environ.* **37**, ME21067 (2022).
87. Hogquist, K. A. et al. T cell receptor antagonist peptides induce positive selection. *Cell* **76**, 17–27 (1994).
88. Adachi, O. et al. Targeted disruption of the *MyD88* gene results in loss of IL-1- and IL-18-mediated function. *Immunity* **9**, 143–150 (1998).
89. Hildner, K. et al. Batf3 deficiency reveals a critical role for CD8α$^+$ dendritic cells in cytotoxic T cell immunity. *Science* **322**, 1097–1100 (2008).
90. Tomura, M. et al. Tracking and quantification of dendritic cell migration and antigen trafficking between the skin and lymph nodes. *Sci. Rep.* **4**, 6030 (2014).
91. Kumagai, S. et al. Lactic acid promotes PD-1 expression in regulatory T cells in highly glycolytic tumor microenvironments. *Cancer Cell* **40**, 201–218 (2022).
92. Itahashi, K. et al. BATF epigenetically and transcriptionally controls the activation program of regulatory T cells in human tumors. *Sci. Immunol.* **7**, eabk0957 (2022).
93. Tamaki, H. et al. *Armatimonas rosea* gen. nov., sp. nov., of a novel bacterial phylum, *Armatimonadetes* phyl. nov., formally called the candidate phylum OP10. *Int. J. Syst. Evol. Microbiol.* **61**, 1442–1447 (2011).
94. Katayama, T. et al. Isolation of a member of the candidate phylum 'Atribacteria' reveals a unique cell membrane structure. *Nat. Commun.* **11**, 6381 (2020).
95. Tong, J., Liu, C., Summanen, P., Xu, H. & Finegold, S. M. Application of quantitative real-time PCR for rapid identification of *Bacteroides fragilis* group and related organisms in human wound samples. *Anaerobe* **17**, 64–68 (2011).

Acknowledgements We thank members of the SCRUM-Japan MONSTAR-SCREEN alliance for providing the cohort study data; T. Kobayashi, T. Owari, H. Nishinakamura, D. Sugiyama and M. Tomura for experimental guidance and discussion; and Y. Ka, T. Ogura, R. Takahashi, Y. Tada, T. Takaku, M. Nakai, K. Onagawa, M. Takemura, M. Hoshino, C. Ozawa, A. Takakura, K. Yoshida, Y. Osada, M. Ozawa, Y. Ohira, S. Yoshimatsu, the animal facility team at the National Cancer Center Japan, K. Morinaga, M. Takashino and R. Norimine for their technical assistance. This study was supported by the Grants-in-Aid for Scientific Research (A grant no. 22H00455 to H.N., S grant no. 25H12345 and 17H06162 to H.N., and B grant no. 24K02306 to S. Koyama) from the Ministry of Education, Culture, Sports, Science and Technology of Japan; the Japan Agency for Medical Research and Development (AMED)-CREST grant (JP18gm1010005 to H.N., H.M. and S.N.); the Moonshot Research and Development Program (grant no. 22zf0127009h0001 to H.N., H.M. and S. Koyama); the Next Generation Drug Discovery and Development Technology on Regulating Intestinal Microbiome (no. 21ae0121037h0001 to H.N. and S. Koyama); the Project for Cancer Research and Therapeutic Evolution (P-CREATE, no. 16cm0106301h0002 to H.N.); the program 'The next-generation drug discovery and development technology on regulating intestinal microbiome' (NeDDTrim) from Japan Agency for Medical Research and Development (AMED) (under the Grant Number JP 21ae0121037h0001 to H.N. and S. Koyama); the Development of Technology for Patient Stratification Biomarker Discovery (grant no. 19ae0101074s0401 to H.N.); the Project for Promotion of Cancer Research and Therapeutic Evolution (P-PROMOTE, no. 22ama221301h0001 to H.N. and S. Koyama, and no. 23ama221329h0001 to S. Koyama and K.S.); the Practical Research for Innovative Cancer Control (no. 22ck0106724h0001 to H.N. and S. Koyama, and no. 23ck0106796h001 to S. Koyama and K.S.) from AMED; the National Cancer Center Research and Development Fund (no. 28-A-7 and no. 31-A-7 to H.N., no. 2022-S-7 to S. Kumagai, no. 2022-A-4 to K.W. and no. 2024-A-03 to H.N.); the Canon Foundation (S. Koyama), the Mitsubishi Foundation (S. Koyama); the Takeda Science Foundation (S. Kumagai); the Naito Foundation (S. Kumagai); the Kobayashi Foundation for Cancer Research (H.N., S. Koyama and S. Kumagai); the Astellas Foundation for Research on Metabolic Disorders (S. Koyama); and the Yasuda Foundation (H.N.).

Author contributions N.Y.-T.L., S.F., S. Koyama, D.M., D.M.T., Y. Shigeno, T.I., Y. Matsumoto, H.Y., K.M., H.T., Y. Sekiguchi, E.S., S. Kumagai, K.I., T. Tanegashima, K.F., S.I., M.S., T. Tsuji, H.W., K.W., Y. Maeda, H.M., S.N. and H.N. performed the experiments and analysed the data. T.E., M.T., R.Y., T.F., M.N., A.K., K.G., T.D. and K.S. collected the clinical specimens and performed analyses of the clinical data. Y. Shigeno and Y.B. isolated YB328 and developed the culture system. N.Y.-T.L., S.F., S. Koyama, Y.B. and H.N. conceived the project and wrote the paper.

Competing interests S. Koyama receives research funding from Otsuka Pharmaceutical and Chugai Pharmaceutical outside this study and receives honoraria from MSD and Chugai Pharmaceutical. K.I. receives honoraria from MSD and Chugai Pharmaceutical. M.N. receives honoraria (lecture fees) from MSD, Ono Pharmaceutical and Bristol-Myers Squibb (BMS). A.K. receives personal fees from Daiichi-Sankyo, Lilly, Ono Pharmaceutical, Taiho Pharmaceutical, BMS, Merck Pharmaceutical, Sumitomo Dainippon Pharma and AstraZeneca outside this study. K.W. serves as a board member and a founder of ARC Therapies outside of this study. T.D. receives personal fees for advisory roles from Sumitomo Dainippon Pharma, Taiho Pharmaceutical, Takeda Pharmaceutical, Chugai Pharmaceutical, AbbVie, Bayer, Rakuten Medical, Otsuka Pharmaceutical, KAKEN Pharmaceutical, Kyowa Kirin, SHIONOGI, PRA Health Science, A2 Health Care, Noile-Immune Biotech, MSD, Daiichi-Sankyo, Amgen, Novartis, Boehringer Ingelheim, Janssen Pharmaceutical and Astellas Pharmaceutical; receives honoraria (lecture fees) from BMS, Rakuten Medical, Ono Pharmaceutical, Daiichi-Sankyo and AstraZeneca; and receives research funding from Lilly, MSD, Daiichi-Sankyo, Sumitomo Dainippon Pharma, Taiho Pharmaceutical, Novartis, Merck Pharmaceutical, Janssen Pharmaceutical, Boehringer Ingelheim, Pfizer, BMS, AbbVie, Eisai, IQVIA, Chugai Pharmaceutical and SHIONOGI outside this study. K.S. reports receiving personal fees for consulting and advisory roles from BMS, Takeda, Ono Pharmaceutical, Novartis, Daiichi Sankyo, Amgen, Boehringer Ingelheim, Merck Pharmaceutical, Astellas, Guardant Health Japan, Janssen, AstraZeneca, Zymeworks Biopharmaceuticals, ALX Oncology and Bayer; receiving honoraria from BMS, Ono Pharmaceutical, Janssen, Eli Lilly, Astellas and AstraZeneca; and receiving research funding (all to the institution) from Astellas, Ono Pharmaceutical, Daiichi Sankyo, Taiho Pharmaceutical, Chugai, Merck Pharmaceutical, Amgen, Eisai, PRA Health Sciences and Syneos Health, outside the submitted work. H.M. receives research grants from Ono Pharmaceutical, Daiichi Sankyo, PFDeNA, Konica-Minolta and Ambry Genetics and serves as a board member of CureGene outside this study. H.N. receives research funding and honoraria (lecture fees) from Ono Pharmaceutical, BMS, Chugai Pharmaceutical, BD Japan and MSD;

receives honoraria (lecture fees) from Amgen; receives research funding from Taiho Pharmaceutical, Daiichi-Sankyo, Kyowa Kirin, Zenyaku Kogyo, Oncolys BioPharma, Debiopharma, Asahi-Kasei, Sysmex, Fujifilm, SRL, Astellas Pharmaceutical, Sumitomo Dainippon Pharma, ARC Therapies and RIKAKEN Holdings; and serves as a scientific advisor and a founder of ARC Therapies and a scientific advisor of LTZ Therapeutics outside this study. S.F., Y.B. and H.N. are the primary inventors on pending patents 2020-165470 belonging to RIKEN and the National Cancer Center Japan. The other authors declare no competing interests.

Additional information
Supplementary information The online version contains supplementary material available at https://doi.org/10.1038/s41586-025-09249-8.
Correspondence and requests for materials should be addressed to Yoshimi Benno or Hiroyoshi Nishikawa.
Peer review information *Nature* thanks Ben Boursi and the other, anonymous, reviewer(s) for their contribution to the peer review of this work. Peer reviewer reports are available.

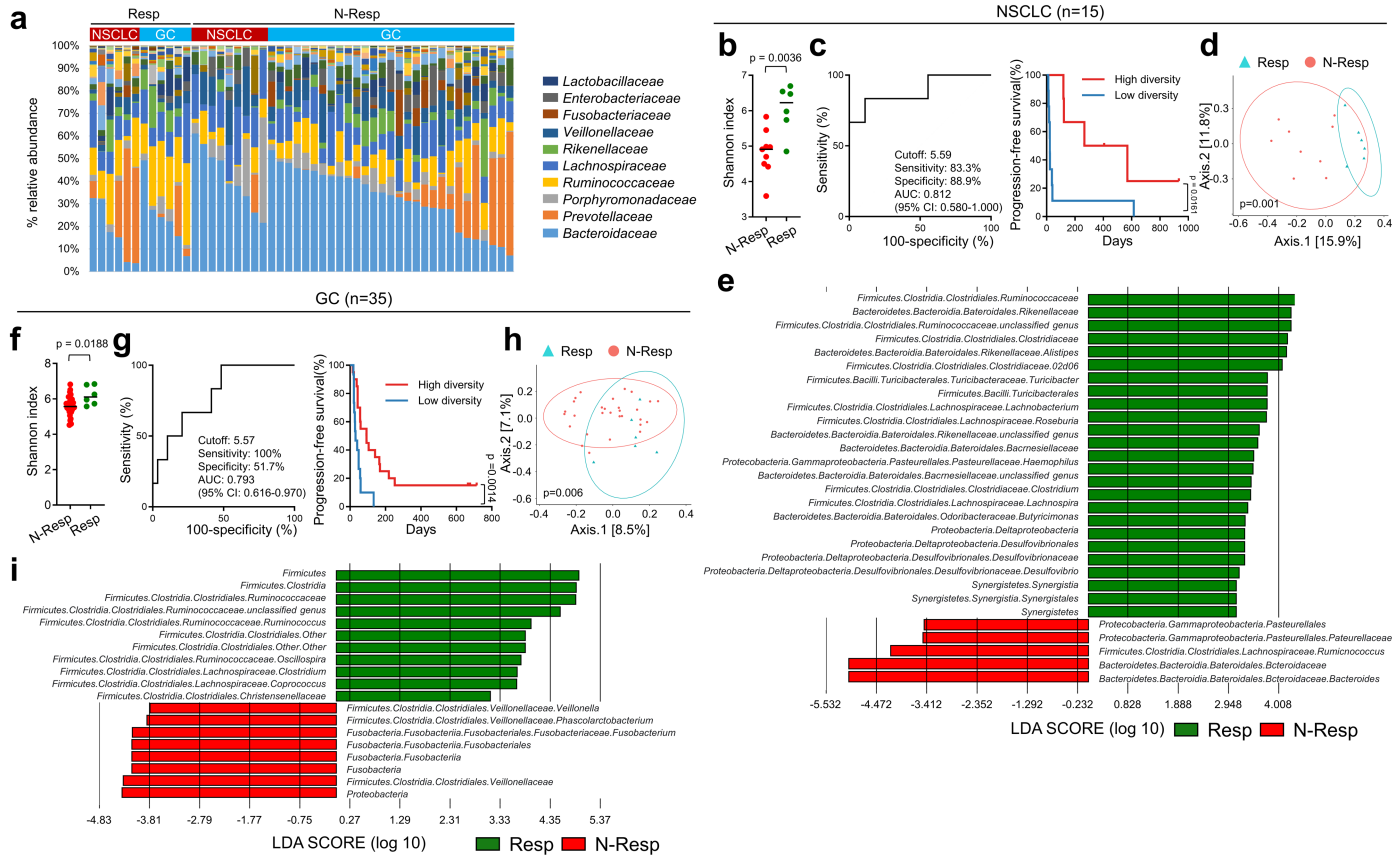

Extended Data Fig. 1 | See next page for caption.

Extended Data Fig. 1 | The microbiota significantly impacts the clinical outcome of PD-1 blockade therapy. a-i, Stacked bar plot of the bacterial abundance aggregated at the family-level. Only families with an abundance of >0.1% are shown. (**a**, n = 50 patients). Shannon diversity of the faecal microbiota in responder (Resp) and non-responder (N-Resp) patients (**b**, n = 15 patients; **f**, n = 35 patients). High/low Shannon diversity of the gut microbiota in patients was stratified by ROC analysis (left) Kaplan–Meier curves (right) for PFS of patients with high/low Shannon diversity of the gut microbiota (**c**, **g**). In NSCLC patients, the median PFS was 266 days (95% CI, 0 to 696) for those with high diversity, and 23 days (95% CI, 20 to 25) for those with low diversity. In patients with GC, the median PFS was 92 days (95% CI, 17 to 166) for those with high diversity, and 31 days (95% CI, 15 to 47) for those with low diversity (**c**, **g**). PCoA of the composition of the faecal microbiota based on unweighted Unifrac distances (**d**, **h**). Bar plots of the LDA scores of differentially abundant taxa in the Resp and N-Resp groups as determined by LEfSe analysis (**e**, **i**). **j-l**, Abundances of selected bacterial taxa. (**j**: family enriched in Resp/N-Resp represented in Fig. 1f; **l**: bacterial genera previously associated with response to immunotherapy). The ROC analysis (left) and Kaplan–Meier curves for PFS (right) for the enriched bacterial families in Fig. 1f were examined. High/low abundances of the indicated bacterial families in patients were stratified by ROC analysis (**k**). n = 50 patients. **m**, Kaplan–Meier curves for the PFS of patients stratified by the median cut-off for each indicated factor. n = 50 patients. **n**, The correlations between bacteria that were significantly correlated with the clinical course and PD-1 expression by $CD8^+$ T cells are shown. n = 26 patients. (**c**, **g**, **k, m**) Kaplan–Meier curves were analysed by the two-sided log-rank test. (**b, f**) Two-sided unpaired t test, and data are presented as the median. (**j, l**) Two-sided Mann–Whitney U test, and data are presented as the median. (**d**, **h**) ANOSIM, with one-tailed significance computed by permutation (n = 999 permutations). (**n**) The correlation was evaluated by two-sided Pearson's correlation analysis.

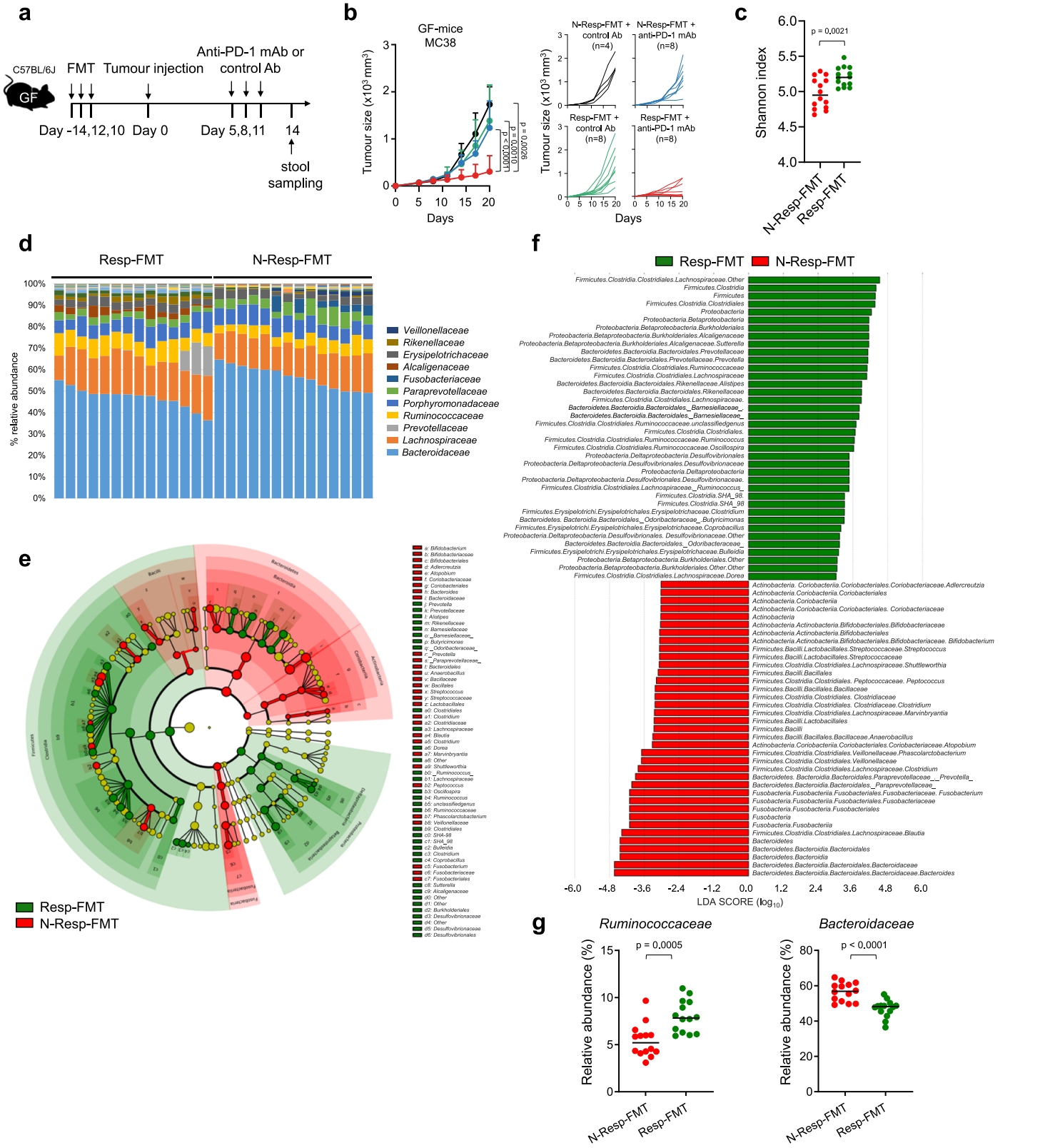

Extended Data Fig. 2 | FMT from patients influences the diversity and composition of the gut microbiota. a-g, GF mice transplanted with faeces from Resps or N-Resps were subcutaneously injected with MC38 tumour cells. Experimental scheme (**a**). Tumour growth curves (**b**, left: summary, right: each mouse). n = 4–8 mice per group. **c-g**, The faecal samples were subjected to 16S rRNA gene sequencing to analyse the bacterial composition. The alpha diversity of the gut microbiota was scored by the Shannon index (**c**). Stacked bar plot of the family-level taxonomic composition of the faeces of Resp-FMT/N-Resp FMT mice. Only families with an abundance of >0.1% are shown (**d**). Differentially abundant taxa were analysed by LEfSe, the symbol sizes are scaled by relative abundance (**e**). The bar plot showed the LDA scores of differentially abundant taxa between the Resp and N-Resp groups (**f**). The relative abundance of *Ruminococcaceae* (left) and *Bacteroidaceae* (right)(**g**). n = 14 mice per group. (**b**, left), The average tumour sizes of the groups on a certain day of the experiment are shown as dots and are presented as the mean ± SD, two-way ANOVA with the Tukey—Kramer method. Each dot indicates one mouse, and the data are presented as the median (**c**, **g**). (**c**, **g**) Two-sided unpaired t test.

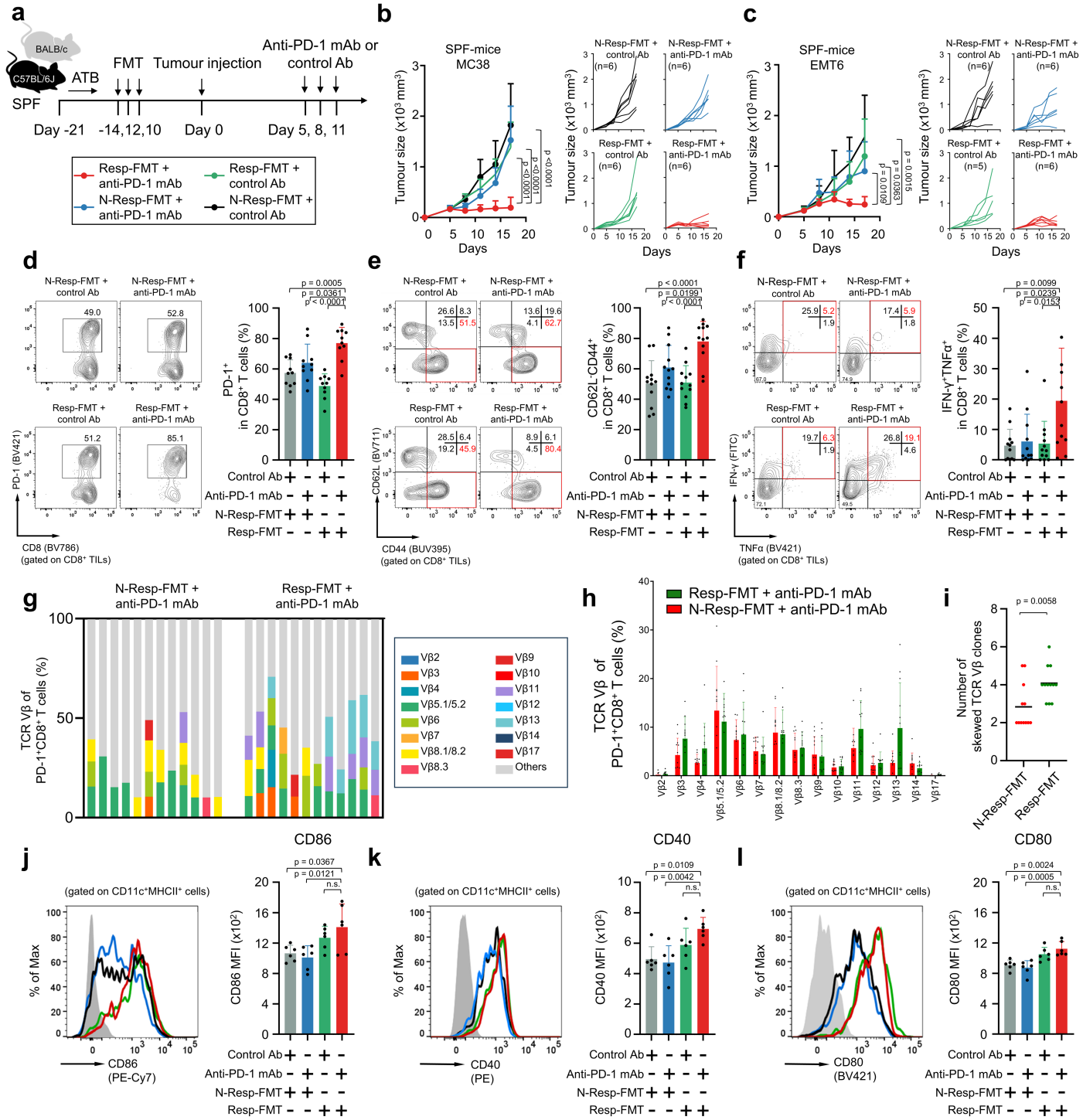

Extended Data Fig. 3 | Faecal transplantation from patients who responded to PD-1 blockade therapy inhibits tumour progression and augments antitumour immunity. a-l, ATB-SPF mice were transplanted with faeces from Resp or N-Resp mice following the subcutaneous injection of tumour cells. Experimental scheme (**a**). Tumour growth curves of MC38 (**b**, left: summary, right: each mouse) and EMT6 (**c**, left: summary, right: each mouse) tumour models. n = 5–6 mice per group. **d-f**, The frequency [representative staining (left) and % summary (right)] of effector molecule expression [PD-1 (**d**, n = 10) and CD62L/CD44 (**e**, n = 12)] and cytokine (IFN-γ/TNFα) production (**f**, n = 12) by $CD8^+$ T cells. **g-i**, TCR Vβ repertoire of $PD\text{-}1^+CD8^+$ T cells (**g, h**). Numbers of skewed TCR Vβ clones (percentages of clones >10%) of $PD\text{-}1^+CD8^+$ T cells (**i**). n = 12 mice per group. **j-l**, The expression [representative staining (left) and MFI summary (right)] of maturation markers [CD86 (**j**), CD40 (**k**) and CD80 (**l**)] by DCs. n = 6 mice per group. (**b**, left; **c**, left), The average tumour sizes of the groups on a certain day of the experiment are shown as dots and are presented as the mean ± SD. (**d-l**) Each dot indicates one mouse, and the data are presented as the mean (**i**) or mean ± SD (**d-f, h, j-l**). (**b, c**) Two-way ANOVA with the Tukey–Kramer method. (**d-f, j-l**), One-way ANOVA with Bonferroni correction. (**i**) Two-sided Mann–Whitney U test.

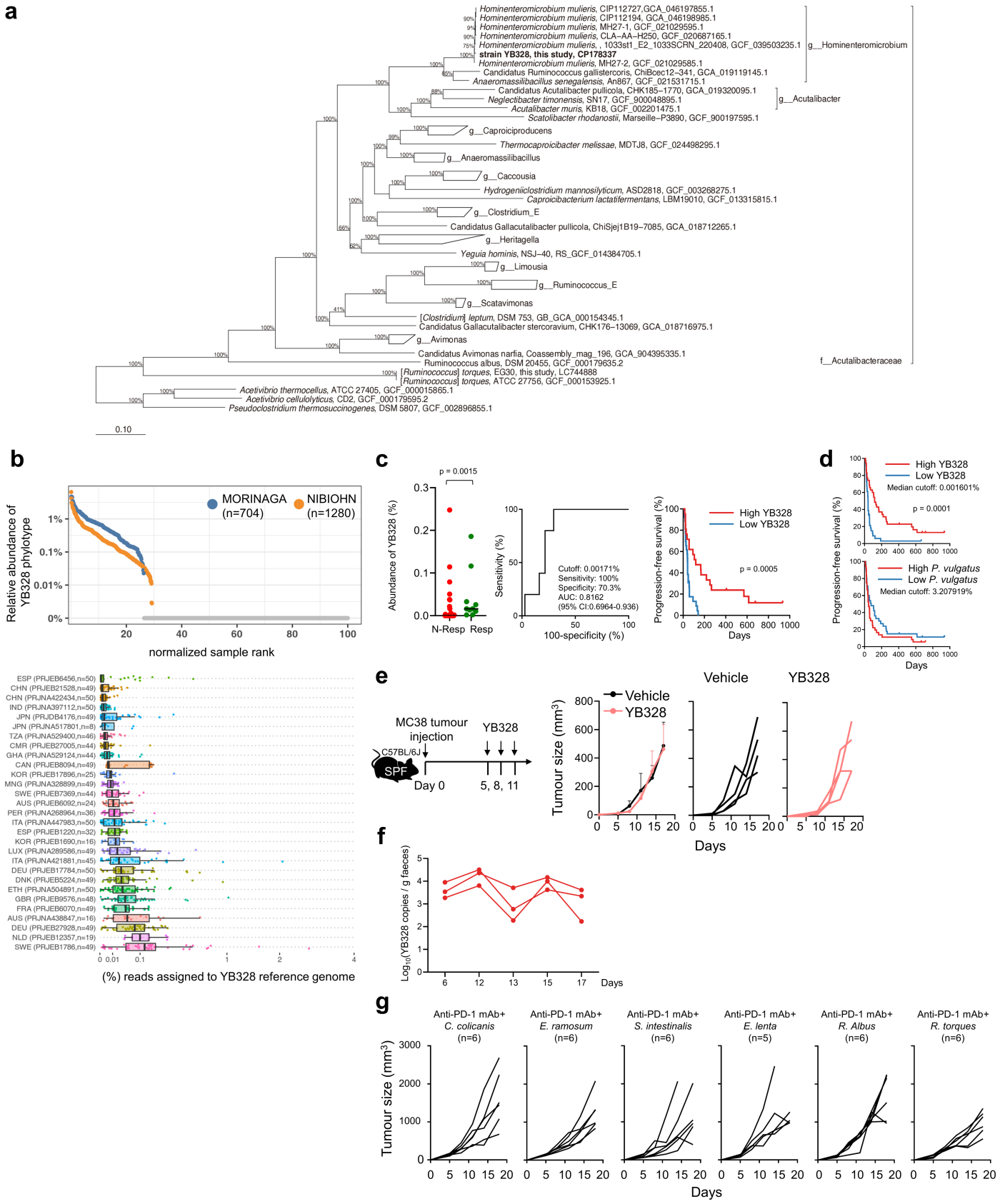

Extended Data Fig. 4 | See next page for caption.

Extended Data Fig. 4 | A bacterium identified from the faeces of Resps is classified as the novel strain YB328. a, Genome-based phylogenetic tree showing the position of strain YB328 in the family *"Acutalibacteriaceae"* in the GTDB v220. Species names, strain identifiers and genome sequence accession numbers are presented in the tip labels, if applicable. Scale bar represents 10% amino-acid substitutions per site. **b**, Abundance of the YB328-related bacteria in: (upper panel) healthy Japanese individuals based on publicly available 16S rRNA gene sequencing data of two cohorts (MORINAGA cohort: n = 704 patients; NIBIOHN cohort: n = 1280 patients), and (lower panel) individuals from 21 countries across the world based on shotgun metagenomics data. For the upper panel, each symbol represents a different dataset. For the lower panel, abundances were calculated as the percentage of metagenomic reads assigned to the YB328 reference genome in our custom GTDB-based database. Text labels on the y-axis indicate the country of origin, and in parentheses the BioProject and the number of datasets included in the analysis. For the box plots, the thick line within each box shows the median, the boxes represent the interquartile range (IQR), and the whiskers extend to the furthest data point within 1.5 times the IQR of the box. **c**, Faecal samples from patients, excluding MSI-H patients (NSCLC: n = 15; GC: n = 32), were subjected to shotgun metagenomic sequencing. Analyses of the relative abundances of the YB328 using Kraken2+Bracken with a custom version of the GTDB (left panel). High/low bacterial abundance was stratified by a ROC curve analysis (middle panel). Kaplan–Meier curves (right panel) of the PFS of patients with high/low faecal bacterial abundance are shown. **d**, High/low bacterial abundance of all GC/NSCLC patients (NSCLC: n = 22; GC: n = 49), stratified by the median cut-off value, was used to plot Kaplan–Meier curves of the PFS of patients. **e**, Experimental scheme (left) and tumour growth curves (middle: summary, right: each mouse). Average tumour sizes of the groups on a certain day of the experiment are shown as dots and are presented as the mean ± SD. n = 4 mice per group. **f**, YB328 colonisation detected in faecal sample by qPCR, n = 3 mice per group. **g**, The tumour growth curves are shown. Each line represents one mouse. n = 5–6 mice per group. (**c**, left panel) Two-sided Mann–Whitney U test and data are presented as the median. (**c**, right panel; **d**) Two-sided log-rank test.

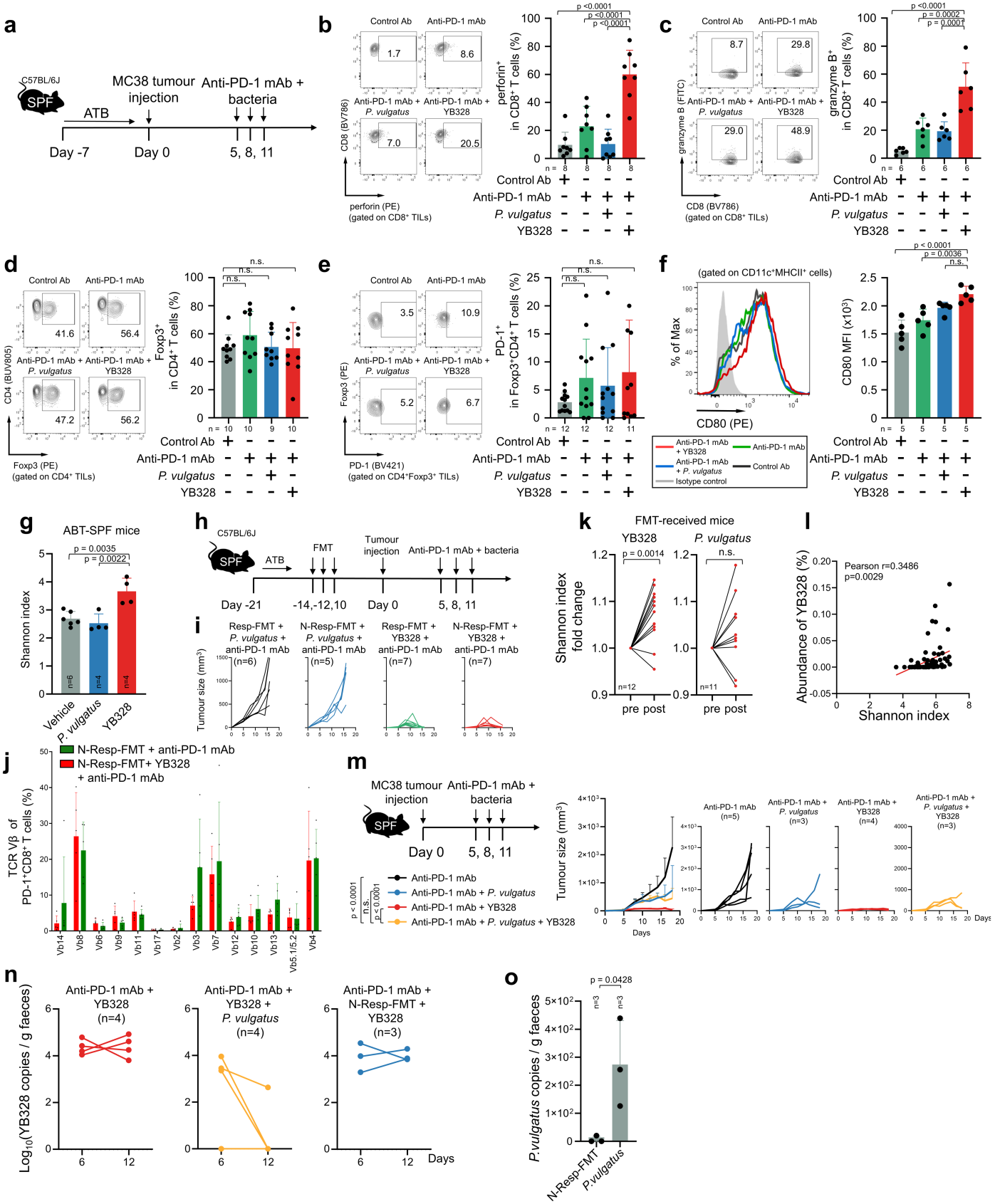

Extended Data Fig. 5 | See next page for caption.

Extended Data Fig. 5 | YB328 administration changes the immunological landscape of the TME. a-g, Experimental scheme (**a**). The frequency [representative staining (left) and % summary (right)] of effector molecule [perforin (**b**) and granzyme B (**c**)] production by $CD8^+$ T cells. The frequency [representative staining (left) and % summary (right)] of $Foxp3^+$ cells in $CD4^+$ T cells (**d**) and PD-1 expression by $Foxp3^+CD4^+$ T cells (**e**). Expression [representative staining (left) and MFI summary (right)] of the maturation marker CD80 (**f**) by $CD11c^+MHCII^+$ DCs. n = 5–12 mice per group. **g**, Shannon diversity of microbiota after the administration of the indicated treatment. n = 4–6 mice per group. **h-k**, Experimental scheme (**h**). Tumour growth curves (**i**, n = 5–7 mice per group). Profile of the TCR Vβ repertoire in PD-1^+CD8^+ T cells (**j**, n = 5 mice per group). Changes in the Shannon index of microbiota diversity (**k**, n = 11–12 mice per group). **l**, The correlation between the abundance of YB328 and the Shannon index of microbiota diversity in all GC/NSCLC patients (NSCLC: n = 22; GC: n = 49) in this study. **m**, The experimental scheme is shown (left panel). Tumour growth curves (middle panel: summary; right panel: each mouse). n = 3–5 mice per group. **n-o**, ATB-SPF or N-Resp-FMT recipient mice received the indicated bacterial treatment. Bacterial engraftment was assessed. n = 3–4 mice per group. (**b-g**, **j, k, n-o**) Each dot in the summary graphs indicates one mouse in the in vivo experiment. (**b-g**, **j, o**) The data are presented as the means ± SD. (**m**, middle) The average tumour size of the groups on a certain day is shown as a dot. (**i, m** left panel) Each line indicates one mouse for the in vivo experiment. (**l**) Each dot indicates one patient. (**b-g**) One-way ANOVA with Bonferroni's correction. (**k**) Two-sided paired t test. (**l**) The correlation coefficient was evaluated by two-sided Pearson's correlation analysis. (**m**) Two-way ANOVA with the Tukey–Kramer method. (**o**) Two-sided unpaired t test.

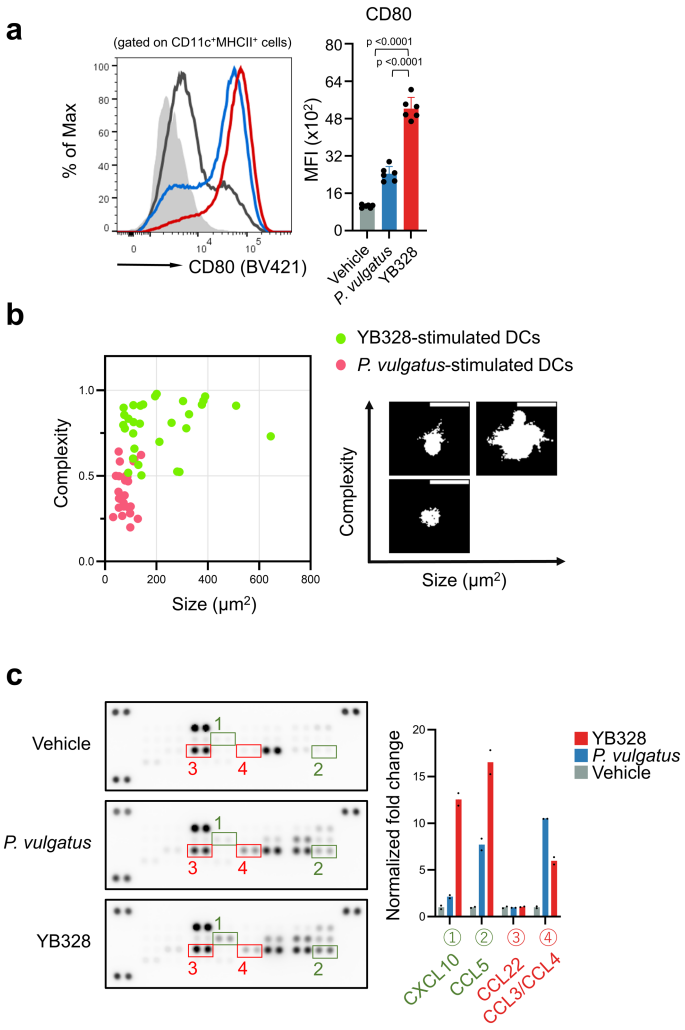

Extended Data Fig. 6 | YB328-stimulated BMDCs differentiate into mature CD103⁺CD11b⁻ cDCs and produce CXCL10 to attract CD8⁺ T cells. a, BMDCs were stimulated with *P. vulgatus* or YB328. The expression [representative staining (left) and MFI summary (right)] of the maturation marker CD80. n = 6 wells per group. **b**, The complexity and size of DCs (n = 30 in each group from Supplementary Video 1) stimulated with YB328 or *P. vulgatus* were evaluated. A representative correlation model for DCs is shown in the binary image. Scale bar: 10 μm. **c**, Chemokine production by YB328-, *P. vulgatus*- or vehicle-treated BMDCs was examined with a proteome profiler chemokine antibody array. Representative data (left) and quantified as fold changes (right) are shown. n = 2 technical replicates. (**a**) One-way ANOVA with Bonferroni correction. Each dot in the summary graphs indicates one well, and the data are presented as the mean ± SD. (**b**) Each dot indicates one cell. (**c**) Data are presented as the mean.

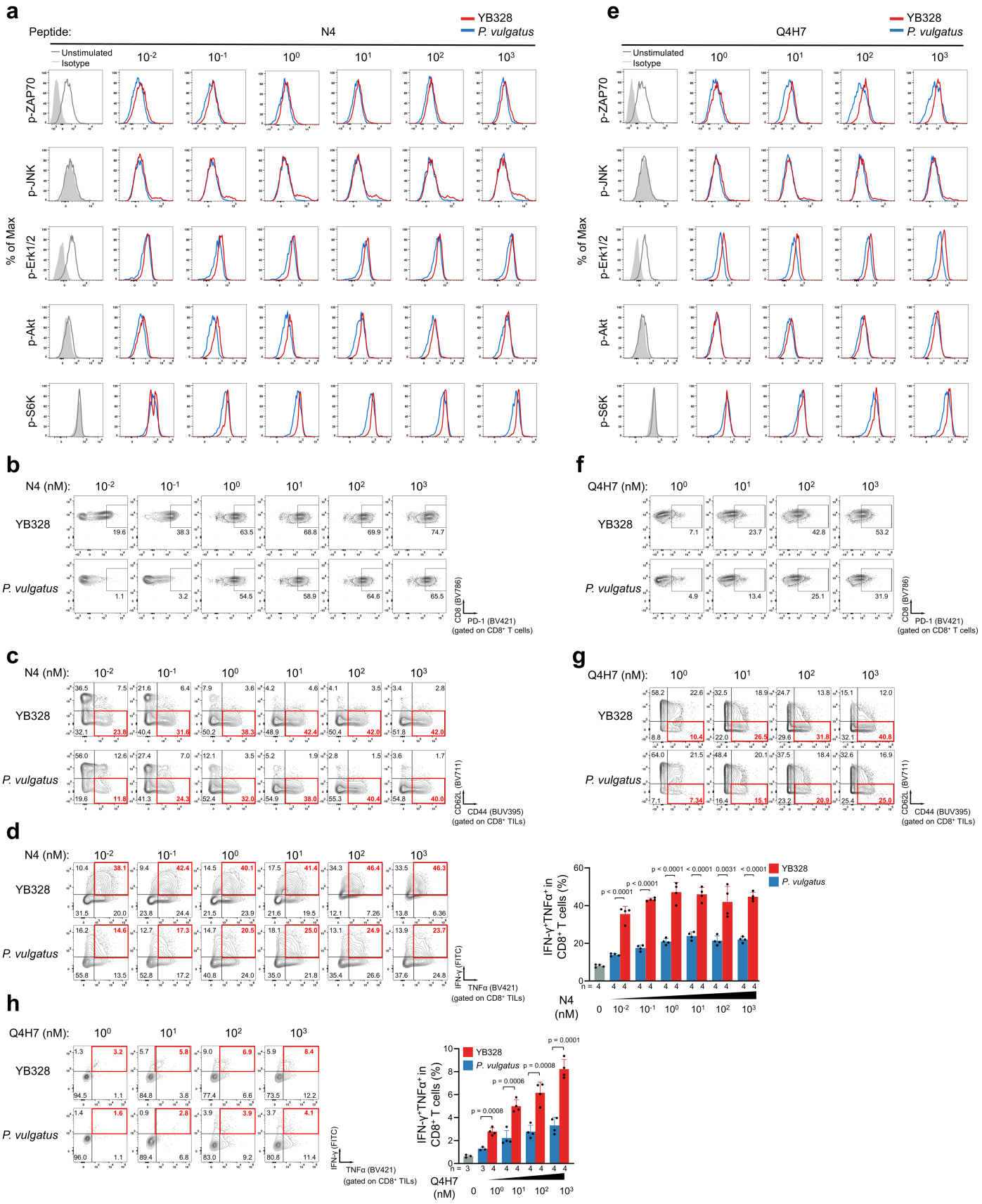

Extended Data Fig. 7 | See next page for caption.

Extended Data Fig. 7 | YB328-stimulated BMDCs deliver robust TCR signals to activate CD8$^+$ T cells. a-h, OT-I CD8$^+$ T cells were cocultured with bacteria-treated BMDCs pulsed with the indicated antigen peptides (**a-d**, N4 peptide; **e-h**, Q4H7 peptide). (**a**, **e**), Representative data showing the expression of TCR signalling molecules (p-ZAP70, p-JNK, p-Erk1/2, p-Akt and p-S6K) by CD8$^+$ T cells after stimulation with DCs pulsed with the indicated concentrations of peptides. (**b**, **f**), Representative data of PD-1 expression by CD8$^+$ T cells after stimulation with DCs pulsed with the indicated concentrations of peptides. (**c**, **g**), Representative data of CD62L/CD44 expression by CD8$^+$ T cells after stimulation with DCs pulsed with the indicated concentrations of peptides. (**d**, **h**), Cytokine (IFN-γ and TNFα) production [representative staining (left) and % summary (right)] by CD8$^+$ T cells after stimulation with DCs pulsed with the indicated concentrations of peptides. n = 3–4 wells per group. The data were analysed by a two-sided unpaired t test and presented as the mean ± SD.

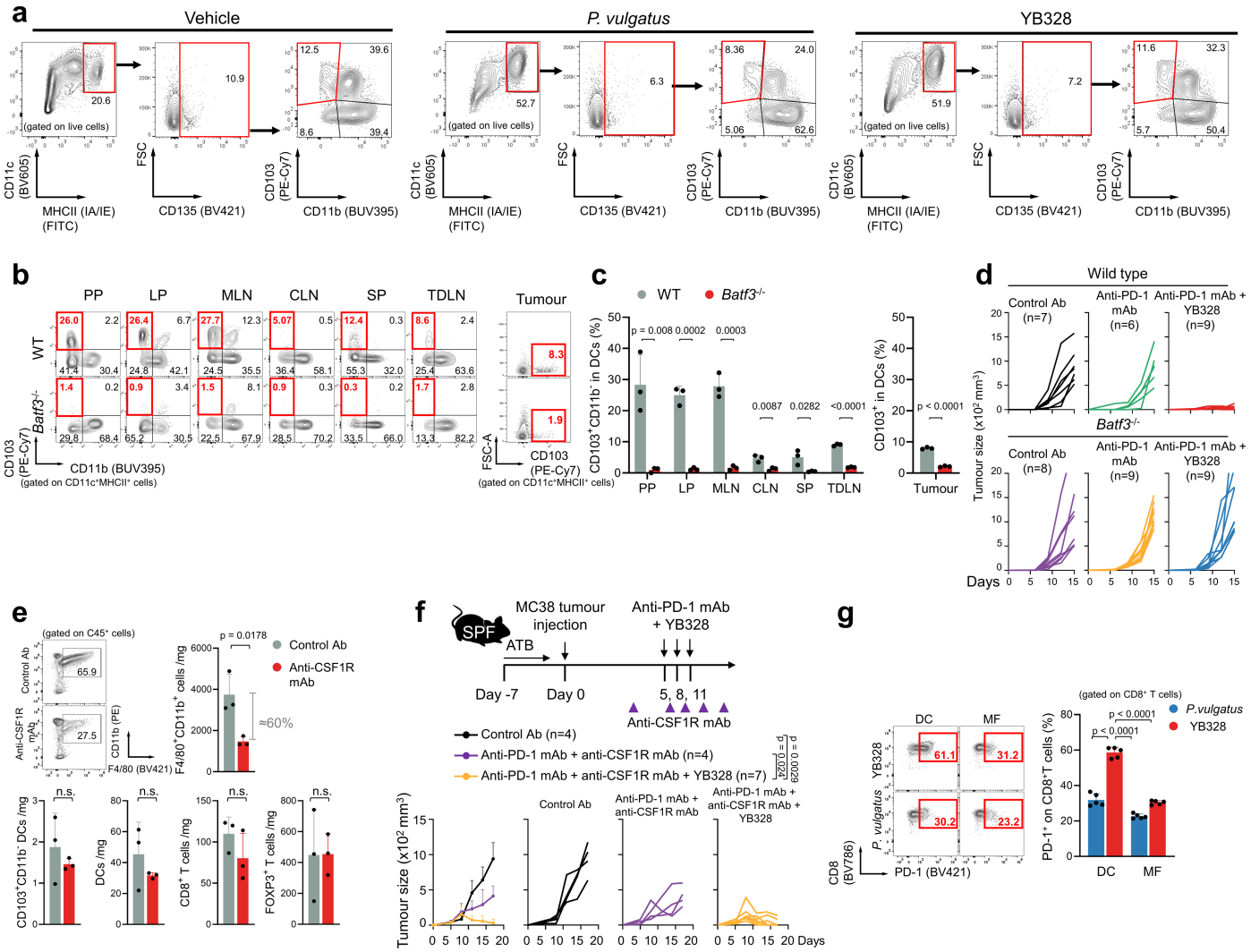

Extended Data Fig. 8 | YB328 treatment induces CD103$^+$CD11b$^-$ cDC generation to augment antitumour immunity of anti-PD-1 mAb. **a**, A representative gating strategy for evaluating the progeny of CD103$^+$CD11b$^-$ cDCs in BMDCs stimulated with YB328, *P. vulgatus*, or vehicle, corresponding to Fig. 4d. **b-c**, Representative staining (**b**) of the phenotype of CD103$^+$CD11b$^-$ cDCs (% summary: **c**, left panel) or CD103$^+$ DCs (% summary: **c**, right panel) in the indicated organs of WT or *Batf3*$^{-/-}$ MC38 tumour-bearing mice (n = 3). **d**, Tumour growth curves (n = 6–9). **e-f**, ATB-SPF mice were subcutaneously injected with MC38 cells and administered an anti-PD-1 mAb, anti-CSF1R mAb or control Ab with/without YB328 treatment. Changes in the immunological landscape are shown (**e**, n = 3). The experimental scheme (**f**, upper panel) and tumour growth curves (**f**, lower-left: summary, lower-right: each mouse) (**f**, n = 4–7). **g**, OT-I CD8$^+$ T cells were cocultured with bacteria-treated BMDCs (DC) or BMDMs (MF) pulsed with antigen peptides. The frequency of PD-1 expression [representative staining (left) and % summary (right)] by OT-I CD8$^+$ T cells is shown (n = 5 biologically replicates). (**d**; **f**, lower-right) Each line indicates one mouse for the in vivo experiment. The average tumour size of the groups on a certain day is shown as a dot and are presented as the mean ± SD (**f**, lower-left). Each dot in the summary graphs indicates one mouse in the in vivo experiment, and the data are presented as the mean ± SD (**c**, **e**). Each dot in the summary graphs indicates a well, and the data are presented as the mean ± SD (**g**). (**c, e**), Two-sided unpaired t test. (**f**) Two-way ANOVA with the Tukey–Kramer method. (**g**) One-way ANOVA with Bonferroni's correction.

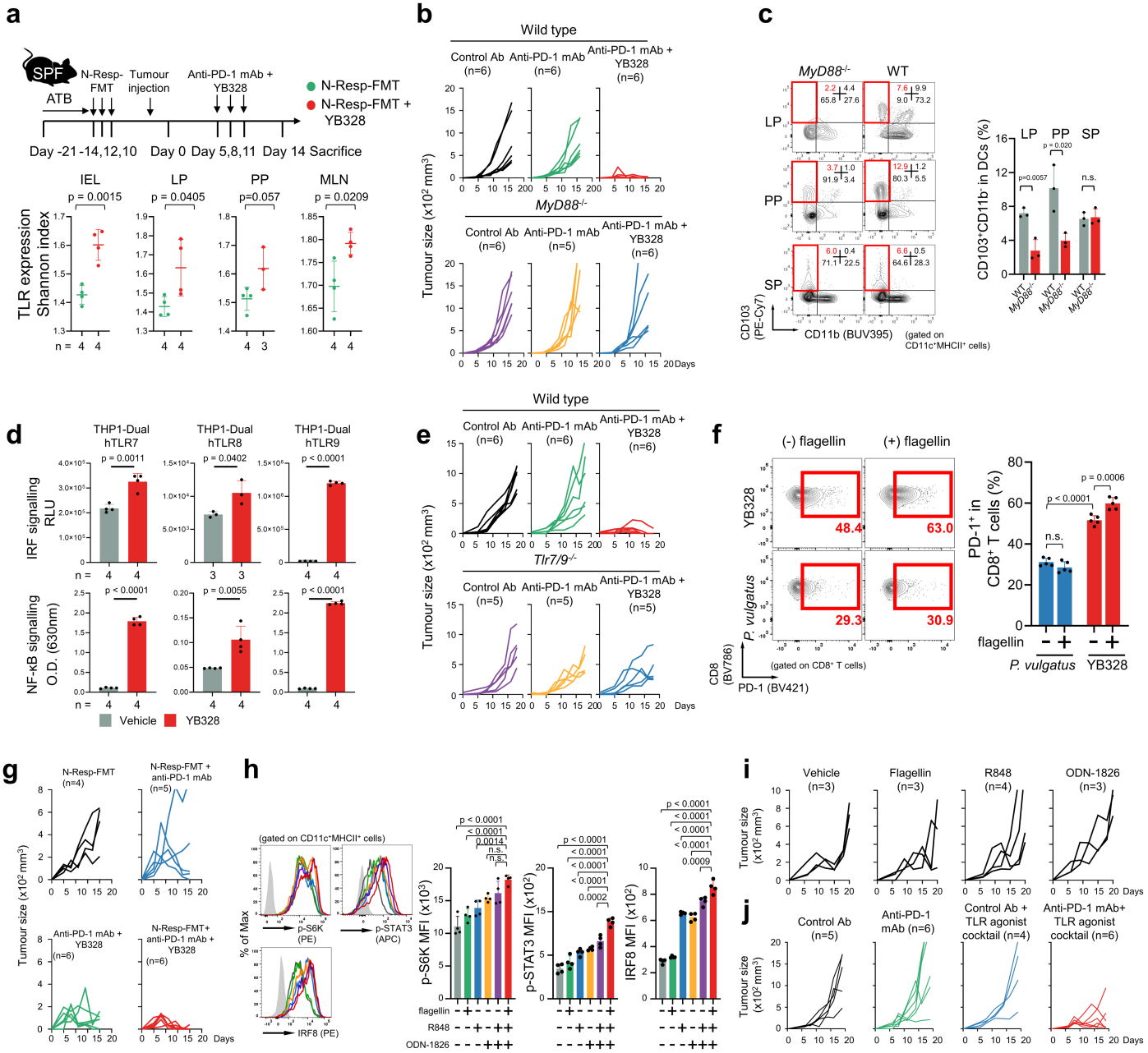

Extended Data Fig. 9 | YB328 treatment induces CD103$^+$CD11b$^-$ cDC generation and sensitises DCs to multiple TLR ligands via MyD88 signalling. a, The expression of TLRs (TLR1–TLR9) by GALT-isolated DCs was examined (upper panel, experimental scheme). The diversity of the expression of TLRs by DCs was calculated by the Shannon index (lower panel), n = 3–4. IEL: Intraepithelial lymphocyte. **b**, Tumour growth curves of each mouse in Fig. 4n are shown, n = 5–6. **c**, The frequency of CD103$^+$CD11b$^-$ cDCs [representative staining (left panel) and % summary (right panel)] in the indicated organs of WT or *MyD88*$^{-/-}$ mice (n = 3). **d**, Assessment of IRF signalling (upper panel) and NF-κB activity (lower panel) in TLR reporter THP-1 cells treated with/without YB328 (n = 3–4). **e**, Tumour growth curves of each mouse in Fig. 4s are shown. (n = 5–6). **f**, BMDCs were stimulated with YB328 or *P. vulgatus* at an MOI of 25 and then treated with flagellin. OT-I CD8$^+$ T cells were cocultured with the stimulated BMDCs pulsed with 1 nM N4 peptides. PD-1 expression by CD8$^+$ T cells [representative staining (left panel) and % summary (right panel)] is shown, n = 5. **g**, Tumour growth curves of each mouse in Fig. 4t. are shown. n = 4–6 mice per group. **h**, BMDCs were treated with the indicated TLR ligands. The levels [representative staining (left panel) and MFI summary (right panel)] of p-S6K, p-STAT3 and IRF8 are shown (n = 4). **i**, Tumour growth curves (n = 3–4). **j**, Tumour growth curves of each mouse in Fig. 4v. is shown. n = 4–6. (**b**, **e**, **g**, **i**-**j**) Each line indicates one mouse for the in vivo experiment. (**a**, **c**) Each dot in the summary graphs indicates one mouse in the in vivo experiment, and the data are presented as the mean ± SD. (**d**, **f**, **h**) Each dot in the summary graphs indicates a well, and the data are presented as the mean ± SD. (**a**, **c**-**d**), Two-sided unpaired t test. (**f**, **h**) One-way ANOVA with Bonferroni's correction.

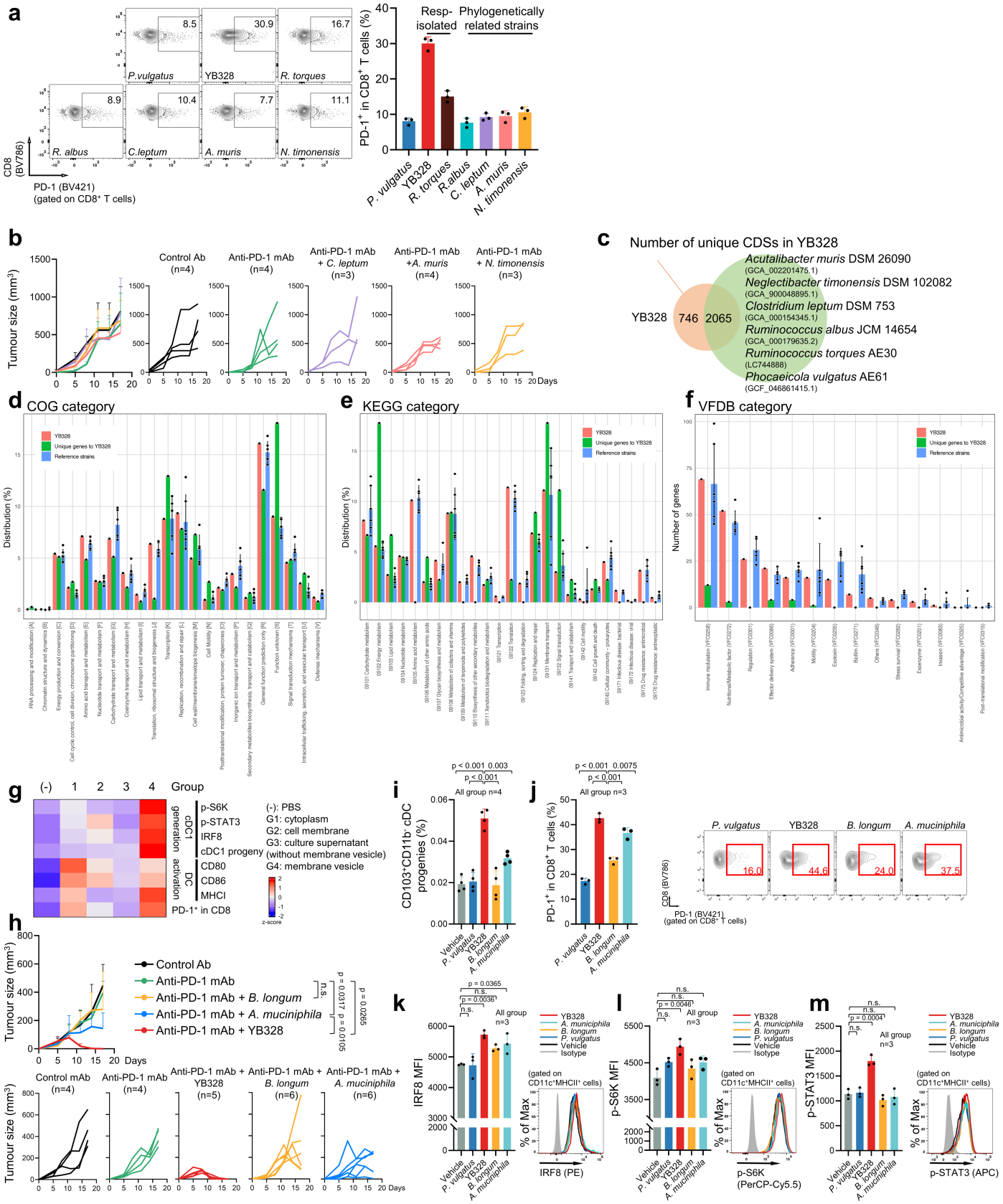

Extended Data Fig. 10 | See next page for caption.

Extended Data Fig. 10 | Specific genomic traits and phenotypic features of YB328 are involved in antitumour effects and their responsible factors. **a**, BMDCs were stimulated with bacterial strains that were isolated from Resps or were genomically similar to YB328. OT-I $CD8^+$ T cells were cocultured with bacteria-treated BMDCs pulsed with N4 peptides (10 nM). The frequency [representative staining (left) and % summary (right)] of PD-1 expression by $CD8^+$ T cells. n = 3 wells per group. **b**, Tumour growth curves (left: summary, right: each mouse). n = 3–4 mice per group. **c-f**, Comparative genomics of YB238 and other six strains (referred to as "Reference strains") Venn diagram indicating the number of genes unique to YB328 (**c**). Bar plots of the distribution of genes annotated to different categories according to COG (**d**), KEGG (**e**), and VFDB (**f**). Values were calculated for all genes of YB328 (red bars), genes unique to YB328 (green bars), and the other six strains (blue bars show the mean ± SD). **g**, BMDCs were treated with each of four cell culture fractions of YB328 [G1: cytoplasm, G2: cell membrane, G3: culture supernatant (without membrane vesicle) or G4: membrane vesicle] and cocultured with OT-I $CD8^+$ T cells stimulated with N4 peptide-pulsed DCs. The expression of the indicated proteins was measured by flow cytometry (n = 3) and normalized between samples. cDC1: $CD103^+CD11b^-$ cDCs. **h**, Tumour growth curves (upper: summary, lower: each mouse). n = 4–6 mice per group. **i-m**, BMDCs were stimulated with the indicated bacterial strains. OT-I $CD8^+$ T cells were cocultured with bacteria-treated BMDCs pulsed with N4 peptides (10 nM). Changes in the progeny of the $CD103^+CD11b^-$ population (**i**). The frequency [% summary (left) and representative staining (right)] of PD-1 expression by $CD8^+$ T cells (**j**). The expression of IRF8 (**k**), p-S6K (**l**) and p-STAT3 (**m**) in BMDCs. The MFI summary (left) and representative staining (right) are shown. n = 3–4 wells per group. (**a, i-m**) Each dot indicates one well for the in vitro experiment in the summary data. (**b**, left; **h**, upper) The average tumour sizes of the groups on the day of the experiment are shown as dots and are presented as the mean ± SD. (**b**, right; **h**, bottom) Each line represents one mouse. (**a**, **i-m**) Data are presented as the mean ± SD. (**i-m**) One-way ANOVA with Bonferroni correction. (**h**) Two-way ANOVA with the Tukey–Kramer method.

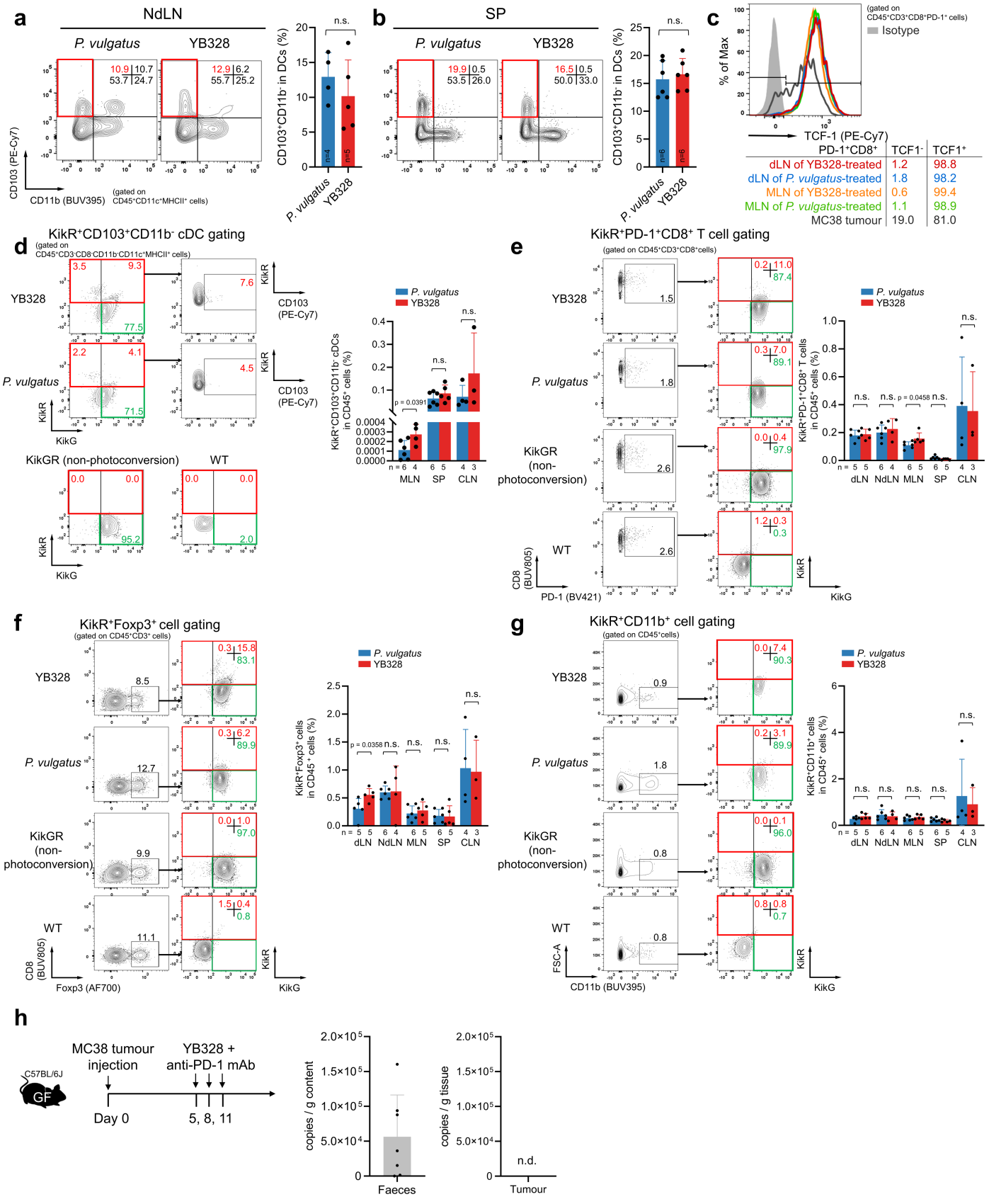

Extended Data Fig. 11 | See next page for caption.

Extended Data Fig. 11 | YB328 treatment increases CD103$^+$CD11b$^-$ cDCs in tumour-related tissues to activate CD8$^+$ T cells. a-c, ATB-SPF mice were subcutaneously injected with MC38 cells and treated with the indicated bacteria. The phenotype and frequency [representative staining (left) and % summary (right)] of DC populations in the indicated organs were examined: NdLNs (**a**) and SPs (**b**). n = 4–6 mice per group. TCF-1 expression by PD-1$^+$CD8$^+$ T cells in the indicated organs after the indicated treatment. Representative staining (upper) and % summary (lower) (**c**). **d-g**, KikGR mice pretreated with ATB were injected subcutaneously with MC38 cells and treated with the indicated bacteria. Before bacterial treatment, KikGR mice were surgically photoconverted. Migratory intestinal cells that expressed KikR$^+$ were profiled in the indicated organs. The frequency [representative staining (left) and % summary (right)] of KikR$^+$CD103$^+$CD11b$^-$ DCs (**d**), KikR$^+$PD-1$^+$CD8$^+$ T cells (**e**), KikR$^+$Foxp3$^+$ T cells (**f**) and KikR$^+$CD11b$^+$ cells (**g**) among CD45$^+$ cells. n = 3–6 mice per group. **h**, WT GF mice were subcutaneously injected with MC38 cells and were administered an anti-PD-1 mAb with YB328 treatment. Faeces were collected after the 24 h of the first administration of YB328. Tumour were collected at days 20. The presence of YB328 was examined. n.d., not detected. n = 7 mice per group. Each dot in the summary graphs indicates one mouse. All the data are presented as the mean ± SD. (**a**, **b**, **d-g**) Two-sided unpaired Student's t test.

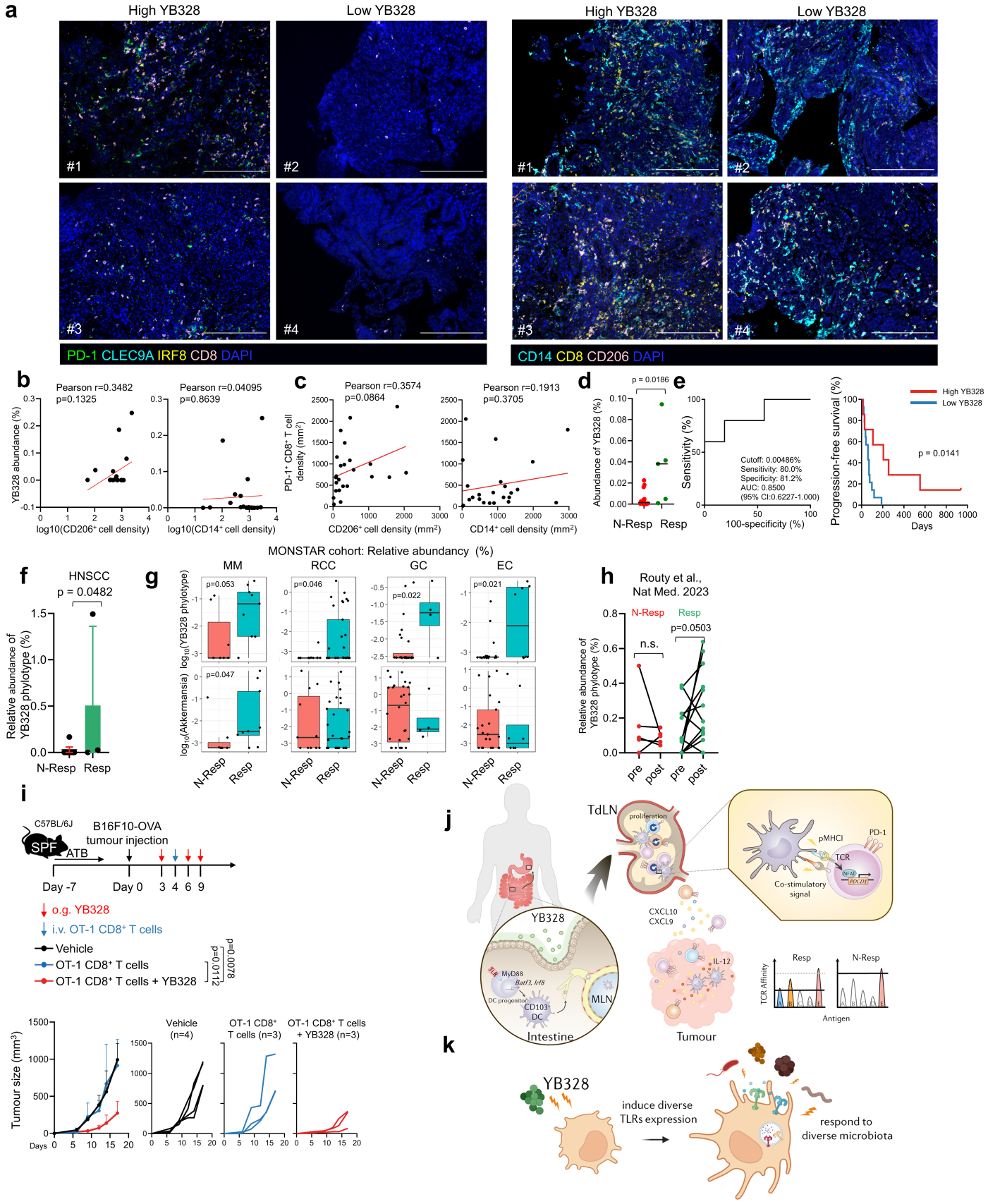

Extended Data Fig. 12 | See next page for caption.

Extended Data Fig. 12 | The abundance of YB328 is associated with the response to anti-PD-1 therapy in human cancers. a-c, Representative images of multiplex immunohistochemical staining of tumours from GC patients (**a**) and the calculated density of immune cells. Correlations between the relative abundance of YB328 in the gut microbiota and the density of $CD206^+$ cells (left) or $CD14^+$ cells (right) (**b**, n = 20). Correlations between PD-1^+CD8^+ T cells and $CD206^+$ cells (left panel) or $CD14^+$ cells (right panel) infiltration (**c**, n = 24). The correlation coefficient was evaluated by two-sided Pearson's correlation. Scale bar: 200 μm. **d**, YB328 abundance in faeces from patients in the validation cohort (n = 21; NSCLC:7; GC:14). **e**, High/low YB328 abundance was stratified by a ROC curve analysis (left panel) Kaplan–Meier curves for the PFS of patients with high/low YB328 abundance in the validation cohort (right panel). **f**, Relative abundance of the YB328 phylotype in the HNSCC cohort (n = 16). **g, h**, Relative abundance of the YB328 phylotype (**g**, **h**), and *Akkermansia* (**g**) in faecal samples across datasets from multiple cohorts. [g: MONSTAR cohort[47] (MM n = 16; RCC n = 44; GC n = 32; EC n = 29), h: Routy et al.[48] (n = 20)]. A pseudocount was added for visualization purposes, and the boxplots denote the median with a interquartile range, and the whiskers extend to the furthest data point within 1.5 times the interquartile range (**g**). **i**, ATB-SPF mice were subcutaneously injected with B16F10-OVA cells, and OT-I $CD8^+$ T cells were transferred with/without YB328 treatment. Experimental scheme (upper). Tumour growth curves (lower left: summary, mean ± SD; lower right: each mouse). The graph shows representative data from two independent experiments. n = 3–4 mice per group. **j, k**, Graphical summaries of the mechanism by which the gut microbiota augments the antitumour efficacy of PD-1 blockade therapy. (**k**) was created using BioRender (https://www.biorender.com). Data are presented as the median (**d**) or mean ± SD (**f**). (**b-d**, **f-h**) Each dot indicates one patient. (**d**, **f, g**) Two-sided Mann–Whitney test. (**e**, right) Two-sided log-rank test. (**h**) Two-sided paired t test. (**i**) Two-way ANOVA with the Tukey–Kramer method.

nature portfolio

Corresponding author(s): Hiroyoshi Nishikawa

Last updated by author(s): May 10, 2025

Reporting Summary

Nature Portfolio wishes to improve the reproducibility of the work that we publish. This form provides structure for consistency and transparency in reporting. For further information on Nature Portfolio policies, see our Editorial Policies and the Editorial Policy Checklist.

Statistics

For all statistical analyses, confirm that the following items are present in the figure legend, table legend, main text, or Methods section.

n/a	Confirmed	
☐	☒	The exact sample size (*n*) for each experimental group/condition, given as a discrete number and unit of measurement
☐	☒	A statement on whether measurements were taken from distinct samples or whether the same sample was measured repeatedly
☐	☒	The statistical test(s) used AND whether they are one- or two-sided *Only common tests should be described solely by name; describe more complex techniques in the Methods section.*
☐	☒	A description of all covariates tested
☐	☒	A description of any assumptions or corrections, such as tests of normality and adjustment for multiple comparisons
☐	☒	A full description of the statistical parameters including central tendency (e.g. means) or other basic estimates (e.g. regression coefficient) AND variation (e.g. standard deviation) or associated estimates of uncertainty (e.g. confidence intervals)
☐	☒	For null hypothesis testing, the test statistic (e.g. *F*, *t*, *r*) with confidence intervals, effect sizes, degrees of freedom and *P* value noted *Give P values as exact values whenever suitable.*
☒	☐	For Bayesian analysis, information on the choice of priors and Markov chain Monte Carlo settings
☒	☐	For hierarchical and complex designs, identification of the appropriate level for tests and full reporting of outcomes
☐	☒	Estimates of effect sizes (e.g. Cohen's *d*, Pearson's *r*), indicating how they were calculated

Our web collection on statistics for biologists contains articles on many of the points above.

Software and code

Policy information about availability of computer code

Data collection

Flow cytometry data were collected by BDFACS Diva software (ver8.0.3).

QuantitativePCR data were collected using QuantStudio Real-Time PCR Software (ver1.3).

Videos were collected using NIS-Elements AR software (ver5.01.00) or ZEN 2 software (black edition).

Confocal images were collected using ZEN 2 software (black edition).

Blot images were collected using LAS-4000 (GE Healthcare) with ImageQuant LAS4000 Control Software (ver1.2.0).

Absorbance values were measured using SkanIt Software Research Edition (ver6.1).

Luminescence values were measured using Gen5 software (ver3.10).

Images taken by the IVIS spectrum imaging system were collected using Living Image (ver3.2).

Multiplex immunohistochemistry staining images were collected using Vectra (ver3.0.7) and Phenochart Whole Slide Viewer (ver1.0.12).

Electron micrographs of cell structure of YB328 were obtained using scanning electron microscopy (SEM) (S-4500; Hitachi, Tokyo, Japan) and transmission electron microscopy (TEM) (H-7600; Hitachi).

Data analysis

Flow jo (version 10.8.1) was used for all flow cytometry analysis.

Microsoft Office excel 2016, GraphPad Prsim 8, SPSS (ver21.0), and R (ver4.02) were used for statistical analysis and graphs generation.

To identify the composition of the microbiome in 16S rRNA gene sequencing data, raw sequences were demultiplexed and quality-trimmed using a FASTX-Toolkit (hannonlab.cshl.edu/fastx_toolkit/index.html, version 0.0.14) and BBtrim (bbmap.sourceforge.net, version 33.21). A total of 20,000 reads per sample were randomly selected using seqtk (version 1.3-r106) for further analyses. The processed sequences were clustered into OTUs defined at a 97% similarity cutoff using UCLUST version 1.2.22q. Representative sequences for each OTU were then classified taxonomically by using RDP Classifier version 2.2 with the Greengenes 13_8 database. The bioinformatics pipeline QIIME (version 1.9.1) was used as the informatics environment for all relevant processing of raw sequencing data and calculation of bacterial relative abundances.

For estimation of YB328 phylotype abundance in faeces from 16S rRNA sequencing, primers in the reads were trimmed using Cutadapt (version 4.2) if applicable, and the analysis was performed using DADA2 (ver 1.26.0).

For whole-genome sequencing of bacteria, HiFi reads (Q20) were generated using SMRT Link ver. 13.0.0.207600 to remove overhang adapter sequences and create consensus sequences based on the resultant subreads. Lima ver. 2.9.0 and pbmarkdup ver 1.0.3 were used for removing ultra-low PCR adapter sequences and PCR duplex reads, respectively. The resulting reads were assembled using Flye ver. 2.9.5

Phylogenetic tree showing the phylogenetic placement of YB328 and related taxa was constructed based on 120 single-copy marker genes using GTDB-Tk v2.4.0 with GTDB release 220 reference data. Aligned protein sequences were then loaded into an ARB (version 7.0) database, representative genomes were selected, and the data were exported with custom masks for uninformative sites. Approximate maximum-likelihood phylogenetic trees were inferred using FastTree v2.1.1053, and the trees were visualised in ARB.

Genome gene identification was performed with Prodigal (version 2.6.3) with the default settings.

Predicted protein sequences were further analysed by matching against the Clusters of Orthologous Groups (COGs) database (release 3.10 in the Conserved Domain Database, https://www.ncbi.nlm.nih.gov/research/cog-project/) using RPS-Blast (BLAST version 2.9.0+; E-value cutoff of 0.01), the Kyoto Encyclopedia of Genes and Genomes (KEGG) database (release 2019-11-18, https://www.kegg.jp/kegg/download/) and the Virulence Factor Database (VFDB; release 2022.04, https://www.mgc.ac.cn/VFs/download.htm) by protein alignment using DIAMOND (version 2.0.13). Coding sequences unique to strain YB328 compared to other strains (see Extended Data Fig. 4a for genome accessions) were identified using CompareM (version 0.1.2; https://github.com/dparks1134/CompareM) with default settings.

Taxonomic profiling using metagenomics sequencing data was performed by read-level taxonomic assignment by Kraken2(v 2.1.3), followed by estimation of relative abundances using Bracken (v2.9). For this purpose, paired-end reads were processed using fastp (v0.23.2 or v0.24.0). Reads were additionally filtered using NCBI's BMTagger (v3.101) to remove reads derived from the human genomic DNA. Furthermore, to reduce the potential of incorrect false-positive assignments, a representative human genome sequence (GRCh38) was also included in the database.

RNA sequencing reads of BMDCs were generated and analyzed by using the Illumina DRAGEN Bio-IT Platform, following the alignment and annotation by UCSC mouse reference genome (GRCm38.p6) from GENECODE.

Raw imaging data were processed and analyzed by ZEN 3.1 software (blue edition), inForm (version 2.5.1), Live image (version 4.7.3), or ImageJ software (Fiji, version 2.0.0).

For manuscripts utilizing custom algorithms or software that are central to the research but not yet described in published literature, software must be made available to editors and reviewers. We strongly encourage code deposition in a community repository (e.g. GitHub). See the Nature Portfolio guidelines for submitting code & software for further information.

Data

Policy information about availability of data

All manuscripts must include a data availability statement. This statement should provide the following information, where applicable:

- Accession codes, unique identifiers, or web links for publicly available datasets
- A description of any restrictions on data availability
- For clinical datasets or third party data, please ensure that the statement adheres to our policy

The whole-genome sequences of YB328 and P. vulgatus AE61 have been deposited in the NCBI BioProject PRJDB17635. The 16S rRNA gene sequences of the bacterial strains isolated in this study have been deposited in DDBJ/EMBL/GenBank under the accession numbers LC719261, LC744884–LC744889, corresponding to strain YB328, Phocaeicola vulgatus strain AE61, Sellimonas intestinalis strain AE3, Clostridium colicanis strain AE66, Eggerthella lenta strain AE7, Ruminococcus torques strain AE30, and Erysipelatoclostridium ramosum strain AM28.

The metagenome and 16S rRNA gene amplicon sequencing data generated in this study are available under BioProject PRJDB17628.

The datasets used in this study, including the HNSCC cohort and the MONSTAR cohort, are not publicly available because of their association with unpublished studies. Access to these datasets is therefore restricted in accordance with institutional policies and data protection requirements. Researchers interested in accessing these data may submit a formal request to the corresponding author, H. N.

The RNA sequences of bacteria-stimulated BMDCs are available from GEO under accession number GSE285376.

The datasets for the Healthy Japanese cohort datasets (accession numbers DRP005906, DRP007219, DRP007221, DRP007218, DRP007222, and DRP007220), the Routy et al. study (BioProject PRJNA928744), and the faecal metagenomics analysis of global abundance of YB328 in healthy donors (BioProjects PRJEB6456, PRJEB21528, PRJNA422434, PRJNA397112, PRJDB4176, PRJNA517801, PRJNA529400, PRJEB27005, PRJNA529124, PRJEB8094, PRJEB17896, PRJNA328899, PRJEB7369, PRJEB6092, PRJNA268964, PRJNA447983, PRJEB1220, PRJEB1690, PRJNA289586, PRJNA421881, PRJEB17784, PRJEB5224, PRJNA504891, PRJEB9576,

PRJEB6070, PRJNA438847, PRJEB27928, PRJEB12357, PRJEB1786) were downloaded through the Sequence Read Archive.

The predicted protein sequences were analysed by matching against the Clusters of Orthologous Groups (COGs) database (release 3.10 in the Conserved Domain Database, https://www.ncbi.nlm.nih.gov/research/cog-project/), the Kyoto Encyclopedia of Genes and Genomes (KEGG) database (release 2019-11-18, https://www.kegg.jp/kegg/download/) and the Virulence Factor Database (VFDB; release 2022.04, https://www.mgc.ac.cn/VFs/download.htm).

Human research participants

Policy information about studies involving human research participants and Sex and Gender in Research.

Reporting on sex and gender	Clinical specimens used in the GC/NSCLC discovery/validation cohort, HNSCC cohort, and MONSTAR cohort were obtained from both male and female patients, and patient gender is indicated in Table 1-5, 8, Supplementary table 11 and Supplementary table 12.
Population characteristics	Patients who were 20 years old or older were enrolled in this study. Patients who had received antibiotics (ATB) or microbiome intervention therapy within 1 month (NSCLC/GC cohort, HNSCC cohort) or 3 months (MONSTAR cohort) before the initiation of treatment were excluded from this study. Japanese patients with advanced NSCLC (n = 22) and GC (n = 49) who received anti-PD-1 mAb monotherapy (nivolumab or pembrolizumab) were enrolled in this study (see Table 1-5). Japanese patients with HNSCC (n=16) who received PD-1 blockade monotherapy (nivolumab or pembrolizumab) were also enrolled (see Supplementary table 11). In the MONSTAR cohort, Japanese patients with MM (n=16), RCC (n=44), GC (n=32) and EC (n=29) who received PD-1 blockade monotherapy (nivolumab or pembrolizumab) were enrolled (see Supplementary table 12).
Recruitment	For the GC/NSCLC cohort, MONSTAR cohort, and HNSCC cohort, patients diagnosed with GC, NSCLC, MM, RCC, EC, or HNSCC at National Cancer Center, Japan, or referred from other hospitals, were recruited. All patients provided written informed consent prior to enrollment. The possibility of researcher selection bias cannot be entirely excluded. However, patient enrollment was conducted prospectively, and all analyzed cases were obtained during real-world clinical practice rather than in clinical trials, which typically impose strict eligibility criteria. In addition, at the National Cancer Center, human biospecimens are biobanked under a broad consent framework, and sample collection was conducted in parallel with routine diagnostic procedures. Therefore, we believe that any potential bias was effectively minimized. Besides, the MONSTAR cohort is a multi-center collaborative study, which reduces the risk of selection bias from any single institution. Each institute enrolled the majority of patients who met the inclusion criteria, thereby minimizing potential selection bias. Patients who received antibiotics (ATB) or microbiome intervention therapy within 1 month (NSCLC/GC cohort, HNSCC cohort) or 3 months (MONSTAR cohort) before the initiation of treatment were excluded from this study due to these therapies significantly affect the baseline microbiome composition.
Ethics oversight	This study was approved by the institutional review boards of the National Cancer Center and conducted in accordance with ethical guidelines, including the Declaration of Helsinki. All cohorts were conducted in a blinded manner and approved by the National Cancer Center Ethics Committee (IRB protocol numbers: GC/NSCLC cohort, 2015-048 and 2017-007; HNSCC cohort: 2022-346; MONSTAR cohort, 2018-367). The GC/NSCLC and MONSTAR cohorts are registered in the UMIN Clinical Trials Registry (https://www.umin.ac.jp/ctr/, IDs: UMIN000019129 and UMIN000036749, respectively). This information is indicated in the Methods section of the manuscript.

Note that full information on the approval of the study protocol must also be provided in the manuscript.

Field-specific reporting

Please select the one below that is the best fit for your research. If you are not sure, read the appropriate sections before making your selection.

☒ Life sciences ☐ Behavioural & social sciences ☐ Ecological, evolutionary & environmental sciences

For a reference copy of the document with all sections, see nature.com/documents/nr-reporting-summary-flat.pdf

Life sciences study design

All studies must disclose on these points even when the disclosure is negative.

Sample size	No statistical methods were used to predetermine sample sizes. Sample sizes for animal experiments were determined based on preliminary pilot studies (Itahashi et al., Sci Immunol., 2022; Kumagai et al., Cancer Cell., 2022; Kumagai et al., Nat Immunol., 2020), and were in line with standards in the field (Tanoue et al., Nature., 2019; Mager et al., Science., 2020; Gopalakrishnan et al., Science., 2018; Routy et al., Science,

2018; Vétizou et al., Science., 2015; Sivan et al., Science, 2015).

Data exclusions	No data exclusions were needed.
Replication	All in vitro and in vivo experiments were conducted at least 2 times with similar results. Regarding reproducibility of the multiplex immunohistochemistry staining data, three independent regions of interest (ROIs; 682 µm x 510 µm) were analyzed per tissue sample.
Randomization	No randomization was performed in human study, because it was an observational study. In animal experiments, tumor-bearing mice were randomly assigned to treatment groups prior to bacterial inoculation and anti-PD-1 mAb administration.
Blinding	No blinded experiments were conducted in human study, because it was an observational study. All other animal studies were not blinded due to requirements for cage labeling and staffing logistics.

Reporting for specific materials, systems and methods

We require information from authors about some types of materials, experimental systems and methods used in many studies. Here, indicate whether each material, system or method listed is relevant to your study. If you are not sure if a list item applies to your research, read the appropriate section before selecting a response.

Materials & experimental systems

n/a	Involved in the study
☐	☒ Antibodies
☐	☒ Eukaryotic cell lines
☒	☐ Palaeontology and archaeology
☐	☒ Animals and other organisms
☐	☒ Clinical data
☒	☐ Dual use research of concern

Methods

n/a	Involved in the study
☒	☐ ChIP-seq
☐	☒ Flow cytometry
☒	☐ MRI-based neuroimaging

Antibodies

Antibodies used

The antibodies are described below and were validated by manufacturer and in previous publications.

Antibodies for flow cytometry in the human study:
(Antibody, clone, company, catalog number, color)
CD3, UCHT1, BD Biosciences, 557943, PerCP/Cy5.5
CD45RA, HI100, Biolegend, 304138, BV711
CD8, RPA-T8, Biolegend, 301046, BV785
FOXP3, 236A/E7, Thermo Fisher Scientific, 12-4777-42, PE
PD-1, MIH4, BD Biosciences, 564323, BV421

Antibodies for flow cytometry in animal experiments:
(Antibody, clone, company, catalog number, color)
B220, RA3-6B2, Biolegend, 103232, Alexa Fluor 700
CCR7, 4B12, Biolegend, 120124, PE/Cy7
CD103, 2E7, Biolegend, 121416, PerCP/Cy5.5
CD103, 2E7, Biolegend, 121426, PE/Cy7
CD115, AFS98, Biolegend, 135515, BV711
CD117, ACK2, Biolegend, 135108, APC
CD11b, M1/70, BD Biosciences, 563553, BUV395
CD11c, HL3, BD Biosciences, 612796, BUV737
CD11c, N418, Biolegend, 117334, BV605
CD11c, N418, Biolegend, 117319, Alexa Fluor 700
CD135, A2F10, Biolegend, 135313, BV421
CD135, A2F10, Biolegend, 135309, APC
CD19, 1D3/CD19, Biolegend, 152414, Alexa Fluor 700
CD3, 17A2, Biolegend, 100216, Alexa Fluor 700
CD3, 17A2, Biolegend, 100241, BV711
CD4, GK1.5, BD Biosciences, 564922, BUV805
CD40, 3/23, Biolegend, 124610, PE
CD44, IM7, BD Biosciences, 740215, BUV395
CD45.2, 104, Biolegend, 109838, BV510
CD45.2, 104, Biolegend, 109839, BV785
CD62L, MEL-14, BD Biosciences, 740660, BV711
CD8, 53-6.7, BD Biosciences, 612898, BUV805
CD8, 53-6.7, Biolegend, 100750, BV785
CD80, 16-10A1, Biolegend, 104726, BV421
CD86, GL-1, Biolegend, 105014, PE/Cy7
Foxp3, MF-14, Biolegend, 126422, Alexa Fluor 700

Foxp3, MF-14, Biolegend, 126404, PE
Granzyme B, GB11, Biolegend, 515403, FITC
H-2Kb, AF6-88.5, BD Biosciences, 742862, BV711
IFN-γ, XMG1.2, BD Biosciences, 554411, FITC
IRF4, IRF4.3E4, Biolegend, 646416, PerCP/Cy5.5
IRF8, V3GYWCH, Thermo Fisher Scientific, 12-9852-82, PE
Ki67, 16A8, Biolegend, 652424, PerCP/Cy5.5
MHCII, M5/114.15.2, Biolegend, 107606, FITC
MHCII, M5/114.15.2, Biolegend, 107614, APC
MHCII, M5/114.15.2, Biolegend, 107621, Alexa Fluor 700
NK1.1, PK136, Biolegend, 108730, Alexa Fluor 700
p-Akt (S473), M89-61, BD Biosciences, 561670, Alexa Fluor 647
PD-1, J43, BD Biosciences, 744549, BUV395
PD-1, RMP1-30, Biolegend, 109121, BV421
Perforin, eBioOMAK-D, Thermo Fisher Scientific, 12-9392-82, PE
p-Erk (Thr202/Tyr204), 6B8B69, Biolegend, 369510, BV421
p-JNK (T183/Y185), N9-66, BD Biosciences, 562480, PE
p-S6K (S235/S236), N7-548, BD Biosciences, 560434, Alexa Fluor 488
p-S6K (S235/S236), cupk43k, Thermo Fisher Scientific, 46-9007-42, PerCP-eFluor710
p-STAT3 (Tyr705), LUVNKLA, Thermo Fisher Scientific, 17-9033-42, APC
p-ZAP70(Y319), 17A/P-ZAP70, BD Biosciences, 561458, PE/Cy7
TCR Vβ 10[b], B21.5, BD Biosciences, 742822, BV650
TCR Vβ 17[a], KJ23, BD Biosciences, 744787, BV421
TCR Vβ 5.1, 5.2, MR9-4, BD Biosciences, 748930, BUV805
TCR Vβ11, RR3-15, BD Biosciences, 743679, BV650
TCR Vβ12, MR11-1, BD Biosciences, 553300, FITC
TCR Vβ13, MR12-3, BD Biosciences, 743990, BV421
TCR Vβ14, 14-2, BD Biosciences, 553258, FITC
TCR Vβ2, B20.6, BD Biosciences, 748770, BUV737
TCR Vβ3, KJ25, BD Biosciences, 751573, BUV615
TCR Vβ4, KT4, BD Biosciences, 745810, BB700
TCR Vβ6, RR4-7, BD Biosciences, 749465, BUV805
TCR Vβ7, TR310, BD Biosciences, 553216, PE
TCR Vβ8, F23.1, BD Biosciences, 751102, BUV615
TCR Vβ9, MR10-2, Biolegend, 139804, PE
TER-119, TER-119, Biolegend, 116220, Alexa Fluor 700
TNFα, MP6-XT22, Biolegend, 506327, BV421
TLR1, TR23, BD Biosciences, 565792, BV421
TLR2, QA16A01, Biolegend, 153011, PE/Cy7
TLR3, 11F8, Biolegend, 141906, APC
TLR4, UT41, Thermo Fisher Scientific, 12-9041-80, PE
TLR5, ACT5, Biolegend, 148108, PE
TLR6, C1N2, BD Biosciences, 566005, BV421
TLR7, 4G6, Novus Biologicals, NBP2-25274F, FITC
TLR8, 44C143, Novus Biologicals, NBP2-24917F, FITC
TLR9, M9.D6, Thermo Fisher Scientific, 17-9093-82, APC

Antibodies for multiplex immunohistochemistry in human study:
(Antibody, clone, company, catalog number)
CD103, EP206, Cell Signaling Technology, 95835S
CD14, SP192, abcam, ab183322
CD206, CL0387, Sigma-Aldrich, AMAb90746
CD8, C8/144B, Dako, M7103
CLEC9A, EPR22324, abcam, ab223188
IRF8, EPR20441, abcam, ab207418
PD-1, EPR4877(2), abcam, ab137132

Antibodies for confocal imaging:
(Antibody, clone, company, catalog number)
NFATc1, 7A6, Thermo Fisher Scientific, MA3-024
Goat anti-Mouse IgG (H+L) Cross-Adsorbed Secondary Antibody DyLight 488, polyclonal, Thermo Fisher Scientific, 35503

Antibodies for PD-L1 and MMR status evaluated by immunohistochemistry:
(Antibody, clone, company)
PD-L1, 22C3, Dako
PD-L1, SP142, Roche
PD-L1, SP263, Roche
MLH1, ES05, Dako
MSH2, FE11, Dako
PMS2, EP51, Dako

In vivo study: Anti-PD-1 mAb (clone: RMP1-14) and control rat IgG mAb (clone: RTK2758) were obtained from Biolegend. Anti-CSF1R mAb (clone: AFS98) was obtained from Bio X Cell.

Validation

All antibodies used in this study are commercially available. Antibodies employed in flow cytometry, multiplex

Validation	immunohistochemistry, confocal imaging, and immunohistochemistry were validated by the respective manufacturers for use in the relevant species and applications, as stated on the manufacturers' websites. Validation details can be found at the following URLs: BioLegend (https://www.biolegend.com/ja-jp/quality/ product-development), BD Biosciences (https://www.bdbiosciences.com/en-us/products/reagents/flow-cytometry-reagents/research-reagents/quality-and-reproducibility), Thermo Fisher (https://www.thermofisher.com/jp/ja/home/life-science/antibodies/invitrogen-antibody-validation.html), Cell Signaling Technology (hhttps://www.cellsignal.jp/about-us/cst-antibody-validation-principles), Sigma (https://www.merckmillipore.com/JP/ja/life-science-research/antibodies-assays/antibodies-overview/Antibody-Development-and-Validation/cFOb.qB.8McAAAFOb64qQvSS,nav?ReferrerURL=https%3A%2F%2Fwww.google.com%2F), abcam (https://www.abcam.co.jp/primary-antibodies/how-we-validate-our-antibodies), Novus Biologicals (https://www.novusbio.com/5-pillars-validation?srsltid=AfmBOoqq8jfPHiU_P3RPaOOUD9drbBkp4EDHDcE3v24vJ9EOyele8GDQ), Dako (https://www.agilent.com/en/product/dako-omnis-solution-for-ihc-ish/primary-antibodies-for-dako-omnis).The information for the other antibodies is shown in the following pages. https://diagnostics.roche.com/global/en/products/lab/pd-l1-sp142-assay-us-export-ventana-rtd001232.html, https://diagnostics.roche.com/jp/ja/products/tests/ventana-pd-l1-_sp263-assay2.html. https://bioxcell.com/educational-articles/quality-control/. All antibodies were used according to the manufacturers' instructions.

Eukaryotic cell lines

Policy information about cell lines and Sex and Gender in Research

Cell line source(s)	The mouse MC38 colon cancer cell line was obtained from Kerafast (Cat#ENH204). TThe EMT6 mammary carcinoma and B16F10 melanoma cell lines were obtained from ATCC (Cat# CRL-2755 and Cat# CRL-6475, respectively). B16F10-OVA cell lines, derived from B16F10, was generated in-house. THP1-Dual™ hTLR7 cells (Cat#thpd-htlr7), THP1-Dual™ hTLR8 cells (Cat#thpd-htlr8), and THP1-Dual™ hTLR9 (Cat#thpd-htlr9) reporter cell lines were obtained from InvivoGen.
Authentication	The MC38, EMT6, and B16F10 cell lines were pre-authenticated by ATCC using short tandem repeat (STR) sequencing and maintained at low passage numbers. OVA expression in B16F10-OVA cells was confirmed by flow cytometry. THP1-Dual™ hTLR7, THP1-Dual™ hTLR8, and THP1-Dual™ hTLR9 cells were not authenticated but were functionally validated for responsiveness to their respective TLR agonists, serving as positive controls. All cell lines were used within 10 passages from the initial banked vials.
Mycoplasma contamination	All cell lines were regulatory tested and negative for mycoplasma contamination.
Commonly misidentified lines (See ICLAC register)	No commonly misidentified cell lines were used in the study.

Animals and other research organisms

Policy information about studies involving animals; ARRIVE guidelines recommended for reporting animal research, and Sex and Gender in Research

Laboratory animals	Six- to 10-week-old GF C57BL/6 mice and BALB/cJ mice were purchased from CLEA Japan (Tokyo, Japan). OT-I TCR transgenic mice (kindly provided by Dr. W.R. Heath, University of Melbourne), MyD88-/- mice, Tlr7-/-, Tlr9-/-, and Tlr7/9-/- mice (Oriental Bio Service, kindly provided by Dr. S. Akira, WPI Immunology Frontier Research Center, Osaka University), Batf3-/- mice (The Jackson Laboratory, kindly provided by Dr. K. Murphy, Washington University School of Medicine) and Kikume Green–Red (KikGR) mice (RIKEN BioResource Research Center, kindly provided by Dr. M. Tomura, Kyoto University Graduate School of Medicine) were used. GF mice were bred and maintained within the gnotobiotic facilities of the Central Institute for Experimental Animals or purchased from CLEA Japan (Tokyo, Japan)/Sankyo Labo (Tokyo, Japan) and maintained within the gnotobiotic facilities of the National Institute of Advanced Industrial Science and Technology. Other mice were housed in cages under SPF conditions, provided with standard food, given free access to hypochlorous weak-acid water, and housed with a 12:12-hour light/dark cycle with lights on at 8:00 am. The temperature was maintained at 22°C (20–26°C), and the humidity was 45% (40–60%).
Wild animals	No wild animals were used in the study.
Reporting on sex	experiments were performed using female and male age- and sex-matched mice.
Field-collected samples	No field-collected samples were used in the study.
Ethics oversight	Animal care and experiments were conducted according to the guidelines of the animal committee of the National Cancer Center/ Institutional Animal Experiment Committee of National Institute of Advanced Industrial Science and Technology after approval by the Ethics Review Committee for Animal Experimentation of the National Cancer Center (protocol numbers: K24-007, K24-010) and the Institutional Animal Experiment Committee of National Institute of Advanced Industrial Science and Technology (protocol number: 2022-0413).

Note that full information on the approval of the study protocol must also be provided in the manuscript.

Clinical data

Policy information about clinical studies

All manuscripts should comply with the ICMJE guidelines for publication of clinical research and a completed CONSORT checklist must be included with all submissions.

Clinical trial registration	This is not a clinical trial, but an observational study.

Study protocol	All cohorts were conducted in a blinded manner and were approved by the National Cancer Center Ethics Committee (IRB protocol numbers: GC/NSCLC cohort, 2015-048 and 2017-007; HNSCC cohort, 2022-346; MONSTAR cohort, 2018-367). The GC/NSCLC and MONSTAR cohorts are registered in the UMIN Clinical Trials Registry (https://www.umin.ac.jp/ctr/) under the identifiers UMIN000019129 and UMIN000036749, respectively.
Data collection	Clinical data were collected from medical records.
Outcomes	Since this was an observational study, no predefined outcomes were established.

Flow Cytometry

Plots

Confirm that:

☒ The axis labels state the marker and fluorochrome used (e.g. CD4-FITC).

☒ The axis scales are clearly visible. Include numbers along axes only for bottom left plot of group (a 'group' is an analysis of identical markers).

☒ All plots are contour plots with outliers or pseudocolor plots.

☒ A numerical value for number of cells or percentage (with statistics) is provided.

Methodology

Sample preparation	For human specimens: To collect tumor-infiltrating lymphocytes (TILs), tumor tissues were minced and treated within 72 hours after surgery with a TIL preparation protocol using an optimized tissue preservation reagent (Tumor & Tissue Preservation Reagent: TTPR) and TIL isolation reagent (Tumor & Tissue Dissociation Reagent: TTDR), which were codeveloped with BD Biosciences, or were treated immediately using the gentleMACS™ Dissociator. For mouse specimens: To isolate TILs and lymphocytes in lymph nodes, tissues were harvested and minced into small pieces, followed by digestion with BD Horizon™ Dri TTDR reagent at room temperature for 20 minutes. After dissociation, the cell suspension was filtered using a 70-µm strainer and washed with PBS supplemented with 1% BSA. For intestinal tissues, small intestines (duodenum, jejunum, and ileum) were excised. The intestinal contents were removed by washing with HBSS. Fat tissue was also removed. Peyer's patches and mesenteric tissues were cut carefully and digested in BD Horizon™ Dri TTDR reagent according to the manufacturer's instructions. Intestines were further opened longitudinally and cut into 5-mm lengths. Tissues were digested by a Lamina Propria Dissociation Kit (Miltenyi Biotec) according to the manufacturer's instructions.
Instrument	FACSAria Fusion (for sorting), LSR Fortessa, or FACSymphony (for analyzing) from BD Biosciences were used for data collection.
Software	BDFACS Diva software (ver8.0.3) was used for data collection, and Flow jo (ver10.8.1) was used for analysis.
Cell population abundance	The cell populations were sufficient for downstream analysis. For cell sorting, cell purity confirmed by FACS was >95% after sorting.
Gating strategy	First we gated based on physical parameters (FSC-A vs SSC-A), then excluded doublets (FSC-H vs FSC-A and SSC-H vs SSC-A). On the singlets, we selected for live cells using Fixable Viability Dye eFluor 780 (Thermo Fisher Scientific).CD8+ T cells as CD45+CD3+CD8+, CD4+ T cells as CD45+CD3+CD4+, effector Treg cells as CD45+CD45RA-FoxP3highCD4+CD3+ (for human samples) or CD45+Foxp3+CD4+CD3+ (for murine samples). Dendritic cells as CD45+CD11c+MHCII+. CD103+CD11b- conventional dendritic cells as CD45+CD11c+MHCII+CD103+CD11b- (in vivo) or CD45+CD11c+MHCII+CD135+CD103+CD11b- (in vitro). CD11b+ cells as CD45+CD11b+. CDPs were identified as Lin−CD117intCD135+CD115+CD11c−MHCII− BM cells. All gating strategies are provided in the figures, extended data figures, and supplementary information.

☒ Tick this box to confirm that a figure exemplifying the gating strategy is provided in the Supplementary Information.